SLAC-220
UC-34d
(E)

D MESON PRODUCTION IN e^+e^- ANNIHILATION*

Petros-Afentoulis Rapidis

Stanford Linear Accelerator Center
Stanford University
Stanford, California 94305

June 1979

Prepared for the Department of Energy
under contract number DE-AC03-76SF00515

Printed in the United States of America. Available from National Technical Information Service, U.S. Department of Commerce, 5285 Port Royal Road, Springfield, VA 22161. Price: Printed Copy $6.50; Microfiche $3.00.

* Ph.D. dissertation.

ABSTRACT

The production of D mesons in e^+e^- annihilation for the center-of-mass energy range 3.7 to 7.0 GeV has been studied with the MARK I magnetic detector at the Stanford Positron Electron Accelerating Rings facility. We observed a resonance in the total cross-section for hadron production in e^+e^- annihilation at an energy just above the threshold for charm production. This resonance, which we name ψ'', has a mass of 3772 ± 6 MeV/c^2, a total width of 28 ± 5 MeV/c^2, a partial width to electron pairs of 345 ± 85 eV/c^2, and decays almost exclusively into $D\bar{D}$ pairs. The ψ'' provides a rich source of background-free and kinematically well defined D mesons for study. From the study of D mesons produced in the decay of the ψ'' we have determined the masses of the D^o and D^+ mesons to be 1863.3 ± 0.9 MeV/c^2 and 1868.3 ± 0.9 MeV/c^2 respectively. We also determined the branching fractions for D^o decay to $K^-\pi^+$, $\bar{K}^o\pi^+\pi^-$ and $K^-\pi^+\pi^-\pi^+$ to be $(2.2 \pm 0.6)\%$, $(4.0 \pm 1.3)\%$, and $(3.2 \pm 1.1)\%$ and the branching fractions for D^+ decay to $\bar{K}^o\pi^+$ and $K^-\pi^+\pi^+$ to be $(1.5 \pm 0.6)\%$ and $(3.9 \pm 1.0)\%$. The average number of kaons per D decay was found to be 0.52 ± 0.14 K^o's and 0.42 ± 0.12 K^+'s.

The rate for inclusive production of D mesons at center-of-mass energies above the ψ'' has been measured; we find that it can account for most, if not all, of the observed increase in the total hadronic cross-section for center-of-mass energies above 4 GeV. The inclusive momentum and energy spectra for D's have been measured at the highest available center-of-mass energy (7 GeV). The energy spectra are rapidly decreasing functions of energy with a slope similar to the slope of the charged pion spectrum at the same center-of-mass energy. This behaviour suggests that the fragmentation function of the charmed quark into charmed mesons is a decreasing function of the scaling variable $z = 2E_D/E_{CM}$.

ACKNOWLEDGMENTS

Current research in high-energy physics is dominated by large collaborations of tens of physicists working in unison, trying to unravel the mysteries of nature. This work, therefore, owes its existence, to a great extent, to the diligent efforts of the members of the collaborations for experiments SP-17 and SP-26 at SPEAR. The members of these collaborations were: Gerry Abrams, Saj Alam, Adam Boyarski, Marty Breidenbach, Don Briggs, Fatin Bulos, Willie Chinowsky, Susan Cooper, Jim Dakin, Jonathan Dorfan, Bob Ely, Joe Feller, Gary Feldman, Gerry Fischer, Abe Fong, Carl Friedberg, David Fryberger, Lina Glatieri, Bruno Gobbi, Gerson Goldhaber, Gail Hanson, Frank Heile, Bob Hollebeek, John Jaros, Bernard Jean-Marie, John Kadyk, Betty Kwan, Rudy Larsen, Pierre LeComte, Alan Litke, Dieter Lüke, Bruce Lulu, Vera Lüth, Harvey Lynch, Don Lyon, Ron Madaras, Jim Martin, Terry Mast, Don Miller, Chuck Morehouse, H.K. Nguyen, Sherwood Parker, Ewan Paterson, Martin Perl, Ida Peruzzi, Marcello Piccolo, Francois Pierre, Ting Pun, myself, Burt Richter, Mike Ronan, Ron Ross, Bernard Sadoulet, Dan Scharre, Rafe Schindler, Roy Schwitters, Jim Siegrist, Bill Tanenbaum, George Trilling, Tom Trippe, Francois Vannucci, Vincent Vuillemin, Scott Whitaker, Jim Wiss, Dave Yount and John Zipse.

Special thanks should go to my advisor, Martin Perl, for his continuous assistance and support; to Gary Feldman, who in many ways proved to be my real advisor and mentor, and from whom I learned how to be a physicist; to Ida Peruzzi and Marcello Piccolo, to whom the results of chapters 3 and 4 owe a great deal and whose friendship I cherish; to John Jaros for very helpful criticism and advice on the analysis of the results of the last chapter; to Bruno Gobbi and Lina Galtieri for their overall assistance and hospitality.

I also wish to thank Alan Litke, Stanley Wojcicki, and Fred Gilman, who as members of my thesis committee had to suffer the punishment of reading an early version of this work, and for their useful comments.

My comrades-at-arms, fellow graduate students, Joe Feller, Frank Heile, Ken Hayes, and Jim Wiss, deserve special mention, because not only did they serve as sources of inspiration but also because I

shared with them the fears and pains of a graduate student's life.

The SPEAR operations staff (Tom Taylor, Ken Underwood, Bill Graham, Vergne Brown, Larry Feathers, Ed Guerra, Bob Stege, and Bruce Walker), deserve special mention for making the machine perform as a reliable and powerful tool for physics research. Ken Witthaus, Ron Baggs, Ron Stickley, Acie Newton and Bob Leonard, (all members of Group E's staff), who helped in many ways in making this experiment a success should also be mentioned.

I want to thank Leo Resvanis for his friendship, advice, and help in surviving in SPEAR's fiery environment; Marlene Durand and Roger Freedman for their support. I also want to acknowledge my parents' and my family's support throughout my long tenure as a graduate student at Stanford.

The polished appearance of this thesis owes a great deal to the efforts of SLAC's technical illustrations department and to the expert typing of Mrs. Irmgild Schack and Miss Karen Goldsmith.

Finally, this work owes an implicit debt to Burt Richter, who did more than anybody else in raising e^+e^- physics to the prominent position it currently occupies.

TABLE OF CONTENTS

CHAPTER I

INTRODUCTION

In this work we will examine the general features of the inclusive production of D mesons in e^+e^- annihilation for center of mass energies of 3.6 to 7.8 GeV. We will first discuss the discovery of the $\psi''(3772)$, a resonance just above the threshold for $D\bar{D}$ production that decays predominantly into $D\bar{D}$ pairs, and we will study the D mesons produced in its decay. We will then turn to the study of the inclusive production of D mesons at higher energies. Finally, we will examine the characteristics of D meson production at the highest available energies in our apparatus (7 GeV) with the aim of obtaining some information on the fragmentation function of the charmed quark.

Before embarking on this long task we will review the overall picture of hadron production in e^+e^- annihilation within the context of the quark-parton model. We will also give a short account of the theoretical expectations for charmed particle production in e^+e^- reactions, within the framework of the charmonium model, as well as a review of the current theoretical prejudices on the form of the fragmentation function of heavy quarks.

Rather than devoting a disproportionate fraction of this introduction to a description of the quark-parton model and of charm phenomenology, we will assume that the reader is familiar with these topics. We will expand only on the particular areas of direct relevance to our work. This significant drawback of this work is mitigated by the existence of a large number of excellent reviews in the recent literature.[1-8] As a poor substitute, Table I summarizes the properties of the SU(4) quarks, and of the predicted and established charmed meson states.

TABLE I

a. SU(4) quarks

Name	u	d	s	c
I	1/2	1/2	0	0
I_z	+1/2	+1/2	0	0
Q	+2/3	-1/3	-1/3	+2/3
B	1/3	1/3	1/3	1/3
Y	1/3	1/3	-2/3	0
S	0	0	-1	0
C	0	0	0	1

b. Charmed Mesons

Name	Mass (GeV/c^2)	Spin	Isospin I_z	Favoured decays
D^o	1.8633	0	-1/2	$K^-\pi^+$, $\bar{K}^o\pi^o$, $K^-\pi^+\pi^+\pi^-$, $\bar{K}^o\pi^+\pi^-$, $K^-\pi^+\pi^o$, $K^-\pi^+\pi^o$, $K^-e^+\nu$,...
D^+	1.8683	0	+1/2	$\bar{K}^o\pi^+$, $K^-\pi^+\pi^+$, $\bar{K}^o\pi^+\pi^-\pi^+$, $\bar{K}^o e^+\nu$, ...
F^+	2.03 (?)	0	0	$\eta\pi^+$, $\phi\pi^+$, $K^+K^-\pi^+$, $\bar{K}^oK^+$,...
D^{o*}	2.0060	1	-1/2	γD^o, $\pi^o D^o$
D^{+*}	2.0086	1	+1/2	γD^+, $\pi^o D^+$, $\pi^+ D^o$
F^{+*}	2.14 (?)	1	0	γF^+

A. HADRONIC PRODUCTION IN e^+e^- ANNIHILATION

Figure 1 shows schematic diagrams for the major processes occuring in e^+e^- annihilation for relatively low center of mass energies ($E_{c.m.}$ less than 10 GeV). Diagrams (a) and (b) illustrate the major quantum electrodynamical (QED) processes: Bhabha scattering (e^+e^- elastic scattering, a combination of graphs (a) and (b)) and lepton pair production (b). These processes proceed through a single virtual photon and can be easily calculated in QED. Diagram (c) shows the annihilation of a positron and an electron into two photons, another copious QED process. Diagram (d) illustrates the "two-photon" production mechanism that contributes to the total hadronic cross section. The contribution from such processes at our energies turns out to be almost negligible. This contribution is expected to increase like $(\ln s)^2$ and should become significant at higher energies.[9]

Finally, diagrams (e) and (f) are the diagrams for hadron production which is the subject of our study. Here we have assumed that the only significant contribution to hadron production comes from the formation of a single intermediate virtual photon which, in turn, couples to a quark-antiquark ($q\bar{q}$) pair. The $q\bar{q}$ pair then decays, through an as yet not understood mechanism, into a final hadronic state with the quantum numbers of the photon, i.e. a $J^{PC} = 1^{--}$ neutral, non-strange, non-charmed state. The possibility of the virtual photon coupling to a vector resonance (which may be a bound state of a $q\bar{q}$ pair) is shown explicitly in (f).

The naive picture of hadron production, as the manifestation of the production of more elementary point-like fermions, the quarks, allows us to relate the total hadronic cross section to the cross section for the production of a pair of charged leptons, e.g. $\mu^+\mu^-$ production. From QED we have that

$$\sigma_{\mu\mu} = \sigma(e^+e^- \to \mu^+\mu^-) = \frac{4\alpha^2}{3s} = \frac{86.86 \text{ nb}}{s(\text{GeV}^2)} = \frac{21.72 \text{ nb}}{E^2_{\text{beam}}\ (\text{GeV})} \ .$$

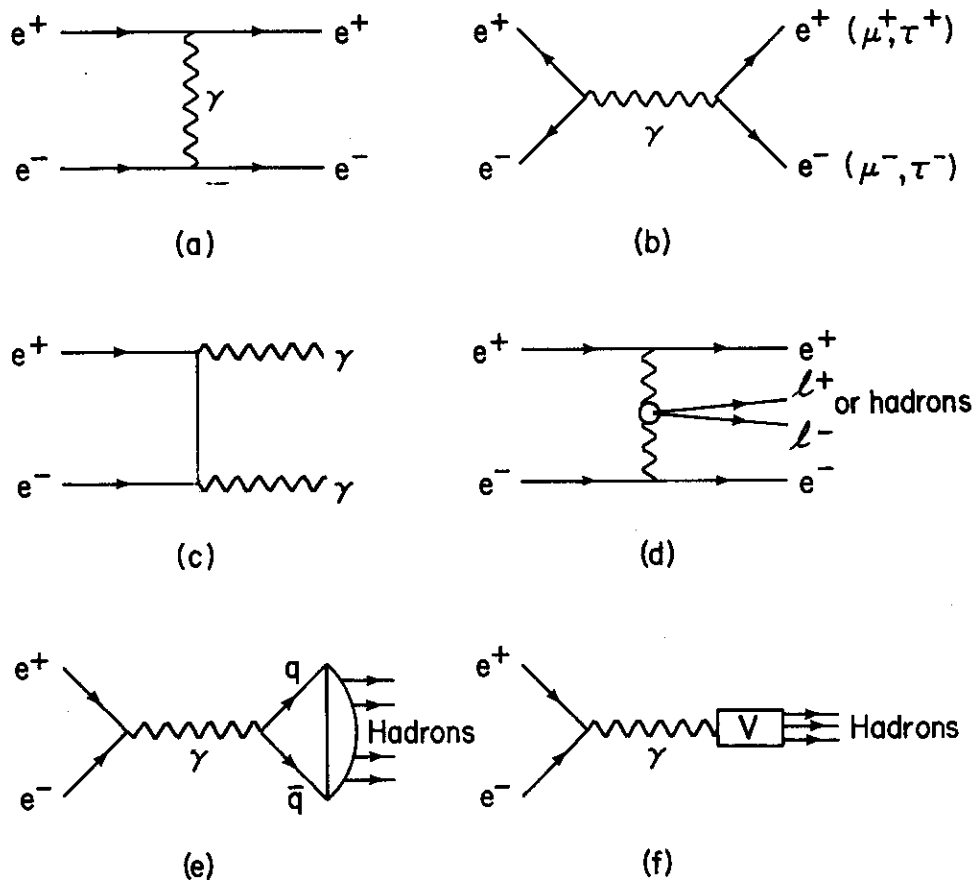

Figure 1 . Some schematic diagrams of processes taking place in e^+e^- collisions. The wavy lines represent photons, the straight lines are leptons and hadrons.

For the total hadronic cross section we have, in a similar manner,

$$\sigma_h = \sigma(e^+e^- \rightarrow \text{hadrons}) = \sigma_{\mu\mu} \times 3 \sum_i Q_i^2$$

where Q_i is the square of the charge of the i'th quark flavour in units of the electron charge, the sum runs over all the quark flavours which can be produced in pairs at a particular center of mass energy, and the overall factor of 3 accounts for the three quark colours of quantum chromodynamics (QCD).

It is by now customary to display results in terms of R, the ratio

$$R = \frac{\sigma_h}{\sigma_{\mu\mu}} = 3 \sum_i Q_i^2 \quad .$$

R in the quark parton picture of SU(4) (see Table I) should be constant and have the value

$$R_a = 3(\frac{1}{9} + \frac{1}{9} + \frac{4}{9}) = 2$$

for energies below the charm threshold (3.7 GeV) where only the "conventional" u, d, and s quarks contribute. At higher energies, where the c quark contribution has to be included, R should be

$$R_b = 3 \times (\frac{1}{9} + \frac{1}{9} + \frac{4}{9} + \frac{4}{9}) = \frac{10}{3} = 3.33 \quad .$$

Figure 2 shows the value of R as a function of energy as measured in our experiment. We find that $R_a = 2.5$ approximately for $E_{c.m.} = 3$ GeV and that R = 5.2-1 = 4.2 at 6 to 7 GeV. In the last value a unit of R, due to the pair production of the heavy lepton τ which is included in the data of Fig. 2, has been subtracted.

The general features of R validate the predictions of the naive quark model. We indeed observe a step in R of approximately the expected magnitude at $E_{c.m.} = 4$ GeV. As we shall show in Chapter 4, all of the observed increase and structure in R can be accounted for by the production of charmed mesons. The deviation of the asymptotic value of R from the naive model's predictions can be explained as a correction arising from QCD quark-gluon interactions. Far from

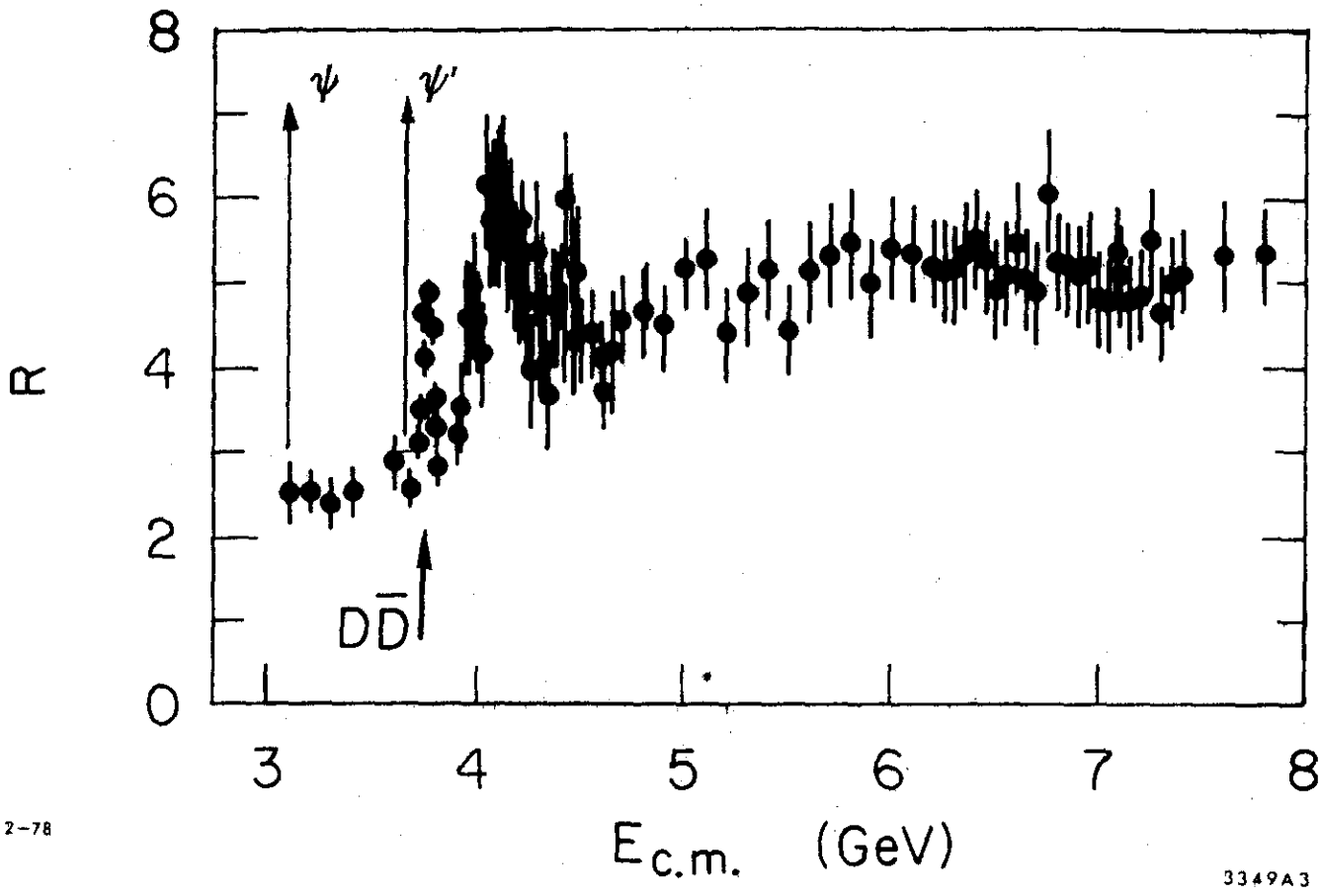

Figure 2. The ratio of the total hadronic cross section to the μ pair production cross section, $R = \frac{\sigma_h}{\sigma_{\mu\mu}}$, as a function of the center of mass energy. The bulk of the data are from Ref. 51, the data at the $\psi''(3772)$ have been added to them. The contribution to R due to pair production of the heavy lepton τ has not been subtracted. Radiative corrections have been applied and the radiative tails of the ψ and ψ' have been subtracted.

thresholds and resonances QCD predicts[10] that

$$R_{QCD} = 3 \sum_{i=1} Q_i^2 \left(1 + \frac{\alpha_s(E)}{\pi} + k\left[\frac{\alpha_s(E)}{\pi}\right]^2 \right)$$

where $\alpha_s(E)$ is the running coupling constant of QCD analogous to the QED α, and k is a numerical constant with a value close[11] to 1. In the standard (SU(4) × SU(3)) model of quarks the coupling constant has the value

$$\alpha_s(E) = \frac{\alpha_s(E_o)}{1 + \frac{25}{12\pi}\alpha_s(E_o)\ln(E^2/E_o^2)} \quad ,$$

with $\alpha_s(E_o)$ determined from experimental data. Our values of R in the 3 to 4.5 GeV region imply a value of $\alpha_s(6\ \text{GeV}) \simeq 0.6$.

The onset of the step in R is accompanied by significant structure in the 3 to 4.5 GeV region. As seen in Fig. 2 and Fig. 3 at least five distinct resonances are observed in this region: the $\psi(3095)$, the $\psi'(3684)$, the $\psi''(3772)$, the $\psi(4.03)$, and the $\psi(4.41)$. The parameters of these resonances can be found in Table III of Chapter 3. It should be noted that at experiments at the DESY colliding beams facility another resonance at 4.16 GeV has been observed. Figure 3 is a compilation of all the published measurements of R.

The most striking feature of the data are the extremely narrow widths of the first two resonances, the $\psi(3095)$ and the $\psi'(3684)$, both of which lie below the threshold for charmed particle production. The reason for this extraordinary occurrence can be found in the Okubo-Zweig-Iizuka (OZI) mechanism.[12] This poorly understood semi-empirical selection rule states that transitions in which the initial quarks annihilate each other and do not survive to the final state should be suppressed. This rule, originally proposed to explain the enhanced branching ratio of the decay $\phi \to K\bar{K}$ relatively to decays with no strange mesons in the final state (e.g. $\pi^+\pi^-\pi^o$), is evidently at work here. The $\psi''(3772)$, which lies above the $D\bar{D}$ threshold, has a width two orders of magnitude greater than the width of the $\psi'(3684)$ and decays, as we shall show in Chapter 3, almost exclusively into $D\bar{D}$. Figure 4 is a schematic illustration of this rule.

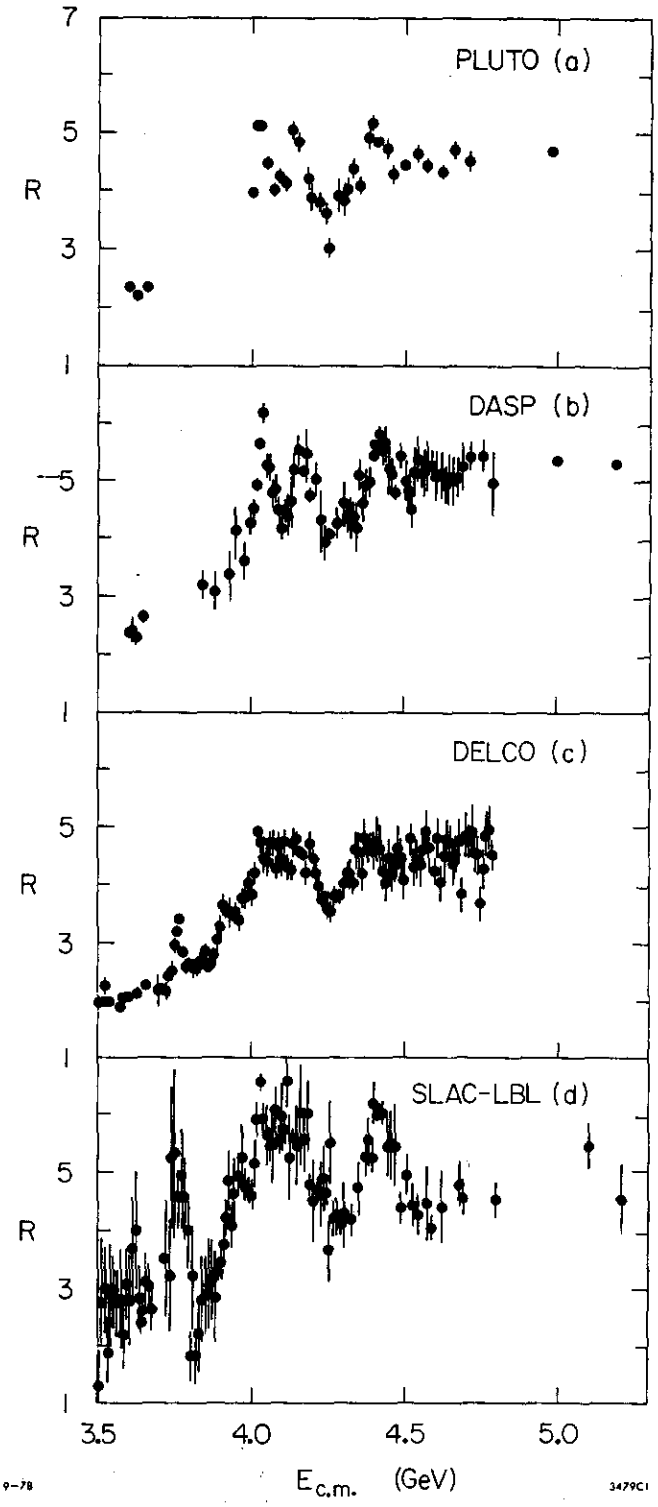

Figure 3. R versus energy from various experiments (taken from Ref. 1). The R values in (a),(b), and (d) have been radiatively corrected. τ pair production is included in R. The data in (d) at the $\psi''(3772)$ are older data collected during the first half of our experiment and do not include the data presented in chapters 3 and 4.

The observation of the narrow resonances, together with the observation of intermediate χ states in the electromagnetic cascades[13,41]

$$\psi' \to \gamma\chi \to \gamma\psi \quad \text{and} \quad \psi' \to \gamma\chi \to \text{hadrons}$$

provided the impetus for the development of the charmonium model.[7,14,15] In this model the ψ's are viewed as bound states of a non-relativistic $c\bar{c}$ system with a binding potential of the form*

$$V(r) = -\frac{\alpha_s}{r} + \frac{r}{a^2} \quad .$$

This form, dictated by the asymptotic freedom features of QCD, is Coulomb-like at short distances and allows for a treatment of the $c\bar{c}$ system along the lines of the treatment of positronium (bound system of e^+e^-) in QED. For energies below the charm threshold, this model, if one includes non-relativistic spin-dependent forces, predicts a spectrum of hydrogen-like excited states which decay electromagnetically to the ground state. In this model, the $\psi'(3684)$ is a radially excited state with the same quantum numbers as the $\psi(3095)$. The rich spectrum predicted[7] has been observed in our experiment[13,41] and is a major success of the charmonium theory. The spectrum is shown in the form of a Grotrian diagram in Figure 5.

The extension of this model to energies above 3.7 GeV, using the parameters of the ψ and the ψ' as input to adjust the variables of the model, leads to definite predictions for the cross section for inclusive production of D mesons in e^+e^- annihilation. The predictions[15] are shown in terms of ΔR, the expected increase in R due to D production, in Figure 6. The existence of an isolated $^3D_1$ resonance at 3750, which decays into $D\bar{D}$, and the subsequent discovery of the $\psi''(3772)$ form the most spectacular success of the model. At higher energies, charmonium gives a qualitatively correct respresentation of the data.

---

*It should be noted that α_s in this formula, as determined[7] from $\psi(3095)$ decays through an intermediate three gluon state, is approximately 0.2 This value is in strong disagreement with the value of 0.6 obtained from the R values. This is one of the major outstanding problems in the charmonium model.

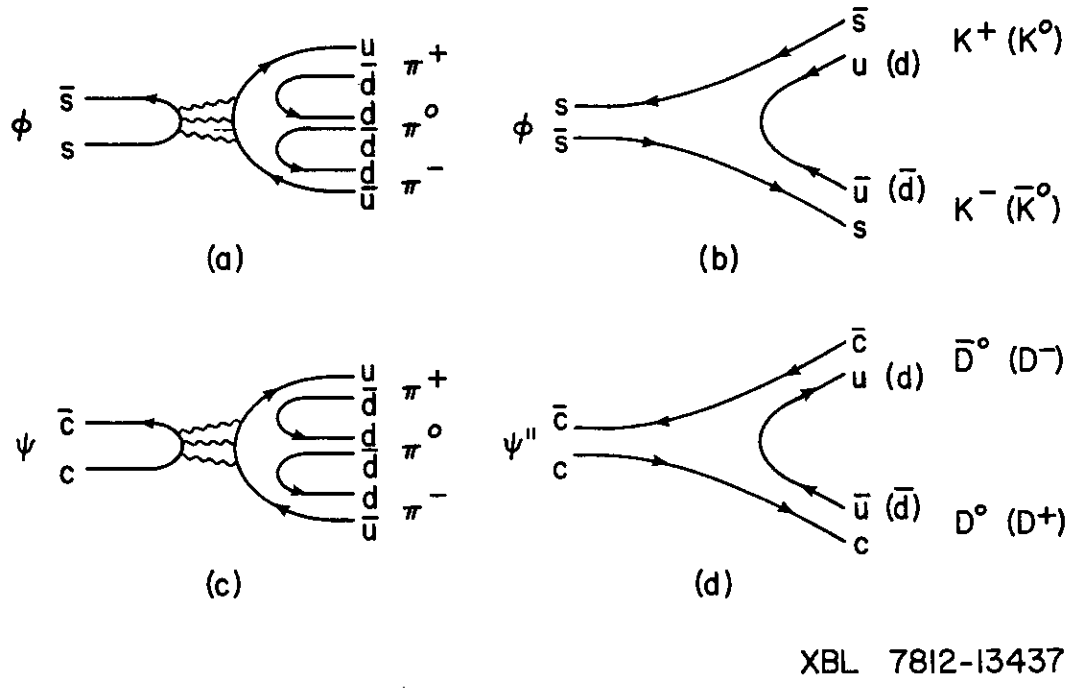

Figure 4. Illustration of the OZI rule. Diagrams (a) and (c) are forbidden, (b) and (d) are allowed. The decay rates for the four diagrams are Γ_a= 0.6 MeV , Γ_b= 3.4 MeV , Γ_c= 0.7 keV , and Γ_d= 28 MeV . The wavy lines represent gluons.

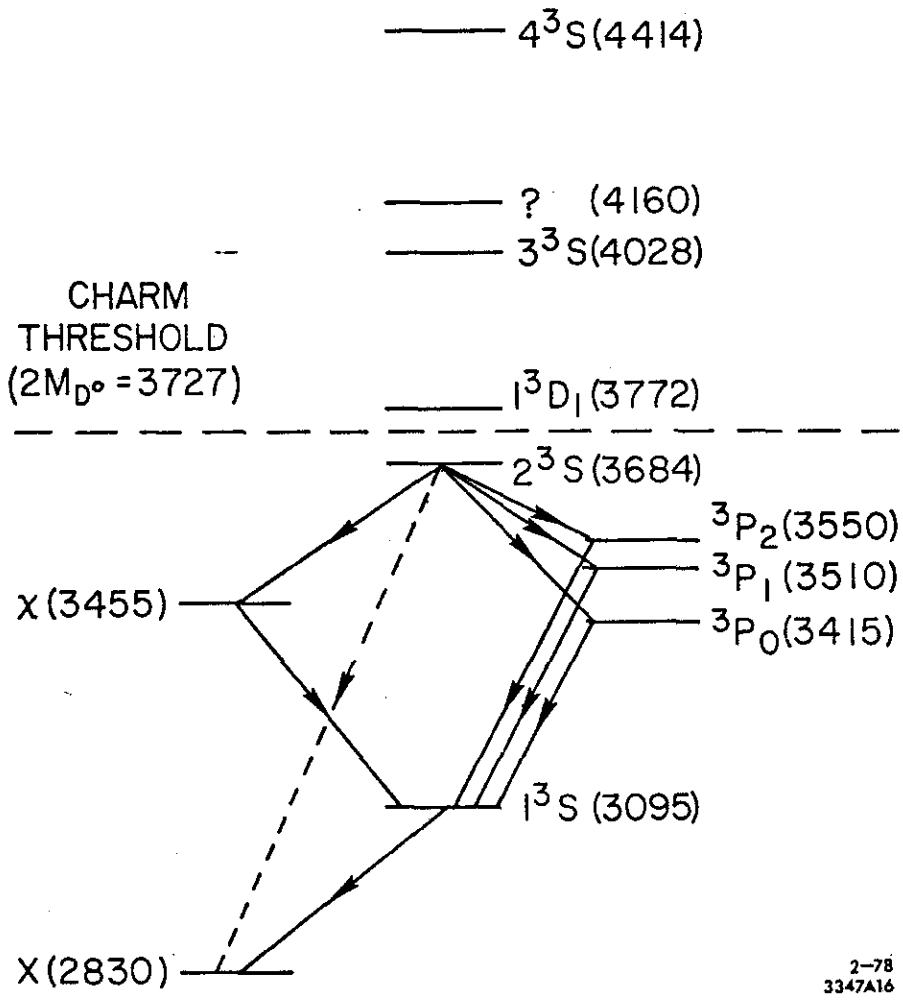

Figure 5 . The observed charmonium levels with the notation $n^{2S+1}L_J$ and masses in MeV/c^2. The correct identification for X(2830) and χ(3455) is not known and even their existence is in doubt[79]. Observed radiative transitions are shown in solid directed lines. The dotted line represents an M1 transition which has not yet been observed. Splittings are approximately to scale.

The opening of the $D\bar{D}^*$ and $D^*\bar{D}^*$ channels at 4.03 GeV and the dominance of $D^*\bar{D}^*$ over the other modes are features of the measured D meson production.

Even though the validity of the model at energies above 4.2 GeV, where there is enough energy to produce higher mass charmed mesons (e.g. $\bar{F}F$), becomes suspect, the predictions of Fig. 6 serve to illustrate the expected behavior of D production. Since D mesons are the lowest lying charmed mesons, their production, either directly or as the result of the decay of heavier charmed particles, should be a major fraction of the $1\frac{1}{3}$ units of R due to charm.

In addition to D mesons, F mesons and charmed baryons are also expected to be produced in e^+e^- annihilation and contribute to R. Possible indications for the F and F^* mesons have been observed in the process

$$e^+e^- \to F^+ \; F^{*-} \;\; \hookrightarrow \gamma F^- \;\; \hookrightarrow \eta\pi^+$$

by the DASP experiment,[3,16] and as a small enhancement in the invariant mass distribution of $KK\pi$ in our experiment.[†17,18] There has been no measurement of the inclusive production of F mesons in e^+e^- annihilation. The results of Chapter 4 allow for at most ½ unit of R to be due to F pair production.

Charmed baryon production should manifest itself as an increase in the rate of inclusive production of protons and Λ's, provided that the c.m. energy is above the threshold for their production. Measurements* of $R_{p+\bar{p}}$ and of $R_{\Lambda+\bar{\Lambda}}$, the contributions to R due to proton and Λ production, from our experiment[19] are shown in Figure 7. We observe an increase in $R_{p+\bar{p}}$ of approximately 0.3 units at $E_{c.m.} = 4.5$ GeV which can be attributed to charmed baryon production.

---

*Whenever we use the symbols $R_{a+\bar{a}}$ or $\sigma_{a+\bar{a}}$ they always refer to the sum of the inclusive processes $e^+e^- \to a$ + anything and $e^+e^- \to \bar{a}$ + anything, unless otherwise noted.

†A recent unpublished analysis of the results from the MARK II collaboration at SPEAR, of comparable statistics, indicates that the $KK\pi$ enhancement we observed is probably a statistical fluctuation.[80]

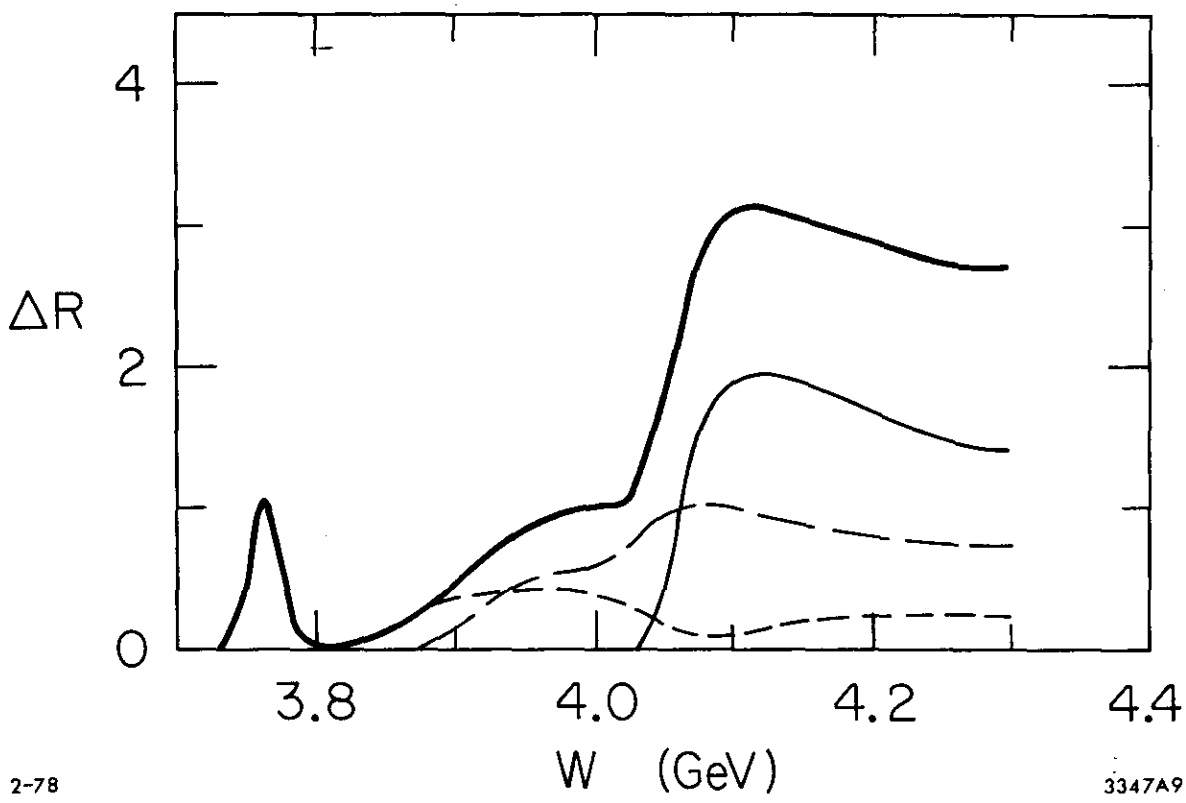

Figure 6 . The charm contribution to R as computed in the coupled-channel charmonium model of Ref. 15 . The heavy solid curve is the sum of the contributions from $D\bar{D}$ (short-dashed curve), $D\bar{D}^*$ + $D^*\bar{D}$ (long-dashed), and $D^*\bar{D}^*$ (light solid); F meson production makes a negligible contribution.

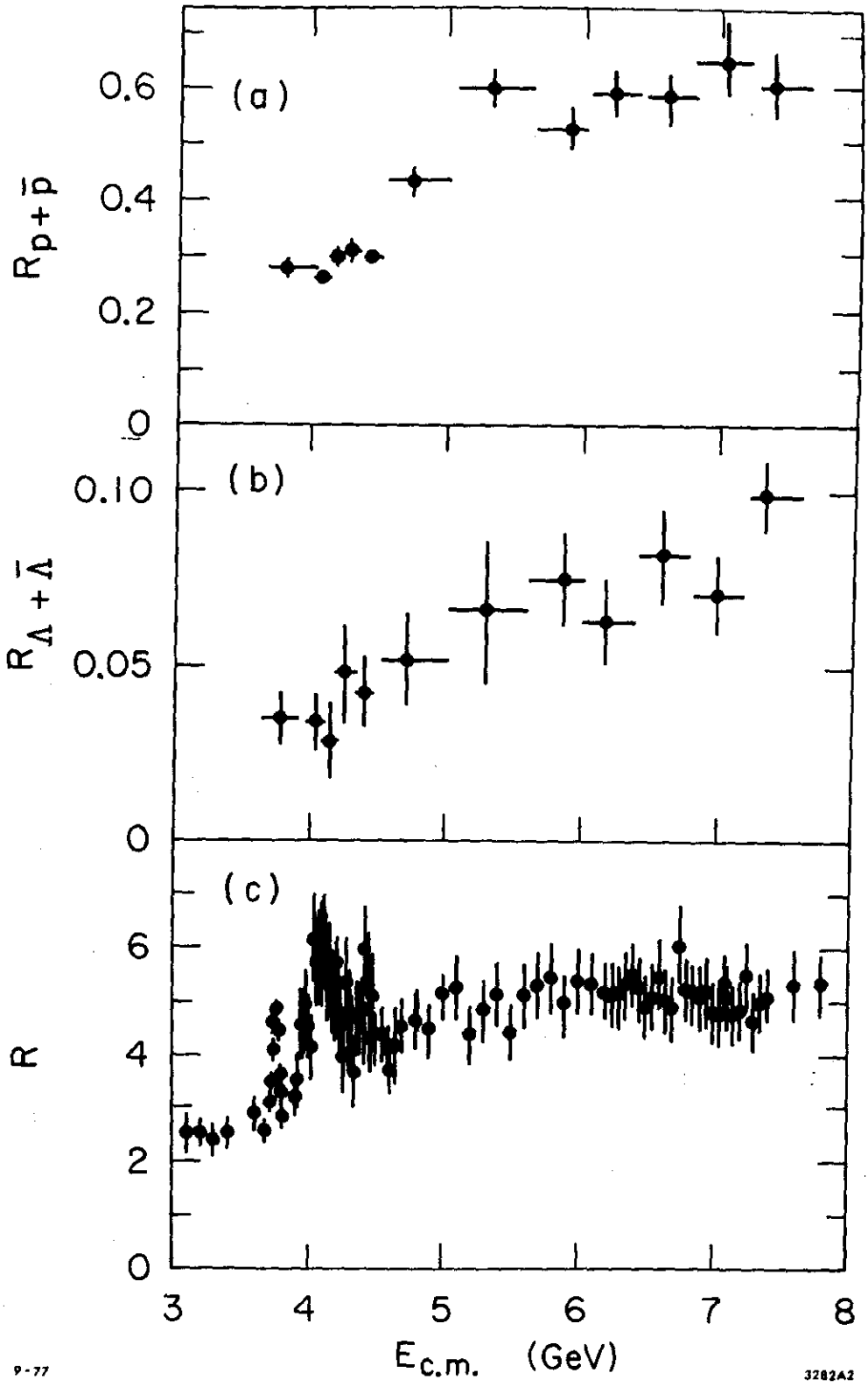

Figure 7 . (a) $R(p + \bar{p}) = 2\,\sigma(\bar{p}) / \sigma_{\mu\mu}$ vs c.m. energy,
(b) $R(\Lambda + \bar{\Lambda}) = (\sigma(\Lambda) + \sigma(\bar{\Lambda})) / \sigma_{\mu\mu}$ vs c.m. energy,
(c) $R = \sigma_h / \sigma_{\mu\mu}$ vs c.m. energy (see Fig. 2).

B. INCLUSIVE PRODUCTION OF HADRONS IN e^+e^- ANNIHILATION AND THE QUARK FRAGMENTATION FUNCTION

The quark-parton model[2,20] offers a simple and understandable framework in which one can analyze the inclusive production of hadrons in any scattering process. The basic assumption of this approach, pioneered by Feynman, is that the underlying mechanisms in any process involve quarks, i.e. point-like charged fermions. The quarks can scatter in two-body collisions, can be generated in quark-antiquark pairs by the strong (colour) field and the electromagnetic field, and can be probed by weak and electromagnetic forces (e.g. in lepton-hadron scattering). The result of this approach is that any particle interaction can be factorized into distinct stages, each stage being described by a set of universal functions that characterize the quark content of hadrons, the quark-quark scattering cross section, and the quark 'decay' properties.

For example, in the case of hadroproduction of a hadron h, shown diagrammatically in Figure 8a, the differential cross section is given by:[21,22]

$$\frac{E d\sigma}{d^3 p_h}(s,\ t,\ u;\ AB \to hX) =$$

$$\sum_{a,b,c} \int_{x_{a,\min}}^{1} \int_{x_{b,\min}}^{1} G_{A\to a}(x_a) G_{B\to b}(x_b) D_c^h(z_c) \cdot \frac{1}{z_c} \cdot \frac{1}{\pi} \cdot \frac{d\hat{\sigma}}{d\hat{t}}(\hat{s},\hat{t};q_a q_b \to q_c q_d)$$

where $G_{A\to a}(x_a)$ describes the probability of finding a quark of flavour a in the hadron A with a fraction x_a of the hadron's momentum, $\frac{d\hat{\sigma}}{d\hat{t}}$ is the differential cross section for quark-quark scattering expressed in terms of the $\hat{s}$, $\hat{t}$ invariants of the quark system $q_a + q_b$, and $D_c^h(z_c)$, the quark fragmentation function, is the probability of a quark of flavour c to fragment into a hadron h carrying a fraction z_c of the

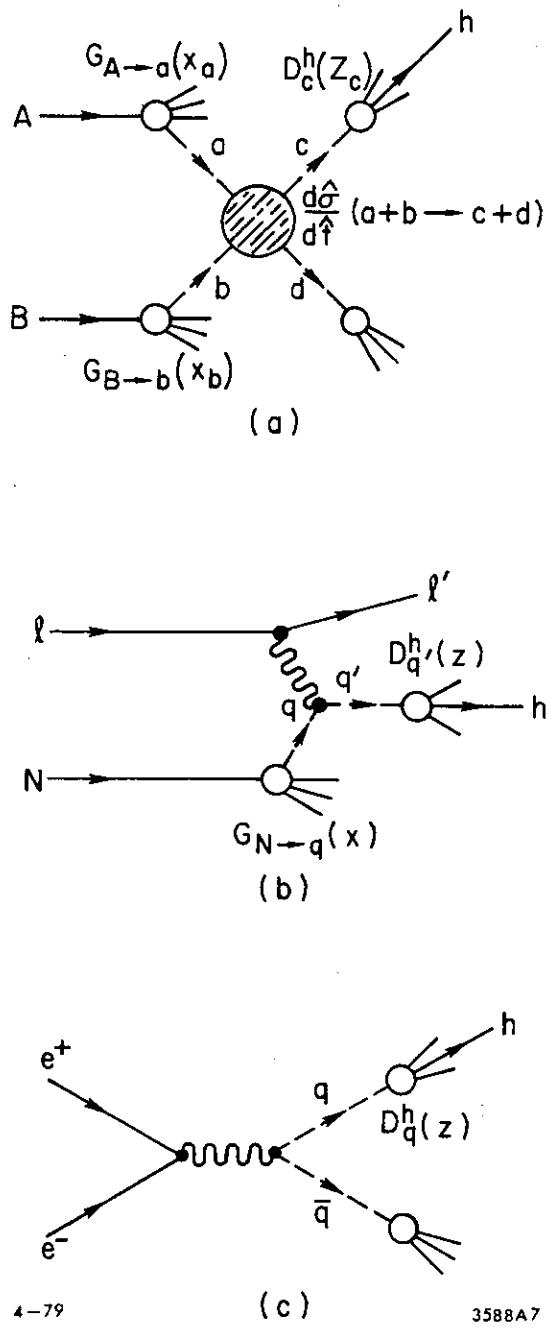

Figure 8 . Quark-parton-model mechanisms for :

(a) hadron-hadron collisions,

(b) hadron production in lepton-hadron collisions,

(c) hadron production in e^+e^- annihilation.

We have emphasized the assumed underlying constituent interactions.

quark's energy.*

In a similar way, the cross section for the leptoproduction of hadrons (Fig. 8b) can be written as

$$\frac{d\sigma}{dxdz}\ (\ell N \to \ell' hX) \propto \sum_n G_{N\to n}(x) D_n^h(z) \quad ,$$

from which we observe that the G functions are directly related to the nucleon structure functions determined from deep inelastic eN and νN scattering.

Finally, for the inclusive production of hadrons in e^+e^- annihilation (Fig. 8c) we have:

$$\frac{d\sigma}{dz}\ (e^+e^- \to hX) = \frac{4\pi\alpha^2}{3s} \sum_i Q_i^2\ D_i^h(z) \quad ,$$

i.e. the cross section of producing a hadron h having a fraction z of the beam energy is directly related to the fragmentation functions and the charges of the produced quarks. We see that e^+e^- annihilation provides a very clean mechanism for studying the fragmentation function. Information from such a study together with the nucleon structure functions obtained from leptoproduction experiments can then be used to analyze the results of hadroproduction, in particular high p_T phenomena, and obtain information on the underlying quark scattering cross section.

It must be emphasized that the above picture is extremely naive and wrong. Effects such as the contribution[33] of QCD gluons have not

---

*There is no accepted meaning of z. Some authors define z as the fraction of the quark's energy carried by the hadron, while others use $z = p/E_q$, the ratio of the hadron's momentum to the quark's energy. This is a significant distinction when the quark energy is not much larger than its mass. To avoid this problem Field and Feynman[22] suggest the use of a rapidity-like variable $y = \frac{E + p_{||}}{E_q + P_q}$, where E and $p_{||}$ are the energy of the hadron and the component of the hadron's momentum along the original quark direction, and E_q and P_q are the energy and momentum of the quark.

been included and they could alter our view significantly. Furthermore, we once again assumed that the one-photon exchange mechanism dominates quark pair and hadronic production in e^+e^- annihilation. Lacking any better description we will adhere to this simplistic view.

In the case of charmed meson production the situation is even simpler:

$$\frac{d\sigma}{dz}(e^+ + e^- \to D + X) = \frac{4\pi\alpha^2}{s}\left(\frac{4}{9} D_c^D(z)\right) \quad ,$$

that is, the sum of the previous equation over all allowed quark flavours simplifies to a single term. Here we have used the assumption that the only quark fragmenting to charmed particles is the charmed one. This assumption is justified on the basis of the relatively high mass of the charmed quark ($m_c \simeq 1.5$ GeV/c) which suppresses the production of $c\bar{c}$ pairs from the vacuum. The measurement of $\frac{d\sigma}{dz}(e^+ + e^- \to D + X)$ is, under these assumptions, a direct measurement of the charmed quark fragmentation function.

The relatively high mass of the charmed quark has led a number of theorists to propose a variety of forms for its fragmentation function, some of them different from the generally accepted form for the fragmentation function of conventional quarks. Suggested forms for conventional quarks (e.g. $D_u^{\pi^+}(z)$) are:

Form:	Author:
$\frac{1}{z}(1-z)$	Sehgal and Zerwas[24]
$\frac{1}{z}$	Seiden[25]
$(n+1)\ (1-z)^n$ with n=1 or 2	Gronau et al.[26]
$A'\left[1-a+3a(1-z)^2\right]+B\left[\frac{3}{3-2a}\frac{1}{z}+\frac{3a}{2a-1}z+\frac{2a(2a^2-3a-2)}{(3-2a)(2a-1)}z^{2-2a}\right]$ with $a \simeq .8$	Field and Feynman[22]
$\frac{(1-z)^n}{z}+\delta(z-a)$	Ellis, Jacob, and Landshoff[27]

These forms, derived mostly from dimensional counting,[28] are likely to be asymptotic expressions appropriate when the quark and hadron masses are negligible compared to the energy of the fragmenting quark.

Forms suggested for heavy and/or charmed quarks are:

(a) $$D(z) \sim \delta(z - \frac{m_D}{m_c + Q}) = \delta(z - .84) \quad ,$$

with $m_D = 1.87$ GeV/c^2, $m_c = 1.5$ GeV/c^2 and Q a flavour independent parameter of the order of 1.0 GeV/c^2. This has been suggested by Suzuki[29] on the basis of a thermodynamic fireball model in which the energy is distributed to the fragmentation hadrons according to a Boltzman distribution.

(b) $D(z) \propto z^3(1-z)$, a model of Kartvelishvili et al.,[30] based on the reciprocity relation at $z \lesssim 1$, which requires that

$$D_q^h(z) \sim G_{H \to q}(z) \text{ for } z \to 1 \quad ,$$

i.e. that the probability that the quark q decays to a high momentum hadron h is the same as the probability of finding a quark q with a high momentum inside a hadron h.

(c) e^{-bz}, a phenomenological parametrization of Barger, Gottschalk, and Phillips,[31] used in their analysis of the lepton energy spectrum in opposite sign di-lepton events observed in neutrino interactions.[32] This spectrum, due to electrons produced in the semileptonic decays of charmed particles, can provide information on the D function's shape. Their analysis of the Fermilab data[33] gives $b \lesssim -3$.

An analysis of CDHS data, along the same lines, by Odorico[34] gives b = 0 or b = +3 as better values. This author remarks that the data demand that "D(z) must be non-small near z=1".

(d) $D(z) = A\, e^{-B\left[(z - \langle z \rangle)/\Delta\right]^2}$ with $\langle z \rangle \lesssim .7$, $\Delta \lesssim .1$, another shape favouring the high z end of the D function proposed by Dias De Deus.[35]

(e) Bjorken suggested,[36] without proposing a specific form, that D(z) should be peaked at high z values. The argument behind this suggestion is that the c quark is very massive, carried most of the momentum and is not perturbed much by the simultaneously generated light quarks.

In summary, there is a large amount of controversy on the shape of the fragmentation function of the charmed quark. Many authors suggest

that it should be drastically different from the D functions of the conventional quarks, being either a constant independent of z or concentrated at high z values. These considerations provided the motivation for our study of the inclusive production of D mesons at high c.m. energies.

Before ending this discussion we should emphasize two points: First, the energies available to us are rather small ($E_{beam} \lesssim 3$ GeV) and comparable to the charmed quark mass ($m_c \lesssim 1.5$ GeV/c^2). Modifications to the fragmentation function due to threshold effects and the limited available energy may be very large, making both the application of asymptotic formulae in this energy regime and the extraction of conclusions that may be applicable to higher energies questionable.

Second, in all of the preceding discussion we have assumed scaling, a natural property of any parton model. In our case scaling is equivalent to the statement that the fragmentation function depends only on z and does <u>not</u> depend on E_q, the quark's energy. QCD implies[23] a breakdown of scaling. $D(z, E_q)$ is then an increasing function of E_q for $z \sim 0$ and a decreasing function of E_q for $z \sim 1$. We should expect the fragmentation function to become more concentrated at $z = 0$ as the energy of the primary quark increases.

CHAPTER 2

APPARATUS AND DATA ANALYSIS

Both the Stanford Positron Electron Accelerating Rings (SPEAR)[37] at SLAC and the SLAC-LBL Magnetic Detector MARK I on which the data for this experiment were collected are by now justly famous and have been extensively described elsewhere.[38-44] The discussion that follows is limited in scope, its aim being only to provide a framework such that the results of Chapters 3, 4, and 5 will be intelligible.

A. SPEAR

The SPEAR Colliding Beam Facility[37] is shown in outline in Fig. 9. It consists of a roughly circular ring of 32 m radius around which a single bunch of electrons and a single bunch of positrons injected from SLAC's LINAC circulate on a coincident orbit in a common vacuum chamber and magnetic guide field in opposite directions. Energy to the circulating particles, to compensate for synchrotron radiation losses, is supplied through the R.F. system which operates at a frequency of 356 MHz. The energy of the beams, E_b, is controlled by the intensity of the magnetic guide field and can cover the range $1 \lesssim E_b \lesssim 4$ GeV. The error in the calibration of the energy of the ring, which is the same as the error of $\oint Bdl$ on the beam orbit, is $\pm .1\%$ and the error in setting the energy is $\pm .1$ MeV.

The bunches collide with zero crossing angle at each of the two interaction regions, the east and west experimental pits, with a frequency of 1.28 MHz. Each of the bunches occupies an ellipsoidal volume of $\sigma_z = 6$ cm, $\sigma_x \simeq \sigma_y \simeq .02$ cm with the long axis along the direction of motion. The luminous volume at the interaction area has the dimensions $\sigma_z = 4$ cm, $\sigma_x \simeq \sigma_y \simeq .015$ cm .

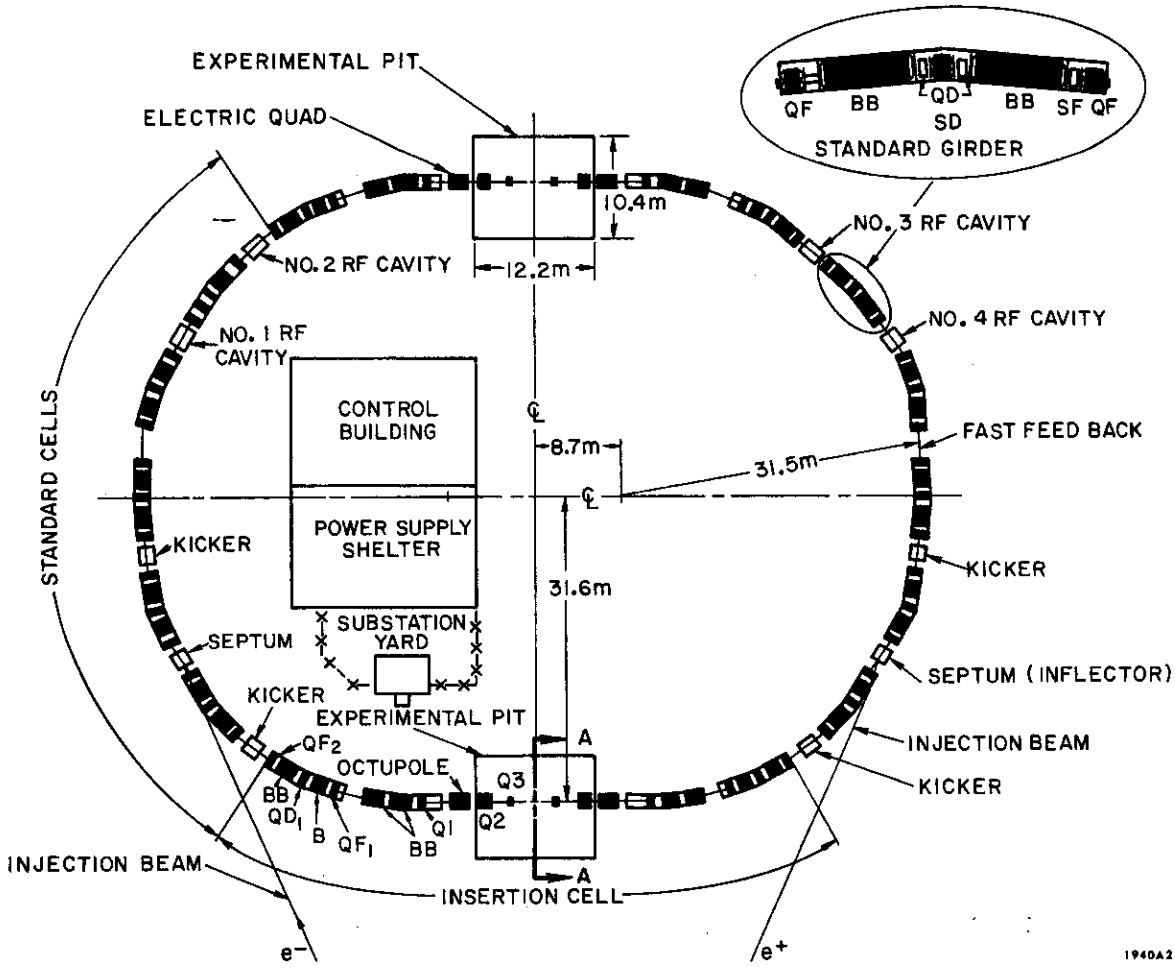

Figure 9 . Layout of the SPEAR e^+e^- colliding beams facility. This experiment was carried out in the experimental pit at the bottom of the figure - the west pit.

The instantaneous luminosity at SPEAR at the beginning of a fill is approximately $(E_b/1.8)^4 \times 10^{30}$ cm^{-2} sec^{-1} for $E_b \lesssim 3$ GeV and 10^{31} cm^{-2} sec^{-1} for $E_b > 3$ GeV. The beam currents and luminosity decay exponentially in time. When the luminosity has dropped below optimum, the beams are dumped and the ring is refilled.

This experiment was carried out in the west pit interaction area of SPEAR using the SLAC-LBL Magnetic Detector.[38-44] For the first part of the experiment the original detector without any modifications was used, while for the second half the detector was modified with the addition of the Lead Glass Wall system.

B. THE SLAC-LBL MAGNETIC DETECTOR

The SLAC-LBL Magnetic Detector (Figs. 10 and 11) is a cylindrical array of counters and chambers used to track and identify particles. Starting from the interaction region and moving outward, the various components of the magnetic detector are:

1) The beam pipe -- it has a mean radius of 8 cm and is made of 0.15 mm thick corrugated stainless steel. The average effective thickness, due to the corrugation, is 0.20 mm.
2) The pipe counters -- there are four semi-cylindrical plastic scintillation counters forming two concentric cylinders at radii of 11 and 13 cm. Each cylinder is 7 mm thick and 36 cm long. They are part of the trigger and serve primarily to reduce triggers from cosmic rays. The efficiency of each counter for detecting minimum-ionizing particles is greater than 95%, as measured with cosmic rays.
3) The proportional chambers -- there are two cylindrical proportional chambers at radii of 17 and 22 cm with active regions in polar angle of 34° - 146° and 29° - 151°. Each of them consists of 512 sense wires parallel to the beam axis. The wire spacing in the inner chamber is 2 mm and the wire spacing in the outer chamber is 3 mm. The efficiency of each chamber for detecting prongs in multi-prong hadronic events is greater than 90%.

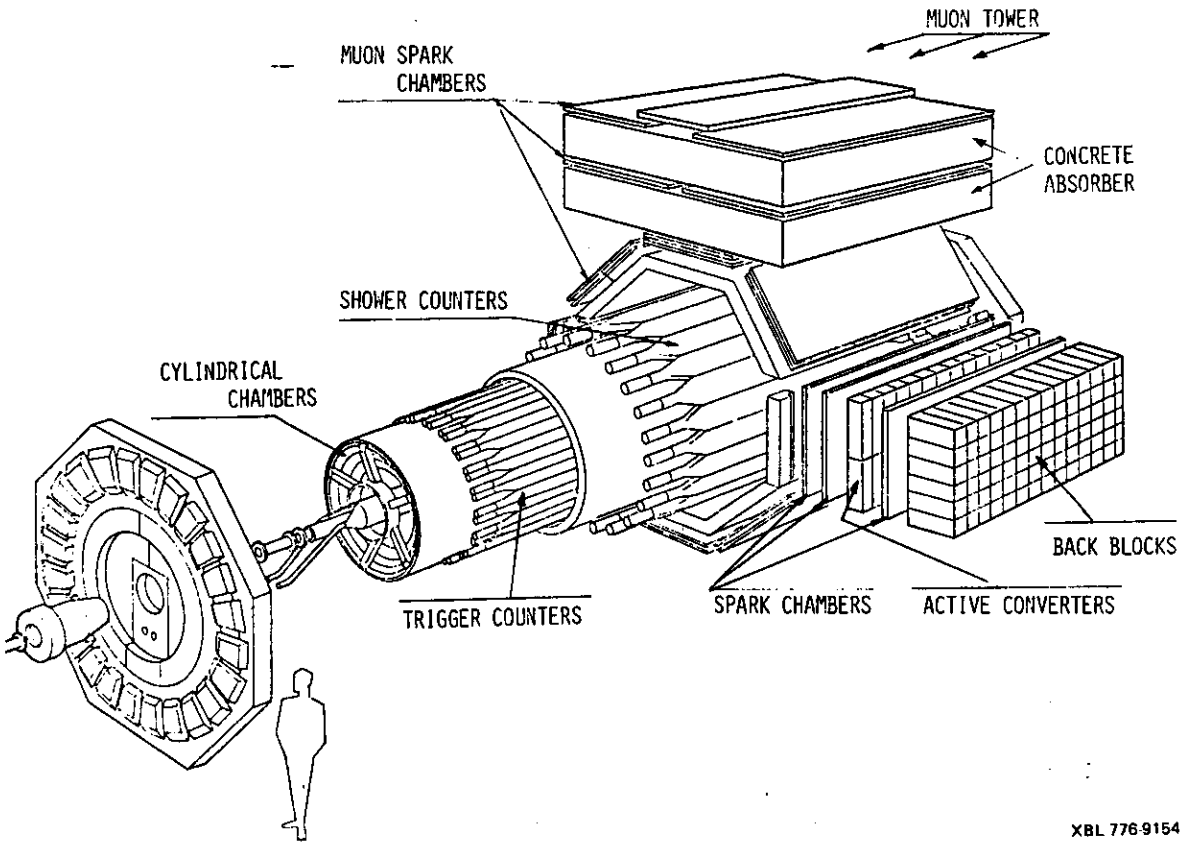

Figure 10. Exploded view of the SLAC-LBL MARK I magnetic detector. The Lead-Glass Wall system is on the right. The center of SPEAR is to the left.

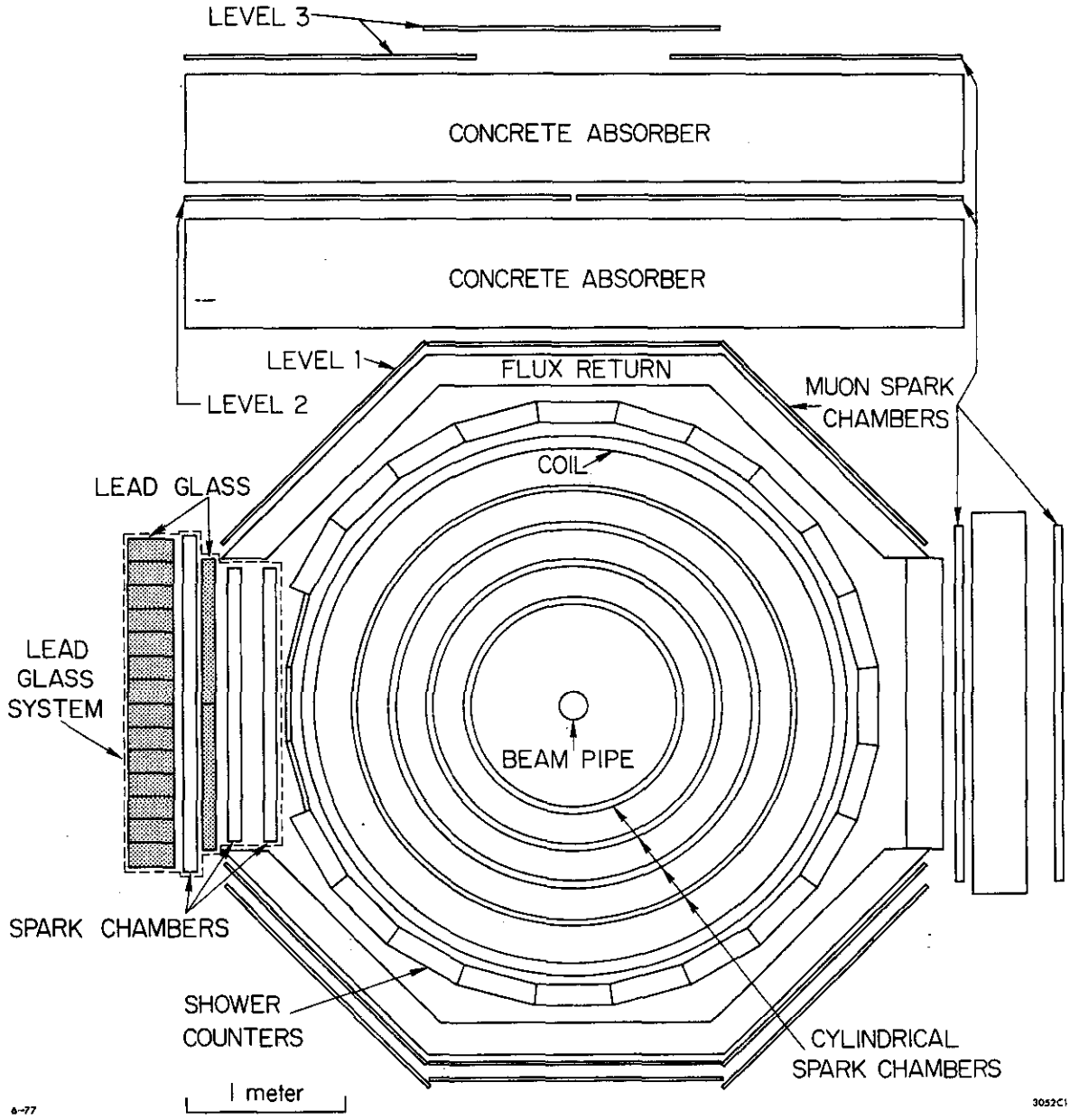

Figure 11. The MARK I magnetic detector as seen looking along the beam line. The proportional chambers around the beam pipe and the trigger counters are not shown. The Lead-Glass Wall is shown on the left side of the figure. The center of the ring is to the right.

4) The cylindrical spark chambers -- there are four modules of concentric cylindrical magnetostrictive spark chambers at radii of 66, 91, 112, and 135 cm with active regions in polar angles of 31° - 149°, 40° - 140°, 43° - 137°, and 45° - 135°. Each module consists of two gaps and four "planes" with the wires at $\pm 2^{\circ}$ and $\pm 4^{\circ}$ with respect to the beam axis. The wire spacing in each "plane" is 1.1 mm. Since the analysis requires sparks in three out of the four modules and two out of the four wires in each module, the efficiency for reconstructing tracks is generally greater than 95%. The angular acceptance of the cylindrical spark chambers is approximately $0.70 \times 4\pi$ sr. The rms momentum resolution for a 1 GeV/c track is about 15 MeV/c. The structural support for the chambers consists of six, 6 mm wall, 5 cm diameter, aluminum posts at a radius of 79 cm, and a 1.3 cm thick aluminum cylinder at a radius of 1.49 m. These posts subtend about 6% of the solid angle. Since they can be major sources of multiple scattering, charged particles whose trajectories pass through one of them must be discarded, thereby reducing the effective angular acceptance of the detector.

5) The trigger counters -- there are forty-eight plastic scintillation counters immediately outside the aluminum cylinder supporting the spark chambers. Each counter made of Pilot-Y scintillator is 2.5 cm thick, 23 cm wide, and 260 cm long. They are viewed from each end by a 5 cm diameter Amperex 56-DVP photomultiplier tube. These counters are part of the trigger. They also provide time-of-flight (TOF) information with a rms resolution (σ_{TOF}) of 0.35 - 0.45 ns. This time-of-flight information allows a one-standard-deviation separation between π and K at 1.2 GeV/c momentum and a one-standard-deviation separation between K and p at 1.8 GeV/c momentum for $\sigma_{TOF} = .35$ ns. The solid angle subtended by these counters if $0.65 \times 4\pi$ sr.

6) The solenoid -- an aluminum solenoidal coil 3.6 m long, 9 cm thick and 3.3 m in diameter provides an axial magnetic field of approximately 4 kG which is uniform to 5% in the active region of the tracking chambers.

7) The shower counters -- there are twenty-four shower counters outside the solenoid. A counter consists of five 0.64 cm thick lead sheets each followed by a 0.64 cm sheet of Pilot-F scintillator. The counters are 48 cm wide and have an active length of 3.1 m. They are viewed from each end by a 13 cm diameter RCA 4522 photomultiplier tube. These counters are part of the trigger. However, their primary function is to discriminate between electrons and hadrons. They also have been used to a limited extent to detect photons. The plastic scintillators in the shower counters were inadvertently scratched during assembly of the counters. As a result, the attenuation length was reduced from 145 cm to typically 75 cm.

For the second half of the experiment three shower counters in one octant of the Magnetic Detector were removed and replaced by six scintillation counters. This was done to accommodate the Lead Glass Wall system and still preserve the original two-charged particle trigger of the Magnetic Detector. These scintillation counters are arranged in such a way that every two of them replace one of the shower counters. These scintillation counters are 1.3 or 1.9 cm thick, 46 cm wide and 152 cm long. They use exactly the same photomultiplier tubes, electronics and software as the three shower counters they replaced.

This alteration of the experiment does not change perceptibly the response of our detector to events with a hadronic multi-particle final state, which are the only class of events used in this work.

8) The iron flux return -- the detector is surrounded by iron which acts both as a flux return and hadron filter. The iron is 20 cm thick around the circumference of the detector and 8 to 12 cm thick on the ends. One octant of the iron flux return has been removed and replaced by the Lead-Glass Wall system.

9) The muon spark chambers -- there are one or two large planar magnetostrictive wire spark chambers outside the return iron in each octant to detect muons. The inner detector and the return iron are 1.7 interaction lengths thick, absorbing muons with

momenta less than 500 MeV/c. For better hadron rejection, five spark chambers and two 1.7 interaction length thick concrete absorbers are placed on top of the detector. The minimum average momentum required for a muon to pass through the first concrete absorber is 910 MeV/c. A spark chamber and a 1.7 interaction length thick iron absorber are placed behind the return iron in the octant opposite to the Lead-Glass Wall system.

10) The luminosity monitors -- there are four counter telescopes, two at each end of the detector at ± 20 milliradians from the beam line in the vertical plane, each one consisting of a defining scintillator followed by a lead-scintillator shower counter, monitoring the luminosity of the storage ring by observing small angle e^+e^- elastic scattering events. Large angle e^+e^- elastic scattering events in the main detector are also used to determine the luminosity.

11) The Lead-Glass Wall system, which replaced for the second half of the experiment one octant of the shower counters, consists of 318 lead-glass Cherenkov shower counters and three wire spark chambers. The arrangement of the system into two horizontal rows of 26 active converters (.10 m × .90 m × .11 m) each and 14 horizontal rows of 19 back blocks (.32 m × .15 m × .15 m) interleaved with spark chambers is seen in Fig. 10.

This system allowed for very good electron and photon identification over the limited solid angle it covered (6% of 4π). Since the following analysis did not use any of the information of the Lead-Glass system we refer to Refs. 43 and 44 for more information on this system.

C. TRIGGER

The data presented here were collected with the "two-charged particle" trigger which was the standard trigger for the Magnetic Detector before the addition of the Lead-Glass Wall system. The trigger rate of the Magnetic Detector is limited to a few triggers per second by the time required to recharge the spark chamber pulsing system. The rate of coincidences of two-or-more trigger counters

with the solenoid on and 25 mA of stored current is approximately 3 KHz. Therefore, two-or-more shower counter latches are required in the trigger to suppress the low-energy machine background and a coincidence between the inner and the outer pipe counters on the same side is required to suppress the cosmic ray background.

A pickup electrode upstream from the detector along one or the other beam detects the passage of the particle bunch and generates a master strobe. This master strobe is split and delayed to generate gates for the various counter latches. A coincidence between:

1) The beam pickup strobe;
2) A coincidence of the inner and outer pipe counters on the same side;
3) Two trigger counters firing in coicidence with the radially outward shower counter or the next closest shower counter ("2-TASH" requirement);[41]
4) Two shower counters firing in coincidence with one of the two trigger counters directly inward or one of the closest two trigger counters ("2-SHAT" requirement);[41] defined the two-charged particle trigger.

The requirement of shower counter firings in the trigger, necessitated by the ferocious background, introduces a momentum bias since low momentum particles may interact in the preceding coil and never reach them. This bias, together with the bias intrinsic in a two particle trigger, can only be corrected with the help of a Monte Carlo simulation of the detector's response and is the cause of the largest part of the systematic uncertainty in measuring the total cross section for e^+e^- annihilation into a hadronic final state.

For the second half of the experiment two additional triggers, the "one particle and neutral energy" trigger and the "total neutral energy" trigger, which incorporated information of the total energy detected by the Lead-Glass system were added. The events collected with these triggers were not included in our analysis presented here and we will not discuss them any further.

D. DATA ANALYSIS

The digitized information for every event, consisting of latches of counters that fired, pulse heights for all the trigger and shower counters, TDC readouts for the trigger counters and magnetostrictive wand readouts were processed off-line on SLAC's IBM-370 computer system.

The off-line analysis program performed the following functions:

1) Rejected events that did not contain sufficient information to warrant further analysis or events for which the TOF readouts indicated that they were due to cosmic rays.
2) By an exhaustive search procedure[39] of combining the reconstructed spark chamber points into groups, found the tracks in an event and determined the momentum of each track by fitting a circular helix to these points (CIRCLE fit). At this level the momentum resolution was

$$\frac{\sigma_p}{p} \simeq .15\ p(\text{GeV}) \quad .$$

3) Using the previously determined tracks, a rough vertex position was determined from which all, or most, of the tracks originated.
4) More accurate vertex and momenta were determined through the CIRCE fitting routines,[45] that incorporated a very accurate representation[39] of the detector's solenoidal field. This part of the analysis consisted of three steps:

   i) Vertex CIRCE

   The constraint that all of the tracks originated from a common vertex, the location of the vertex being a free parameter, was imposed. This fit gave a momentum resolution $\frac{\sigma_p}{p} \simeq .05\ p(\text{GeV})$ and the most accurate estimate of the vertex location.[42]

   ii) One-track CIRCE

   The momentum for each track was determined without any constraint as to a common vertex for all tracks. The momentum resolution obtained was again $\frac{\sigma_p}{p} \simeq .05\ p(\text{GeV})$. These momenta overwrote the ones determined by the vertex CIRCE and proved very valuable in the search of secondary vertices from particles like K^o_s or Λ's that decayed a short distance from the interaction region.

iii) Beam Constrained CIRCE

Identical to the vertex CIRCE in (i) except that the vertex location was constrained to lie within the ellipsoid of the interaction region. With this constraint the arc length for most tracks increased by about 30% leading to a much better momentum resolution: $\frac{\sigma_p}{p} \simeq .015\ p(\text{GeV})$.

5) Pulse heights and TOF were corrected for known shifts and drifts of offsets and gain factors. At this level a tentative particle identification for each track was made to be used in Step 6.

6) Events were classified[39] in a variety of classes (e.g. likely candidates for the processes $e^+e^- \to e^+e^-$, $e^+e^- \to \mu^+\mu^-$, $e^+e^- \to$ hadrons), or as background events (e.g. events with a vertex very near the beam pipe, cosmic rays) based on the number of tracks, vertex location and the best guess as to each particle's type.

7) Selected events were written on output data summary tapes. The selected events satisfied the following criteria:

i) Two-or-more charged tracks detected;

ii) No cosmic rays in the event;

iii) The vertex was within a large fiducial volume, roughly the size of the interior of the beam pipe ($|z| < .17$ m, $R < .1$ m).

Three classes of events merit more discussion:

a) the $e^+e^- \to e^+e^-$, Bhabha scattering candidates.

These events identified by the collinearity of the two oppositely-charged tracks, the fact that $p_{track} \simeq E_{beam}/c$, and the large pulse height in the shower counters or the Lead-Glass system, served as the "reference" class. By relating the number of events in this class, using the estimated detector acceptance, to the QED cross section:

$$\frac{d\sigma}{d\Omega}(e^+e^- \to e^+e^-) =$$

$$= \frac{\alpha^2}{8E^2}\left(\frac{1 + \cos^4(\theta/2)}{\sin^4(\theta/2)} - \frac{2\cos^4(\theta/2)}{\sin^2(\theta/2)} + \frac{1}{2}(1 + \cos^2\theta)\right)$$

an absolute value for the luminosity of SPEAR was found. This was a better value than the number derived from the luminosity

monitor which could be off by $\simeq$ 10% due to small orbit variations. The ratio of the two luminosities was typically $1.0 \pm .1$ except when running on the ψ and ψ' where processes like $e^+e^- \to \psi \to e^+e^-$ interferred with Bhabha scattering. In such a case only the luminosity monitor derived luminosity was used.

b) the $e^+e^- \to \mu^+\mu^-$, QED μ-pair candidates.

Once again two oppositely charged high-momentum collinear tracks, with the particles having a low pulse height in the shower counters or the Lead-Glass system.

This class of QED events allowed a further check on the luminosity measurement from (a) and served as a general purpose calibrating process, since events of this type have an angular distribution of the form:

$$\frac{d\sigma}{d\Omega} = \frac{\alpha^2}{16E^2}(1 + \cos^2\theta) \quad ,$$

and populate more or less evenly the angular acceptance of our detector.

c) hadronic events.

These are the events on which our results are based. These are events with 3-or-more detected tracks or events with two equal charge tracks of momentum greater than .3 GeV/c and events with two oppositely charged tracks with a coplanarity angle θ_{copl} in the range $20^o \leq \theta_{copl} \leq 160^o$. Figure 12 defines the coplanarity angle θ_{copl}.

E. MOMENTUM RESOLUTION AND PARTICLE IDENTIFICATION USING THE TIME-OF-FLIGHT SYSTEM

The results of our analysis depend crucially on two factors:

1) the momentum resolution of our apparatus.

We are trying to identify D mesons through their decays

$$D^o \to K^-\pi^+ \text{ and } D^+ \to K^-\pi^+\pi^+$$

by looking at invariant mass distributions of two or three particle combinations. The width of the characteristic peaks for the D^o at 1863.3 MeV/c^2 and at 1868.3 MeV/c^2 for the D^+

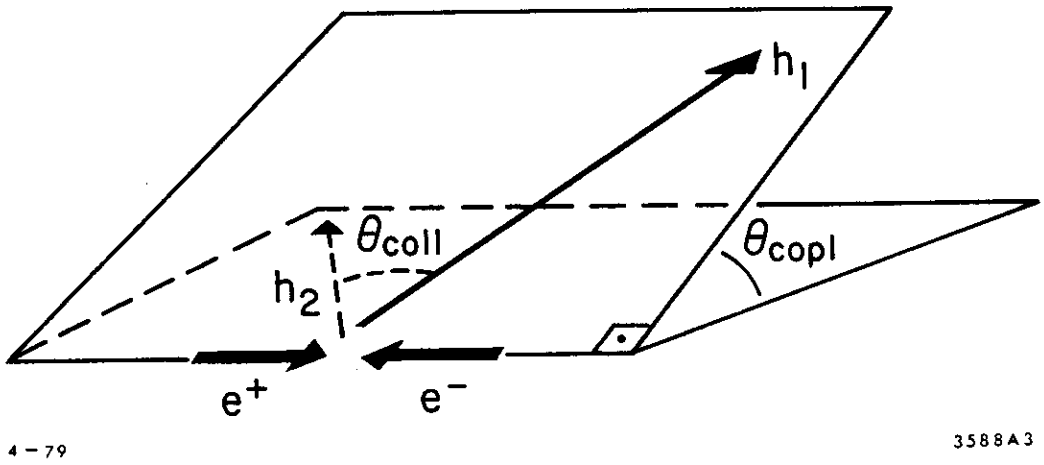

Figure 12. Illustration of the coplanarity and collinearity angles for an event with two hadrons, h_1 and h_2 .

depends directly on the accuracy with which we measure the momentum of their decay products. A better measurement results in a sharper peak and a better signal-to-noise ratio.

Our limited momentum resolution arises from two sources:

a) measurement error in the location of the sparks at the spark chambers, and

b) multiple scattering of the particles as they travel through the beam pipe and pipe counters (.011 radiation lenths), the proportional chambers (.009 radiation lengths), and the support material, gas , and wires of the spark chambers (.006 radiation lengths) all of which add up to .026 radiation lengths.

The resolution achieved in the MARK I Detector was

$$\frac{\sigma_p^2}{p^2} = [.045 * p(\text{GeV/c})]^2 + [.006]^2$$

for the regular or one-track CIRCE, and

$$\frac{\sigma_p^2}{p^2} = [.015 * p(\text{GeV/c})]^2 + [.006]^2$$

for the beam constrained CIRCE. The first term in these formulae represents the measurement error contribution which dominates over the second term which is the contribution due to multiple scattering. As a rule, we used the momentum generated by the beam constrained CIRCE, while the one-track CIRCE momentum proved valuable when searching for relatively long-lived particles (K_s^o, Λ^o) that decayed some distance away from the interaction region.

An illustration of the effect of our resolution is shown in Figs. 13(a) and 13(c). We show the expected mass width for D^o and D^+ decaying into $K^-\pi^+$ and $K^-\pi^+\pi^+$, respectively, as a function of their momentum. The width, determined from a Monte Carlo simulation incorporating our limited momentum resolution shows significant momentum dependence. For example, we find that $\sigma_m(p_D = 0) \simeq 18$ MeV/c^2 and $\sigma_m(p_D = 2.5$ GeV/c) $\simeq 40$ MeV/c^2 for the D^o. This variation has to be taken into account in our analysis.

Finally, Fig. 15(a) (page 41) is another illustration of our momentum

Figure 13 . (The figure can be found on the next page)

Monte Carlo estimates of the mass resolution and the detection efficiency for D mesons using the TOF weight technique.
The results of three different simulations for the decays $D^{o} \rightarrow K^{-}\pi^{+}$ and $D^{+} \rightarrow K^{-}\pi^{+}\pi^{+}$ are shown for comparison :
Open circles - D's produced with an angular distribution of the form

$$\frac{d\sigma}{d\Omega} = \frac{3}{16\pi} (1 + \cos^2\theta)$$

Crosses - D's produced isotropically
Solid circles- D's produced with an angular distribution of the form

$$\frac{d\sigma}{d\Omega} = \frac{3}{16\pi} (1 + \cos^2\theta)$$ but excluding any corrections for the decay-in-flight of the charged kaon.

The superposed lines are eye-ball fits to the Monte Carlo points.
The x and z scales at the bottom refer to the x and z bins used in the analysis of the high energy data of chapter 5 .

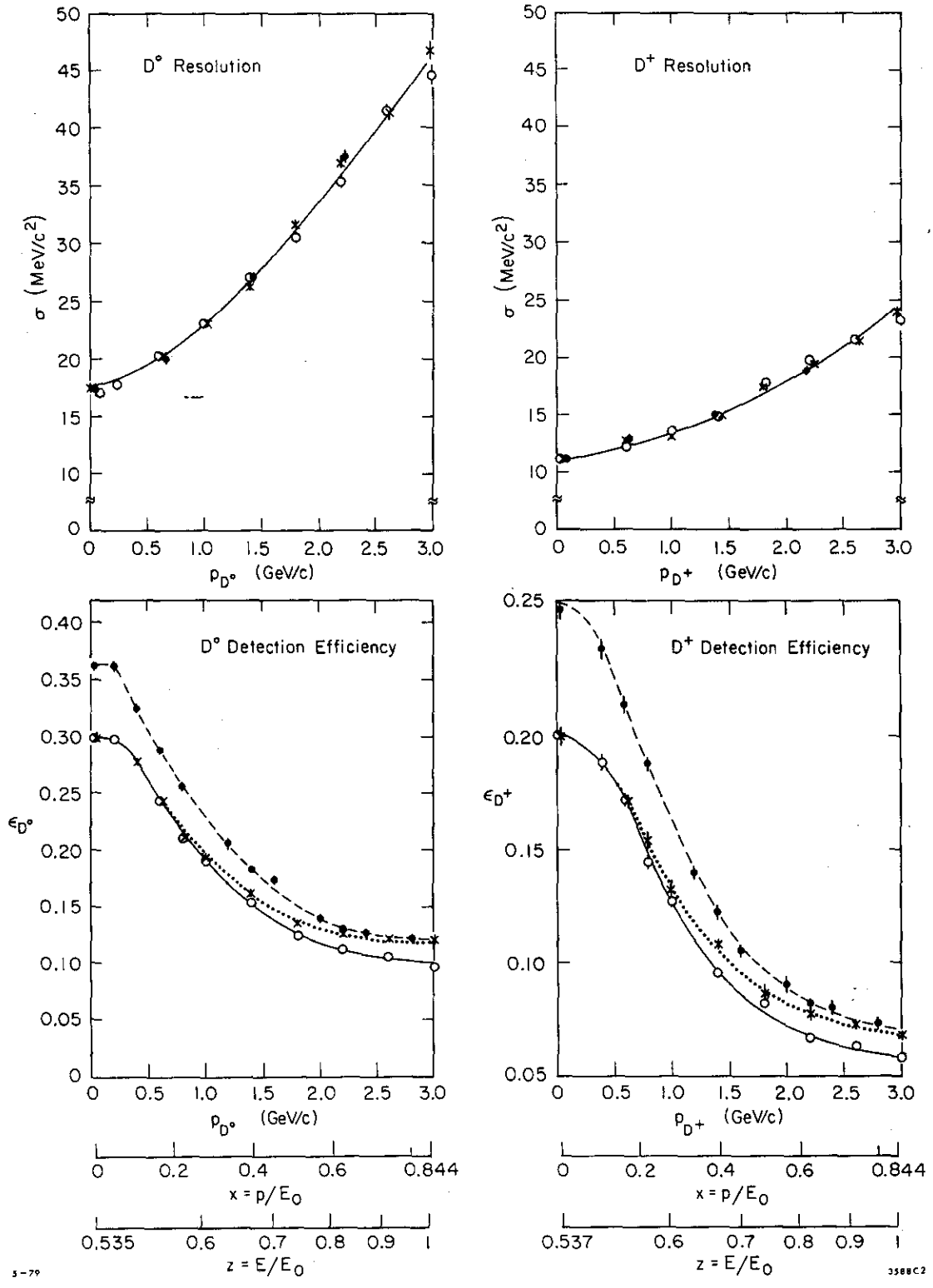

Figure 13. (The figure caption can be found on the preceding page)

resolution. We plot the ratio E_μ/E_{beam} for muon pairs produced at $E_{c.m.} = 7.4$ GeV (E_μ is the energy of the muon given from $E_\mu^2 = p_\mu^2 + m_\mu^2$). The superposed line is the shape expected for a momentum resolution of $\frac{\sigma_p^2}{p^2} = (0.015 * p(\text{GeV/c}))^2 + (0.006)^2$.

2) the time-of-flight resolution

The timing information provided by the 48 trigger counters affords the only means of separating heavy particles from lighter ones. As such, it was the only measurement that allowed us to identify particular tracks as charged pions, charged kaons or protons.

The importance of this system is amply illustrated by the fact that the D mesons were discovered[46,47] through the use of this information while an earlier search that did not make use of it failed.[48]

The signal from each trigger counter phototube was divided in two, the one half was used to provide pulse height information, and the other half was used in conjunction with the beam crossing signal derived from the beam pick-off electrode to provide timing information (see Fig. 14).

In the off-line analysis the TDC, ADC readings and the z intercept of a track with a trigger counter were used to derive a corrected time-of-flight for each track. The correction formulae were:

$$(F)_{i,k} = T_{i,k} \cdot g_{i,k} - C_{i,k} - t_o - a_1 + (-1)^k \left[(a_2 + V_i)z + a_3 z^2\right] + \frac{1}{a_4 + a_5 H_{i,k}} + \frac{a_6 z_c \, e^{a_7 z_c^2 + a_8 z_c}}{H_{i,k}} \qquad (1)$$

$$(TOF)_i = \left\{\frac{F_{1i} - z/c\beta_c}{b_1 z_c^2 + b_2 z_c + b_3} + \frac{F_{2i} + z/c\beta_c}{b_1 z_c^2 + b_2 z_c + b_3}\right\} \div \left\{\frac{1}{b_1 z_c^2 + b_2 z_c + b_3} + \frac{1}{b_1 z_c^2 + b_2 z_c + b_3}\right\} \qquad (2)$$

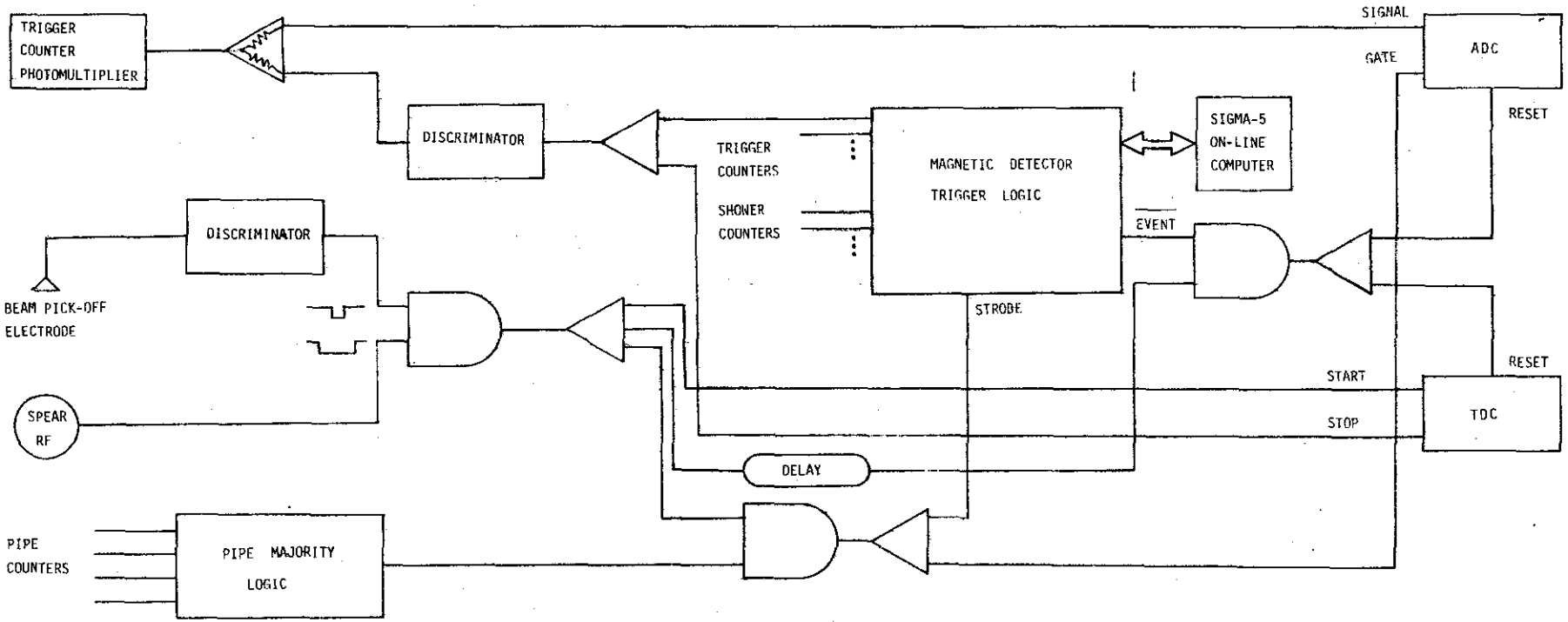

Figure 14. Block diagram of the time-of-flight electronics.

where:

k is 1 or 2 for the North or South phototube,

i is 1 through 48 for the trigger counter being considered,

$T_{i,k}$ is the raw TDC reading for each phototube,

$g_{i,k}$ is the conversion factor ($\simeq$ 5 counts/nsec) for each TDC,

$C_{i,k}$ is an adjustable offset for each counter,

t_o is an overall offset for all counters,

V_i is the signal propagation speed for each counter,

$H_{i,k}$ is the pulse height,

z is the z intercept for a track and the trigger counter,

z_c is $(L/2 - |z|)$, the distance between the phototube and the intercept of a track with the trigger counter

a,b are constants,

c is the speed of light,

β_c is the average signal propagation speed for all trigger counters ($\simeq$ .53),

$(TOF)_i$ is the time-of-flight for a track pointing to trigger counter i.

The term in square brackets in (1), corrects for the z dependence, the second to last term for pulse height slewing and the last term for attenuation due to multiple reflections in the scintillator. The weighted sum in Eq. (2) assigns a greater weight to the measurement derived from the phototube that was closer to a track's trajectory. This weighting improves our TOF resolution by about .05 ns.

The constants a and b were determined once for all, while g_i and v_i were adjusted very infrequently ($\simeq$ every year), the $C_{i,k}$ were adjusted every one or two weeks and t_o was re-determined for every run (i.e. once every two or three hours). The objective of these laborious and complicated adjustments was to minimize the resolution of the TOF system and thus increase its particle-identifying capability. For this minimization procedure e^+e^- elastic scattering events were used, since they travel with $\beta \simeq 1$ and their expected flight time is accurately known once their trajectory (or equivalently their momentum) has been determined.

The achieved resolution was of the order of $\sigma \simeq .37$ ns, and is illustrated in Fig. 15(b). Figure 16 shows a mass plot for tracks in hadronic events as determined from the time-of-flight system and their momenta. As we see, for high momenta we cannot separate particle types unambiguously, the π/K separation starts being problematical at p = 1.0 GeV and the K/p separation at p = 1.5 GeV. Nevertheless, the TOF information allows particle identification on a statistical basis through the use of the weight technique.[46-49]

Each particle in an event is assigned a weight proportional to the probability that it is a π, K, or p. These weights are determined from the measured time-of-flight and momentum of each particle:

$$\text{e.g. } W_i(\pi) \propto e^{-(t_{measured} - t_{expected})_i^2/2\sigma^2}$$

where $t_{expected}$ is the expected flight time of a particle being a π, having the measured momentum and following the observed trajectory in our apparatus and σ is the measured resolution of the time-of-flight system. When we are investigating particular multi-particle combinations, e.g. $K^+\pi^-$ for the D^o, all possible combinations of tracks and particle hypotheses are made with each combination weighted by the joint probability that the tracks satisfy the particular particle hypotheses assigned to them. For example: for two tracks (1 and 2) of opposite charge to form a D^o or a $\bar{D}^o$ the weight associated to the combination under the hypotheses that track 1 is a π and track 2 is a K would be

$$W_D = \frac{e^{-(t_m - t_\pi)_1^2/2\sigma^2} \cdot e^{-(t_m - t_K)_2^2/2\sigma^2}}{\sum_{\alpha=\pi,K,p} e^{-(t_m - t_\alpha)_1^2/2\sigma^2} \cdot \sum_{\beta=\pi,K,p} e^{-(t_m - t_\beta)_2^2/2\sigma^2}}$$

On occasion, a threshold was imposed on the weight associated with a combination in order to improve the signal-to-noise ratio, or a variation of the above technique was used: the particle hypothesis for a track with the highest weight was assigned a weight of 1.

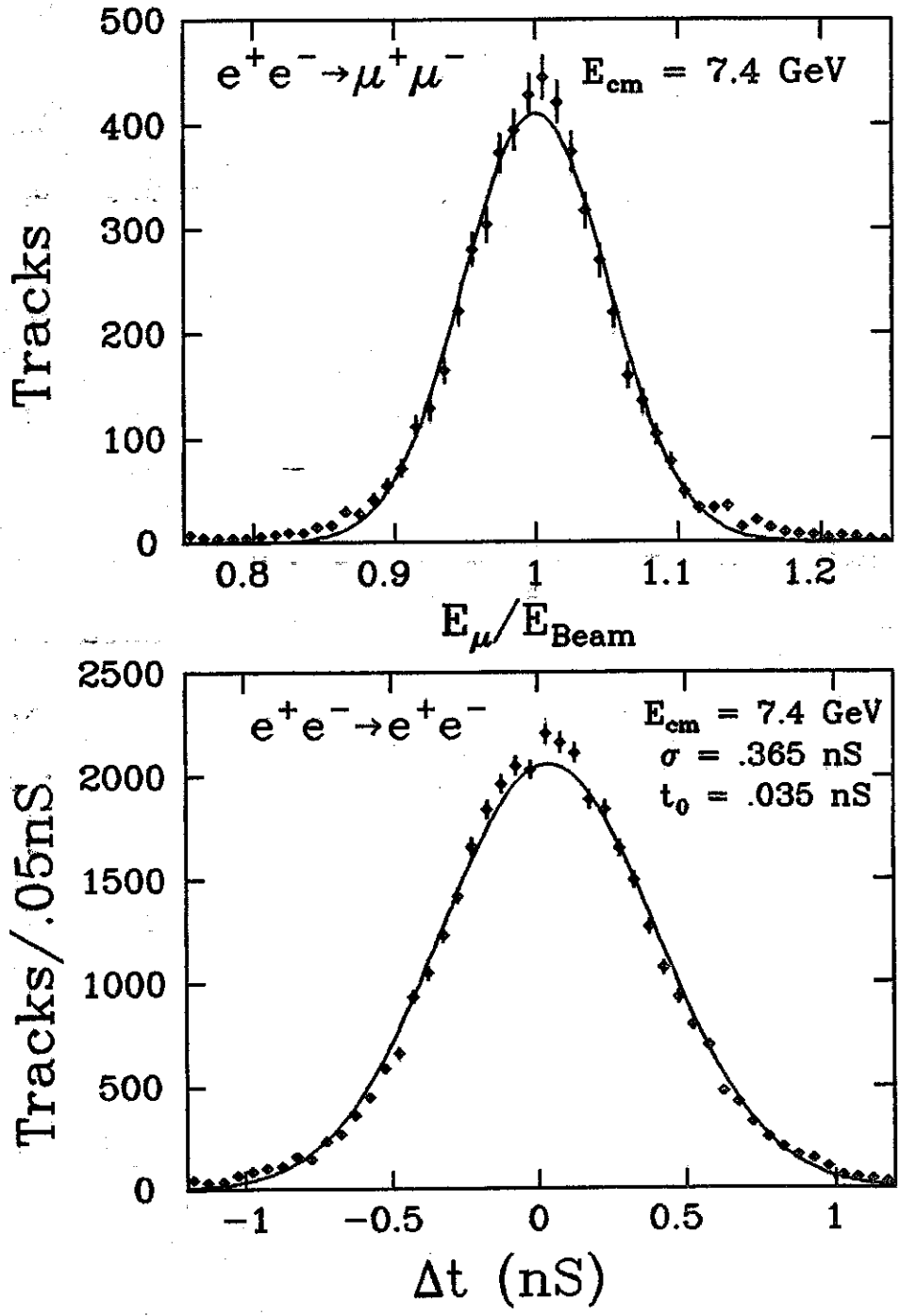

Figure 15 . (a) Ratio of muon energy to beam energy for $e^+e^- \to \mu^+\mu^-$ events at $E_{c.m.}$ = 7.4 GeV. The superposed shape is described in the text.

(b) Difference between expected and measured time-of-flight of electrons in $e^+e^- \to e^+e^-$ events at $E_{c.m.}$ = 7.4 GeV. The data of this graph are approximately 30% of the data used in the analysis of chapter 5. The parameters of a fit of a Gaussian to this data are shown in the figure.

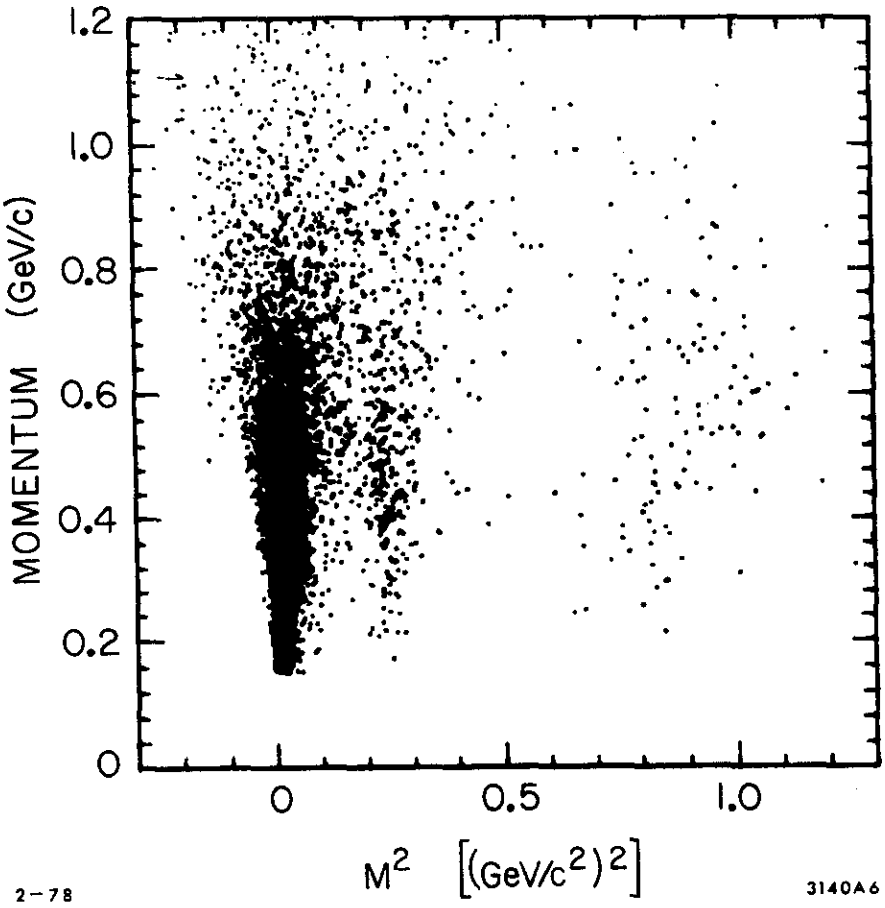

Figure 16. Mass squared for each track, reconstructed from TOF and momentum measurements versus momentum. The data are from multi-track events at the $\psi(3095)$.

There are some important points that need to be emphasized:

a) Particles may not have a good time-of-flight measurement. This may be due to counter inefficiency ($\leq 1\%$), or more frequently due to the fact that either two particles hit the same trigger counter or a particle was produced with a large polar angle θ so that it passed near the edge of the spark chambers and did not hit the trigger counters. As a rule, tracks with unreliable time-of-flight information were called pions (since pions are the majority of particles produced) or were not used. A correction for these losses has to be made in the analysis procedure.

b) The hypotheses allowed, $\pi/K/p$, do not include the cases of electrons or muons. While we have to correct for this in the case of single particle inclusive distributions, in the case of D meson studies, combinations that include a missidentified lepton populate the invariant mass distributions more or less uniformly and are simply a background under the peaks that correspond to the charmed mesons. There is no need to explicitly correct for this effect.

c) This is a statistical technique and its results cannot be interpreted in a naive manner. What we mean can be illustrated by the following hypothetical case: If no K's were produced in e^+e^- annihilation this analysis technique would generate erroneous kaons. The interpretation of a result has to be made by comparison with a Monte Carlo simulation of the looked-for process in our detector.

The last point, being of paramount importance, will be illustrated by describing in detail the techniques used in obtaining the rate of inclusive $K^{\pm}$ and D production.

In the case of charged kaons, the TOF system provides unambiguous K-π spearation (i.e. $> 3\sigma$) for momenta up to .65 GeV/c, and partial K-π separation (i.e. $> 1\sigma$) for momenta up to 1.2 GeV/c. For momenta smaller than .65 GeV/c, the number of kaons obtained using the normalized TOF weights is the same as the one obtained by a straight cut in the TOF derived mass of the track and no

explicit correction for misidentification is needed. For momenta in the range .65 to 1.0 GeV/c we must correct for the resolution of the TOF system: We compute the 3 × 3 matrix of π, K, and p identification probabilities as a function of momentum. The diagonal elements of this matrix give the probability that a particle is correctly identified while the off-diagonal elements give the misidentification probabilities. Figure 17, shows the values of the matrix elements as a function of momentum; we observe, as expected, that for low momenta the diagonal elements have values close to unity, while for high momenta all the elements tend towards the asymptotic value of 1/3.* The inverse of this matrix relates the observed (and weighted) π/K/p rates to the produced rates. From a Monte Carlo simulation we have found that this gives the correct number of charged kaons but with an error larger than the statistical one.

For momenta higher than 1.2 GeV/c the above method deteriorates rapidly and we have to resort to a different method. We extrapolate the observed kaon momentum spectrum by fitting it to an exponential. This correction is of the order of 10% at $E_{c.m.}$ = 4.0 GeV and gets worse as the c.m. energy gets higher. For this reason, we chose not to report any measurements for charged kaon production for c.m. energies greater than 5 GeV. We have checked that this correction is consistent with the fraction of K^o_s (for which our acceptance for momenta greater than 0.4 GeV/c shows little momentum dependence) with momenta greater than 1.0 GeV/c.

In the case of inclusive D production at higher energies, we evaluated the efficiency for detecting a D meson as a function of momentum through a Monte-Carlo simulation that incorporated

*This is easily seen if one makes the observation that the matrix elements are the average weight for a particle of type i to be called a particle of type j. At high momenta, where the TOF provides almost no information, particle identities are assigned almost randomly and the average weight is 1/3.

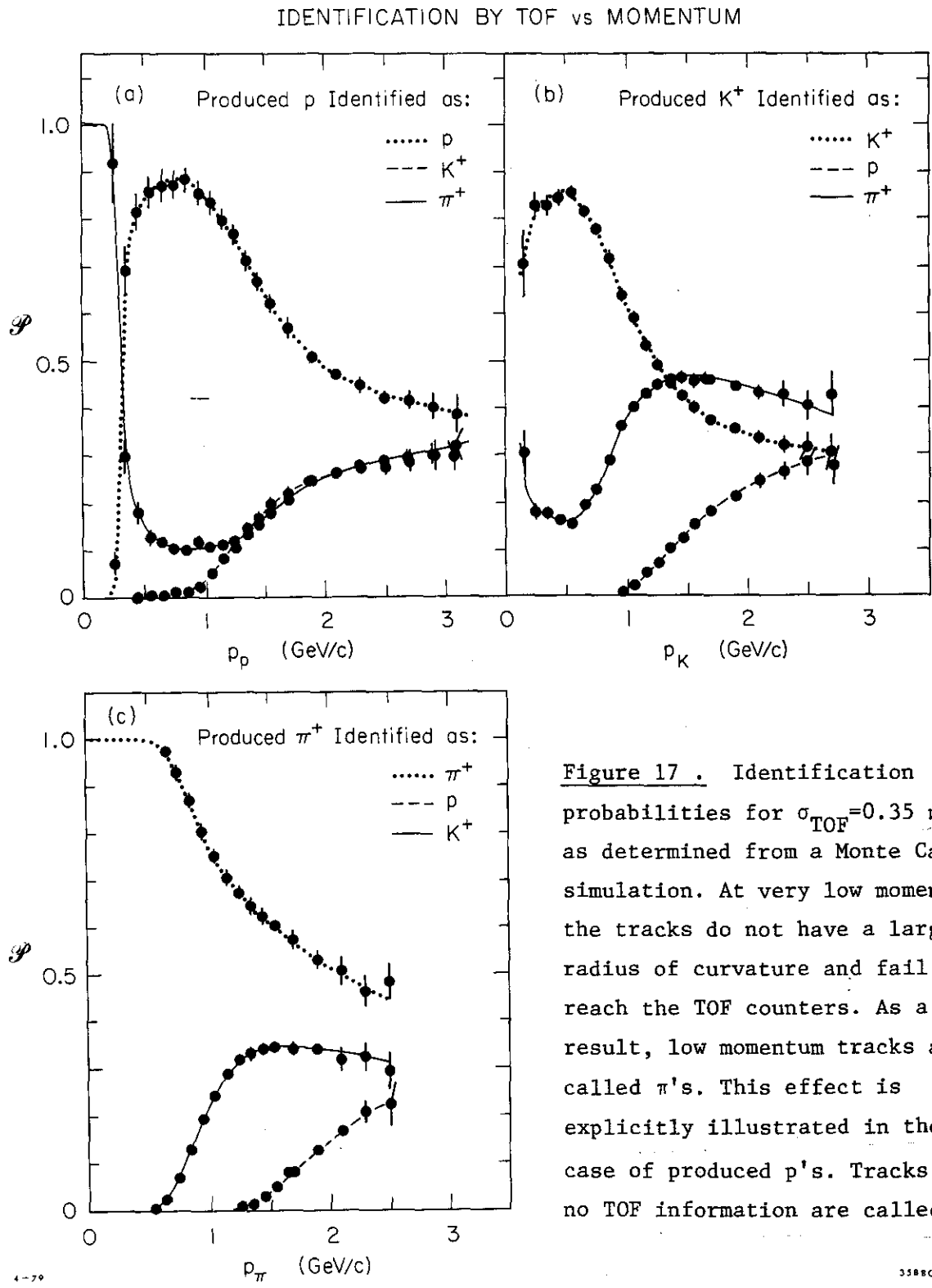

Figure 17 . Identification probabilities for σ_{TOF}=0.35 ns as determined from a Monte Carlo simulation. At very low momenta the tracks do not have a large radius of curvature and fail to reach the TOF counters. As a result, low momentum tracks are called π's. This effect is explicitly illustrated in the case of produced p's. Tracks with no TOF information are called π's.

the effects of the geometric acceptance of our detector, of the TOF resolution, of the kaon decay in flight, as well as the effects of non-isotropic production (if any) of the D's. Figures 13(b) and 13(d) show this efficiency for the two extreme production models, isotropic D production and $1 + \cos^2\theta$ distribution. This efficiency was used to correct the number of observed weighted D^o's and D^+'s in a particular momentum interval.

F. K^o IDENTIFICATION

Neutral kaons were identified through their decay $K_s^o \to \pi^+\pi^-$. Our technique[50] can be summarized as follows: First the event was projected on the x-y plane, i.e. the plane normal to the beams, and for every charge zero two particle combination with an opening angle in the x-y plane greater than 10^o and smaller than 170^o an intersection was determined. In general, the trajectories intersect at two points. Only the intersection closer to the origin (intersection of the e^+e^- beams) was considered. The projected distance of this intersection from the origin was required to be greater than 0.4 cm and smaller than 16 cm, i.e. just inside the first wire chamber, and, in any case, greater than five standard deviations from zero. The vertex location in the x-y plane is checked using the z coordinate: if the two tracks were separated by more than 15 cm along the z direction they were rejected. For the pairs that survived these cuts we required that their invariant mass be in the range 0.47 to 0.52 GeV/c^2. Furthermore, the vertex position was required to be consistent with the flight path of a kaon: the angle ξ between the three dimensional vector defined by the origin and the decay vertex and the momentum of the kaon (as determined by the vector sum of the momenta of the two particles) had a) to be smaller than four standard deviations from zero and b) to be smaller than 60^o.

Figure 18(a) shows the $\xi/\Delta\xi$ distribution with the four standard deviation cut indicated, and Fig. 18(b) shows the two particle invariant mass distribution after all the other cuts were applied. The signal-to-noise ratio is approximately 2.5.

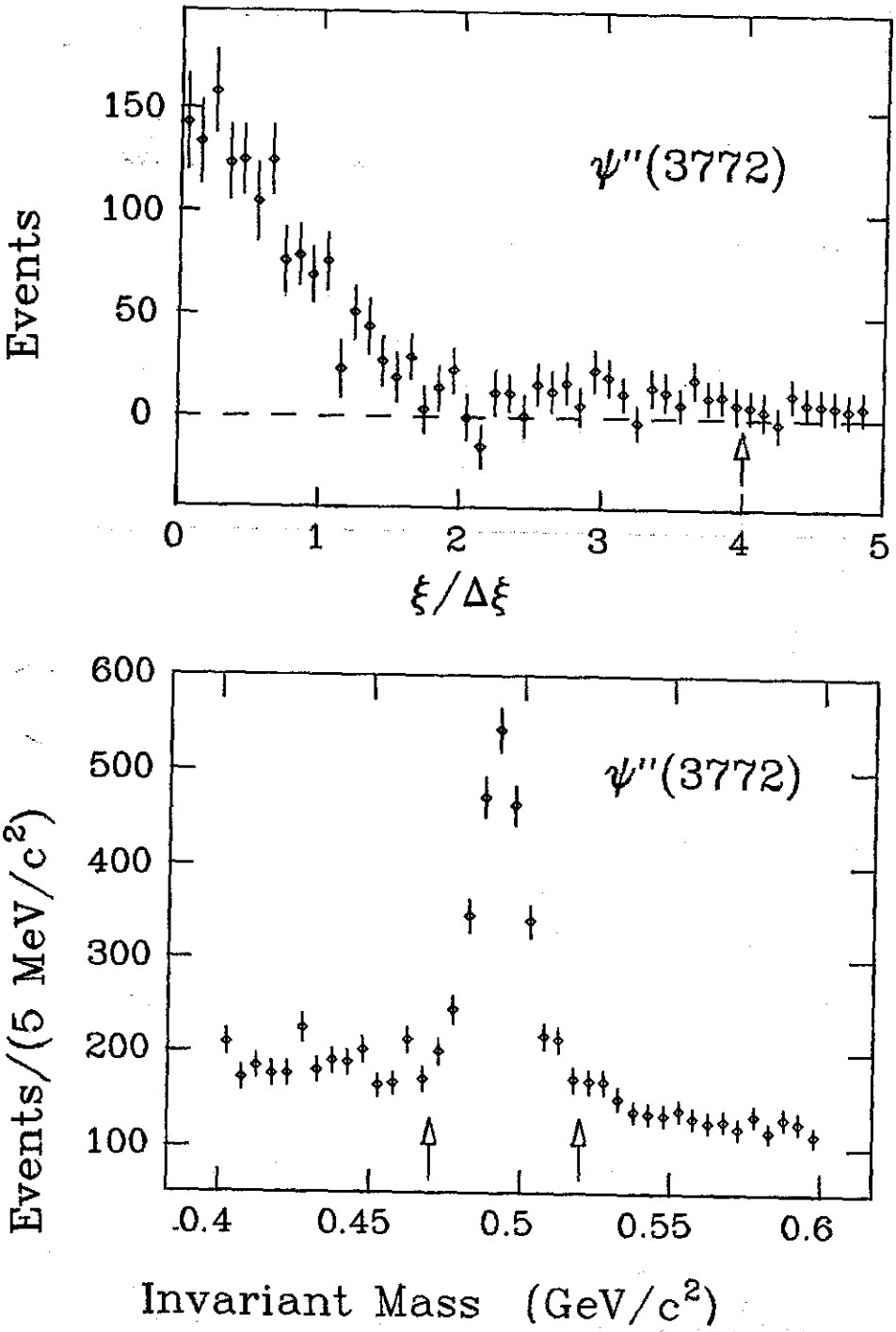

Figure 18 . Identification of the decay $K^o_s \to \pi^+\pi^-$ in hadronic final states produced at the ψ"(3772) : (a) $\xi/\Delta\xi$ distribution for the angle ξ (defined in the text) for K^o_s candidates selected by cuts on the vertex position and opening angle. The invariant mass of the pair was required to be greater than 0.47 and smaller than 0.52 GeV/c^2. Backgrounds estimated from events in adjacent invariant mass ranges have been subtracted. The cut in $\xi/\Delta\xi = 4$ is indicated by the arrow. A typical value of $\Delta\xi$ is 9^o. (b) Invariant mass of the pion pairs after all other cuts were applied.

G. MONTE CARLO SIMULATION; DETECTOR EFFICIENCY

In order to obtain physically significant quantities from our measurements we have to correct for the efficiency of our apparatus. Our efficiency is roughly determined by the geometric acceptance of the detector but other factors such as the bias associated with the two-particle trigger, angular correlations between the particles in a final state, and the momentum and position dependent shower counter efficiency, complicate the picture to the point that the only reliable estimate for its value has to be obtained through a Monte Carlo simulation.

In this simulation[4] events were generated according to either Lorentz-invariant phase space or a jet model in which phase space was modified by a matrix element squared of the form $H^2=e^{-\Sigma p_T^2/2b^2}$ where p_T is the momentum perpendicular to a jet axis. The jet axis angular distribution was of the form $\frac{d\sigma}{d\Omega} \propto 1 + \alpha \cos^2\theta$; where θ is the polar angle relative to the e^+ beam. In both models either only charged and neutral pions were produced or kaons, etas and nucleons were also included to provide a more realistic representation of the final states in the e^+e^- annihilation process. The total multiplicity was given by a Poisson distribution. The simulation included the geometric acceptance, trigger efficiency, wire chamber inefficiencies, momentum resolution, conversion probability of photons and all the other features of the detector (including a simulation of the TOF system).

The parameters of the Monte Carlo (produced multiplicities, particle type fractions, α, b, etc...) were adjusted in a way such that the Monte Carlo derived average observed charged-particle multiplicity and the median observed charged-particle momentum agreed with the same quantities derived from the real data. This Monte Carlo calculation resulted in a matrix of efficiencies for detecting a certain number of particles for each charged particle multiplicity in the final state. The produced multiplicity distribution was then obtained through an unfolding procedure as the maximum-likelihood solution to an over-determined set of linear equations. The average detection efficiency was simply the ratio of detected to produced events.

The average overall detection efficiency,[51] for detecting hadronic events, shown in Fig. 19, is a slowly rising function of the energy and can be approximated by a simple analytic formula. The efficiency seems to be an almost linear function of the mean multiplicity (Fig. 20). The increase in efficiency as a function of energy can be accounted by an increase in mean multiplicity as the energy rises.

The efficiency for single particle inclusive production can be evaluated in two different ways. For simplicity we will discuss the case of D mesons, similar considerations apply, mutatis mutandis, to the case of kaons.

One approach is to produce a variety of specific final states, e.g. $D\bar{D}$, $D\bar{D}^*$, $D^*\bar{D}^*$, $D\bar{D}^*\pi$, $D\bar{D}\pi\pi$ etc., and choose a mixture of these states in a manner such that the momentum spectrum and angular distribution of the D's, together with the overall multiplicity and average charge particle momentum obtained from the Monte Carlo agree with the observed ones. From this study, an overall efficiency can be obtained in a single step. We used this technique in the study of D meson production in the c.m. energy range 3.7 to 5.8 GeV, where the final states with D's are rather easy to simulate.

The alternative approach is to determine the efficiency as a product of two terms:

$$\varepsilon = \varepsilon_D(p_D) \cdot \varepsilon_T(p_D, E_{c.m.}) \quad .$$

The first term, ε_D is the efficiency for detecting D mesons of a fixed momentum decaying into $K^-\pi^+$ or $K^-\pi^+\pi^+$. This part of the efficiency, which depends on the momentum and angular distribution of the D's as well as the geometric acceptance of the apparatus and the TOF resolution, is the correction shown in the lower half of Fig. 13.

The second term, ε_T, is the probability for an event with a detected D to trigger our apparatus and satisfy our event selection criteria. This quantity depends on the multiplicity and dynamics of final states containing D's. Its accuracy is limited by our lack of knowledge about the production mechanism. In the case of D's, this limitation is not a significant factor since the multiplicity of events with D's is relatively high. ε_T is larger than .9 for a wide variety of models.

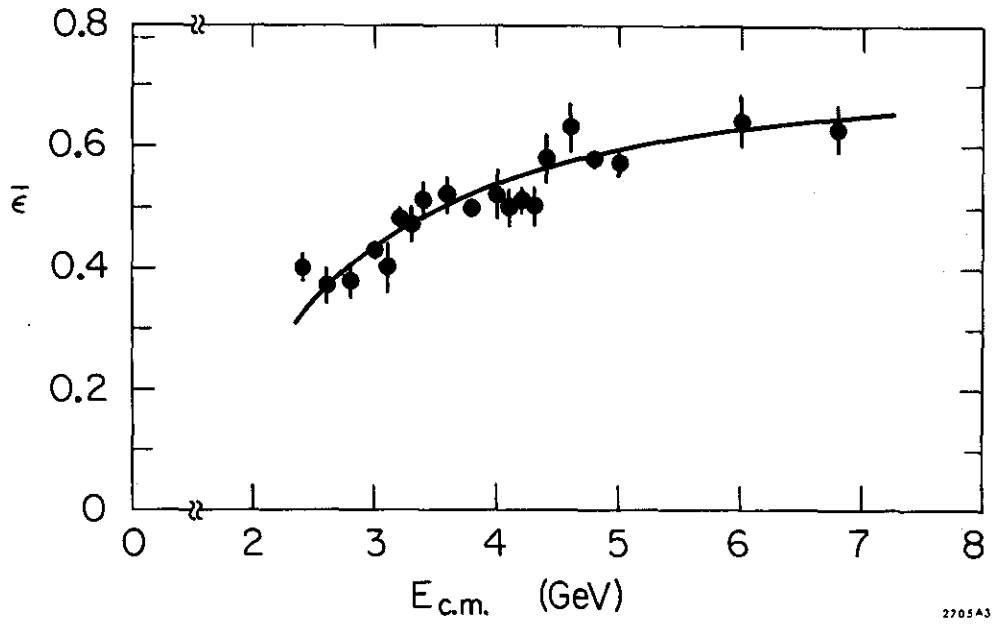

Figure 19 . Average detection efficiency for detecting hadronic events versus $E_{c.m.}$. The smooth curve, which was used in the cross section determination of chapter 3, is given by :

$$\bar{\epsilon} = \left[0.186 + \ln(E_{c.m.}/2)\right] \; / \; \left[0.955 + \ln(E_{c.m.}/2)\right] .$$

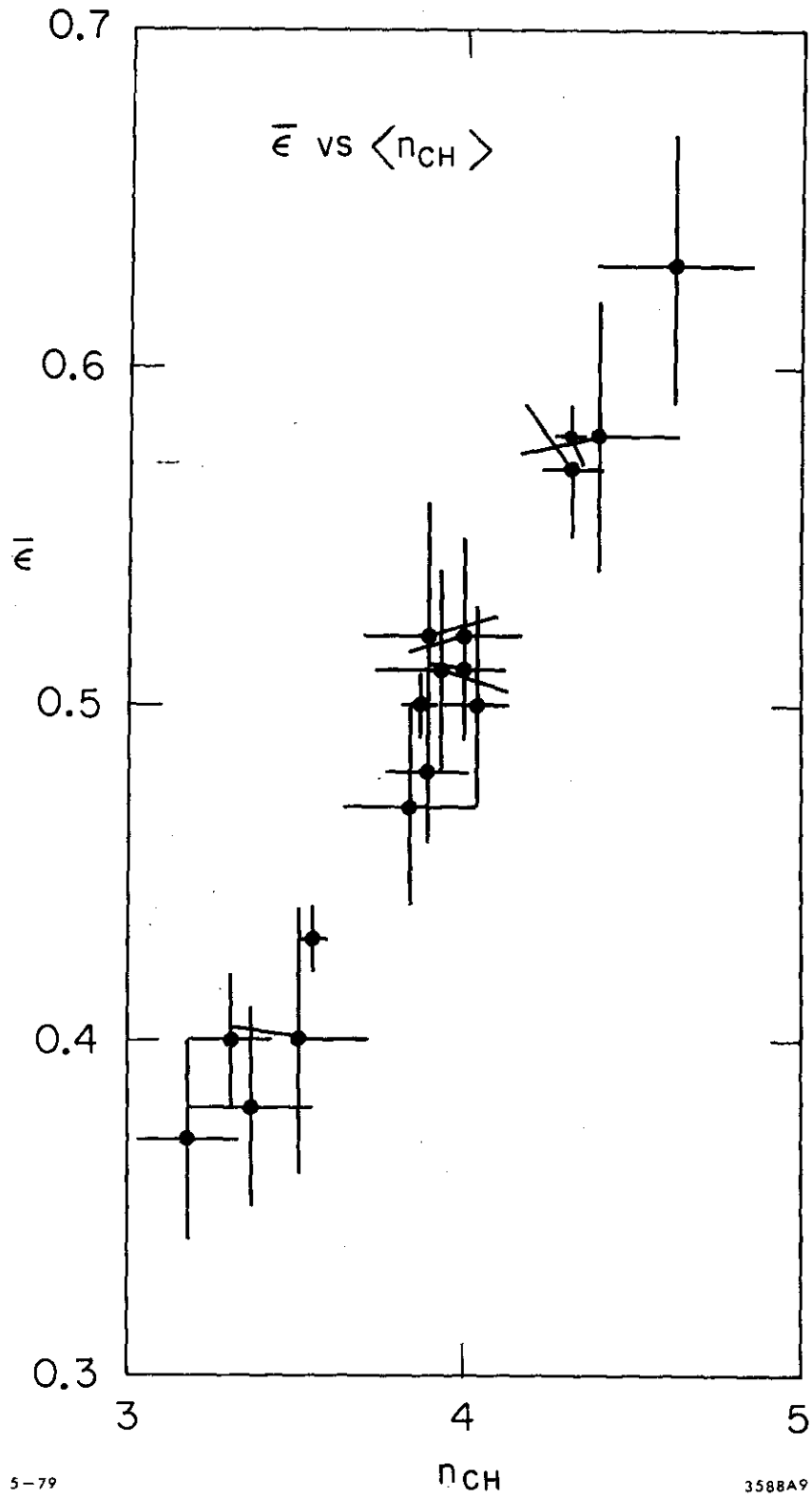

Figure 20. Average detection efficiency for hadronic events vs. mean produced charged-particle multiplicity. Each data point corresponds to a different center of mass energy.

In the case of kaons, this term is less accurately determined. In the Monte Carlo simulation used to determine ε_T, the detected kaon momentum spectrum, the average multiplicity and momenta of all detected charged particles have been adjusted to agree with the data for the various c.m. energies under study. These parameters are found to be the most critical in the determination of the trigger efficiency. They vary smoothly and slowly as a function of c.m. energy. Likewise, ε_T is a smooth function: it increases for increasing energy because the multiplicity of the final state rises, ε_T decreases with increasing kaon momentum. These model calculations include corrections due to particle correlations described by the formation of jets.

CHAPTER III

D MESON PRODUCTION AT $E_{c.m.} = 3.772$ GeV/c^2

A. THE ψ'' (3772)

The most striking feature of the total cross-section of e^+e^- annihilation into hadrons, with the exception of the very narrow $\psi(3095)$ and $\psi(3684)$, is the structure observed in the energy range $E_{c.m.} = 3.77 - 4.5$ GeV. The most distinctive landmark in this region is a rather narrow peak at 3.772 GeV, the $\psi(3772)$. (In the rest of this work we will refer to the $\psi(3095)$, $\psi(3684)$, and $\psi(3772)$ as ψ, ψ', and ψ'' respectively.) This resonance[52,53] occurs just above the threshold for charmed meson production and is, as we shall see, almost totally due to $D\bar{D}$ production. The ψ'' is an interesting object for study, not only in its own merit, as a confirmation of quarkonium predictions, but because it also provides a rich source of kinematically well-defined and relatively background-free D mesons for study.

The events used for this total cross-section analysis are hadronic events, as described in the previous chapter. Events were accepted if the reconstructed vertex lay in the region $-.12\ m < z < .1\ m$ and $R < .04$ m. Events with a vertex in the two regions $-.12\ m > z > -.17\ m$ and $.1\ m < z < .17\ m$ with $R < .04$ m, were used to estimate the background from beam-gas interactions. Runs taken with single beams have a uniform longitudinal distribution of the vertices; colliding-beam runs show, in addition, a peak corresponding to the overlap region of the beams[54] ($-.12\ m < z < .1$ m). This subtraction was of the order of 2%. Events with $-12\ m < z < .1$ m and $.04\ m < R < .06$ m were used to estimate the loss due to the radial cut. Studies of radial vertex distributions and visual scanning of earlier data[54] show that such losses do not favour any particular multiplicity. This loss was approximately 9% and the data were corrected for it.

The contamination from two-photon processes was estimated from an

earlier study[40] that used the small-angle (25 mrad) luminosity monitor counter in coincidence with the main detector to tag one or both of the forward-angle electrons and positrons that characterize these processes. This was a rather small correction (<1%).

To correct for the inefficiency of the apparatus we used the average efficiency $\bar{\varepsilon}$ mentioned in the previous chapter. The use of such a simplistic form of the efficiency can only be justified if the most salient features of the data (the observed mean particle momentum and the observed mean charged-particle multiplicity) vary smoothly, and slowly, with energy over the region of interest. Figure 21 shows the variation of these quantities with $E_{c.m.}$.

There does not appear to be any significant structure, with the exception that the observed multiplicity is higher in the region where ψ' radiative tail is important. This is caused by the relatively high multiplicity in ψ' decays. As a consequence of using a smooth function for $\bar{\varepsilon}$, we measure a slightly larger magnitude for the ψ' tail than we would if we used a locally varying $\bar{\varepsilon}$; however, since we subtract the ψ' tail experimentally using the same technique, as will be discussed below, no error is introduced in the determination of radiatively corrected cross-sections. The values of $\bar{\varepsilon}$ used vary from 0.51 at $E_{c.m.} = 3.7$ GeV, to 0.53 at $E_{c.m.} = 3.9$ GeV.

Rather than displaying σ_T (the total cross-section) directly, we follow the usual practice of plotting the ratio R of σ_T to the theoretical cross-section for production of muon pairs. Figure 23(a) shows R before radiative corrections. The error bars represent only the statistical uncertainties. There is an additional overall systematic uncertainty of 15%, arising largely from the uncertainty in $\bar{\varepsilon}$. There is clearly an enhancement near 3.77 GeV, but it is partially obscured by the ψ' radiative tail.

Corrections for radiative effects[55-57] in the initial state can be divided into four parts: the radiative tail of the ψ', the radiative tail of the ψ, the correction due to the continuum and the correction due to the resonance itself. All four of these corrections have the same physical process as their origin and the division into these four parts is arbitrary but convenient.

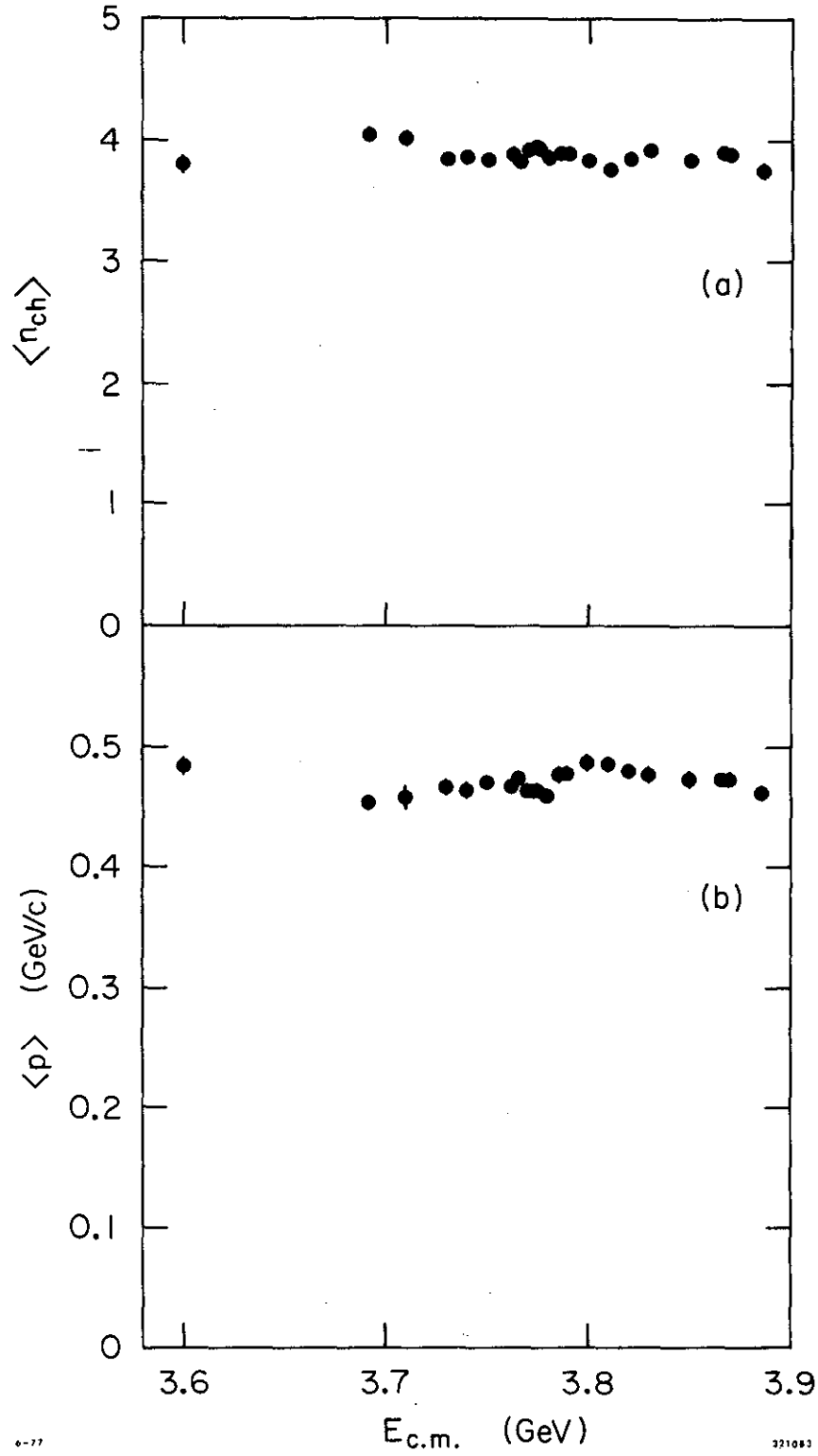

Figure 21. (a) Observed mean charged-particle multiplicity, and (b) mean charged-particle momentum vs. $E_{c.m.}$.

The radiative corrections to the lowest order diagram (Fig. 22(a)), which is the one used in theoretical discussions of e^+e^- annihilation, including the second order diagrams in Figs. 22(b) and 22(c) were first derived in a convenient form by Bonneau and Martin.[55] Their formula 16 reads (with minor modifications):

$$\sigma_{OBSERVED} = \sigma(S_o)\ \varepsilon(S_o)\ (1 + \delta) \tag{1}$$

$$\delta = \frac{2\alpha}{\pi}\left[\frac{\pi^2}{6} - \frac{17}{36} + \left[2\ \ell n\ \frac{2E}{m_e} - 1\right] \times \left(\frac{13}{12} + \right.\right.$$

$$\left.\left. + \int_o^E \frac{dK}{K} \cdot \left[\left(1 - \frac{K}{E} + \frac{K^2}{2E^2}\right) \frac{\sigma(S)\ \varepsilon(S)}{\sigma(S_o)\ \varepsilon(S_o)} - 1\right]\right)\right]$$

where $\varepsilon(S)$ = our apparatus detection efficiency, $S_o = 4E^2$, E = beam energy, $S = 4E(E-K)$, K = energy of radiated photon. Rewriting this formula, as done by Jackson and Scharre,[56] we have

$$\sigma_{OBSERVED}\ (S_o) = \sigma(S_o)\ [1 + \xi] + \tag{2a}$$

$$+ t\int_o^E \frac{dK}{K}\ (\sigma(S)\ \varepsilon(S) - \sigma(S_o)\ \varepsilon(S_o)) -$$

$$- \frac{t}{E}\int_o^E dK\left(1 - \frac{K}{2E}\right)\ \sigma(S)\ \varepsilon(S)$$

where

$$\xi = \frac{2\alpha}{\pi}\left(\frac{\pi^2}{6} - \frac{17}{36}\right) + \frac{13}{12}\ t \tag{2b}$$

and

$$t = \frac{2\alpha}{\pi}\left[2\ \ell n\ \frac{2E}{m_e} - 1\right]$$

In formula (2a) the three different parts can be given a direct physical meaning: the first term corresponds to radiative modifications of the vertex form factor due to vacuum polarization and mass renormalization as well as a part of the external Bremsstrahlung which is independent of K; the second term corresponds to soft photon emission and the last term to hard photon emission.

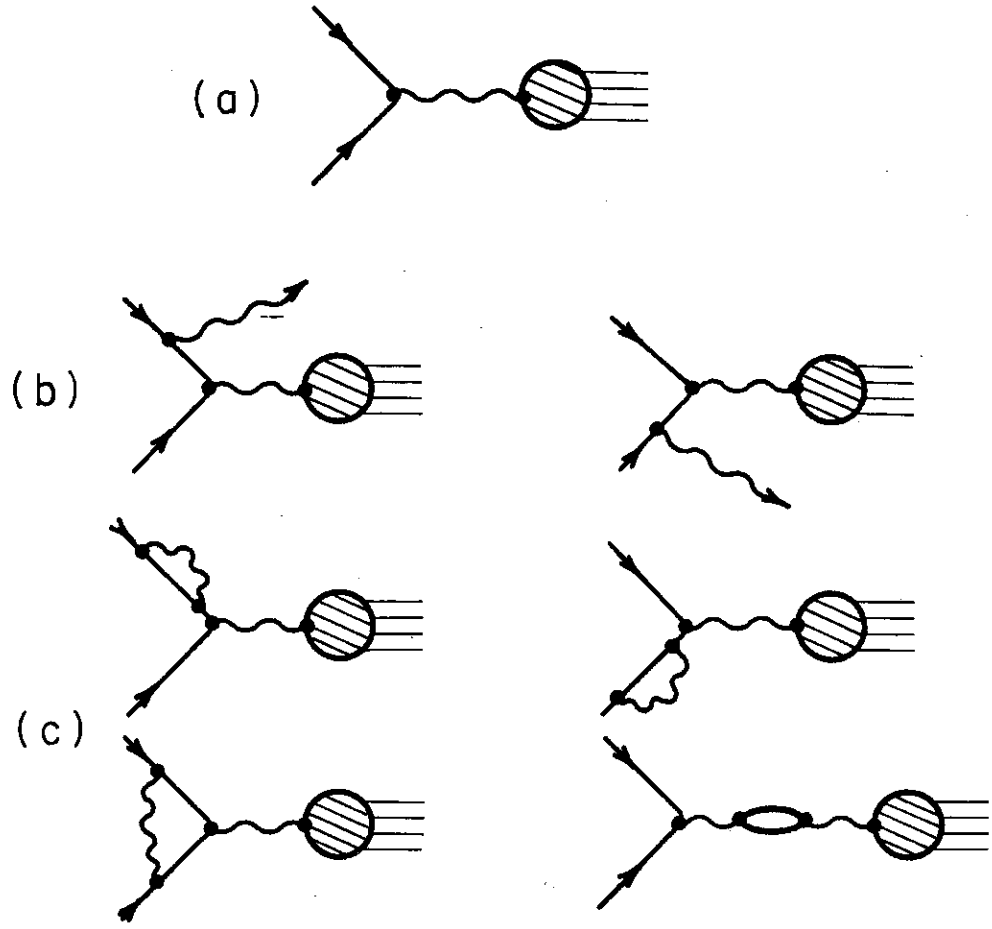

Figure 22 . QED diagrams for initial-state radiative corrections for e^+e^- annihilation via one-photon exchange.
(a) lowest order diagram,
(b) higher order diagrams involving real (soft) photon emission, and
(c) higher order diagrams involving one additional virtual photon.

The last term is significant only when K is large. The second term becomes important when there is significant variation of the cross-section in the near vicinity of the energy we are interested in and is the one that gives rise to the radiative tails of resonances. In such a case the summation of the infinite number of soft photons leads to the usual exponentiation prescription, and in the vicinity of a resonance we have:

$$\sigma_{\text{OBSERVED}}(S) = \sigma(S_o)\,\varepsilon(S_o)\,(1+\xi) +$$

$$+ t\int_o^E \frac{dK}{K}\left(\frac{K}{E}\right)^t \left(\sigma(S)\,\varepsilon(S) - \sigma(S_o)\,\varepsilon(S_o)\right) + \text{hard photon term} =$$

$$\sigma(S_o)\,\varepsilon(S_o)\xi + t\int_o^E \frac{dK}{K}\left(\frac{K}{E}\right)^t \sigma(S)\,\varepsilon(S) + \text{hard photon term}$$

For a narrow resonance like the ψ, ψ' we have (as shown by Jackson and Scharre):[56]

$$\sigma_{\text{OBSERVED}}(2E) = t \cdot A \cdot \left(\frac{2(E-E_o)}{E}\right)^t \left(\frac{1}{2(E-E_o)} - \frac{1}{E} + \frac{E-E_o}{E^2}\right) \quad (4)$$

where

$$A = \frac{A_o \cdot \varepsilon(E)}{\left(\frac{2\sigma}{t}\right)^t + \xi}$$

and $A_o = \int\sigma(S)dS$ is the are of the resonant cross-section in the absence of radiation. The original Bonneau-Martin formula gives the underlined terms only.

In our case we subtracted the ψ, ψ' tails using formula (4), the correction due to the continuum was estimated from (1) by the Monte Carlo (with the emission of photons according to (1) and assuming a slowly varying cross-section without resonances) and the correction due to the resonance itself was estimated from

$$\sigma'_{\text{OBSERVED}}(2E) = t\int_{\text{LOW END OF }\psi''}^E \frac{dK}{K}\left(\frac{K}{E}\right)^t \sigma'(2E-K) + \sigma'(2E) \quad (5)$$

where σ' refers to the resonance cross-section above the continuum. Equation (5) was solved by numerical iteration, where $\sigma'_{\text{OBSERVED}}$ was a parametrized form of the raw cross-section above the continuum

and after the subtraction of the ψ' and ψ tails, until the value of σ' stabilized. The ratio of $\frac{\sigma'}{\sigma'_{OBSERVED}}$ was used to correct $\sigma'_{OBSERVED}$.

The subtraction of the ψ tail was done by using the published values of A_o and mass, while the ψ' was done empirically. A two-parameter fit to (4) (free parameters A_o = magnitude of ψ' tail and the non-resonant part of R) in the $E_{c.m.}$ region from 3.692 to 3.730 GeV, allowed us to determine its size experimentally. To avoid energy callibration problems the mass of the ψ' was re-determined from a small set of runs, the resulting mass being $3684.4 \pm .2$ MeV in excellent agreement with the value measured with the same apparatus a year earlier (the error quoted here is only statistical and this should not be interpreted as a more accurate determination of ψ' mass).

At 3.77 GeV the relative size of these corrections are -5% for the part due to the continuum, -2% for the tail of the ψ, - 13% for the tail of the ψ', and + 9% for the ψ'' itself. The radiatively corrected values of R are shown in Fig. 23(b), and in Fig. 24 along with an additional measurement at 3.6 GeV and the result of previous measurements[59,60] in the same detector. Table II shows the values of R before and after radiative corrections.*

Since, as we shall see, the ψ'' peak is almost totally due to $D\bar{D}$ pair production we fit it with a Breit-Wigner shape so that

$$R = \frac{\sigma_T}{\sigma_{\mu\mu}} = \frac{3\pi}{\sigma_{\mu\mu} m^2} \frac{\Gamma_{ee}\,\Gamma(E)}{(E_{c.m.} - m)^2 + \Gamma^2(E)/4} \quad ,$$

where m is the mass of the resonance, Γ_{ee} is the partial width to electron pairs, and $\Gamma(E)$ is the total width whose energy dependence

*When these results were first published a correction to the external radiative corrections for e^+e^- collinear events that results in an 8% increase of the evaluated luminosity was not included. The results presented here include this correction, with the exception of Figs. 23 and 24.

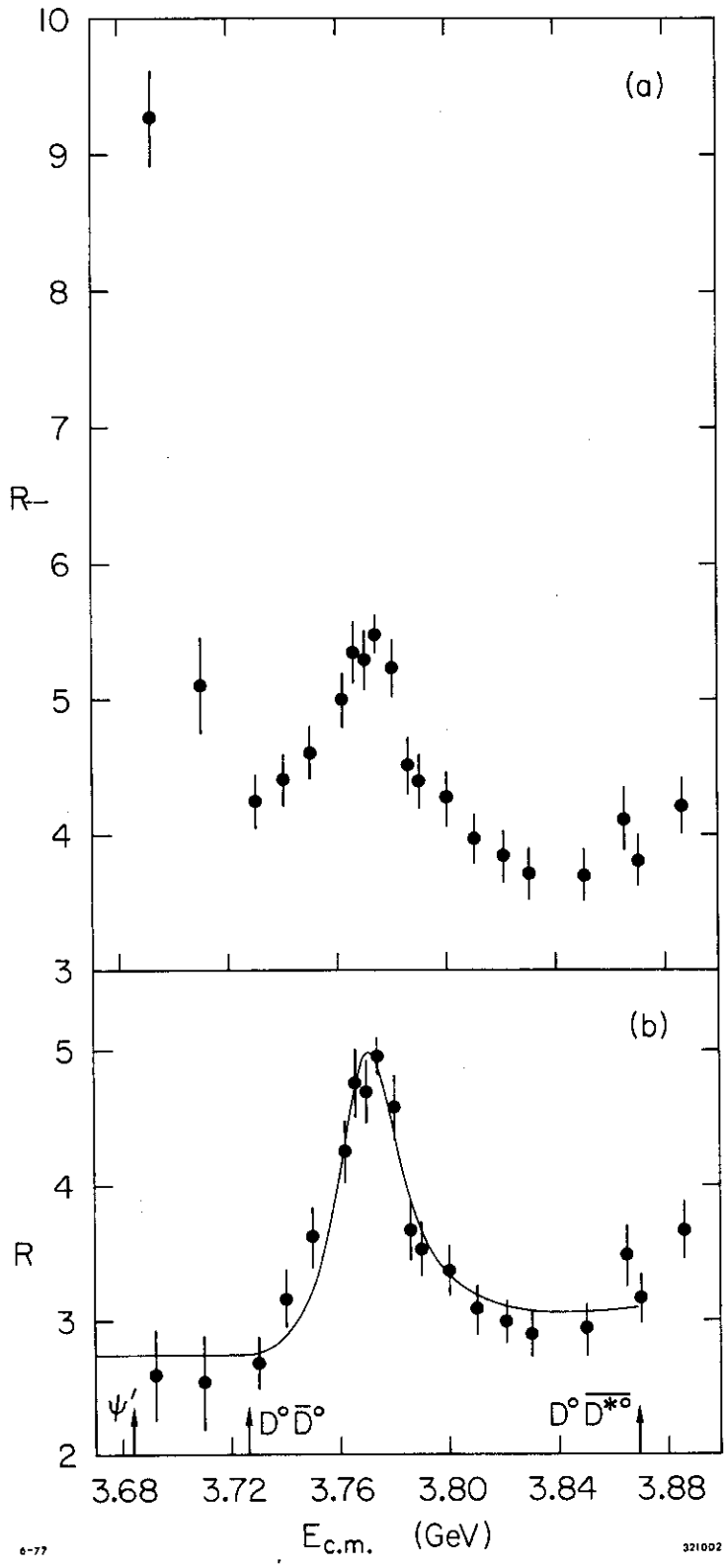

Figure 23 . R vs $E_{c.m.}$ (a) before and (b) after corrections for radiative effects. The curve is a p-wave Breit-Wigner shape described in the text. The mass of the ψ' and the positions of the thresholds for $D^\circ\bar{D}^\circ$ and $D^\circ\bar{D}^{*\circ}$ production are indicated.

TABLE II

R Values Near the $\psi''(3772)$ Before and After Radiative Corrections

$E_{c.m.}$	R before any corrections	R after all corrections
3.598	2.86 ± 0.17	2.46 ± 0.17
3.692	8.57 ± 0.34	2.40 ± 0.34
3.710	4.72 ± 0.35	2.35 ± 0.35
3.730	3.92 ± 0.19	2.48 ± 0.19
3.740	4.07 ± 0.19	2.94 ± 0.20
3.750	4.26 ± 0.19	3.34 ± 0.21
3.762	4.62 ± 0.20	3.92 ± 0.22
3.766	4.95 ± 0.22	4.40 ± 0.25
3.770	4.89 ± 0.21	4.34 ± 0.23
3.774	5.08 ± 0.12	4.59 ± 0.13
3.780	4.84 ± 0.21	4.23 ± 0.23
3.786	4.17 ± 0.20	3.40 ± 0.21
3.790	4.06 ± 0.19	3.27 ± 0.19
3.800	3.95 ± 0.18	3.12 ± 0.18
3.810	3.68 ± 0.17	2.85 ± 0.17
3.821	3.57 ± 0.17	2.77 ± 0.17
3.830	3.45 ± 0.17	2.68 ± 0.17
3.850	3.43 ± 0.18	2.72 ± 0.18
3.865	3.81 ± 0.22	3.21 ± 0.22
3.870	3.53 ± 0.18	2.93 ± 0.18
3.886	3.90 ± 0.20	3.39 ± 0.21

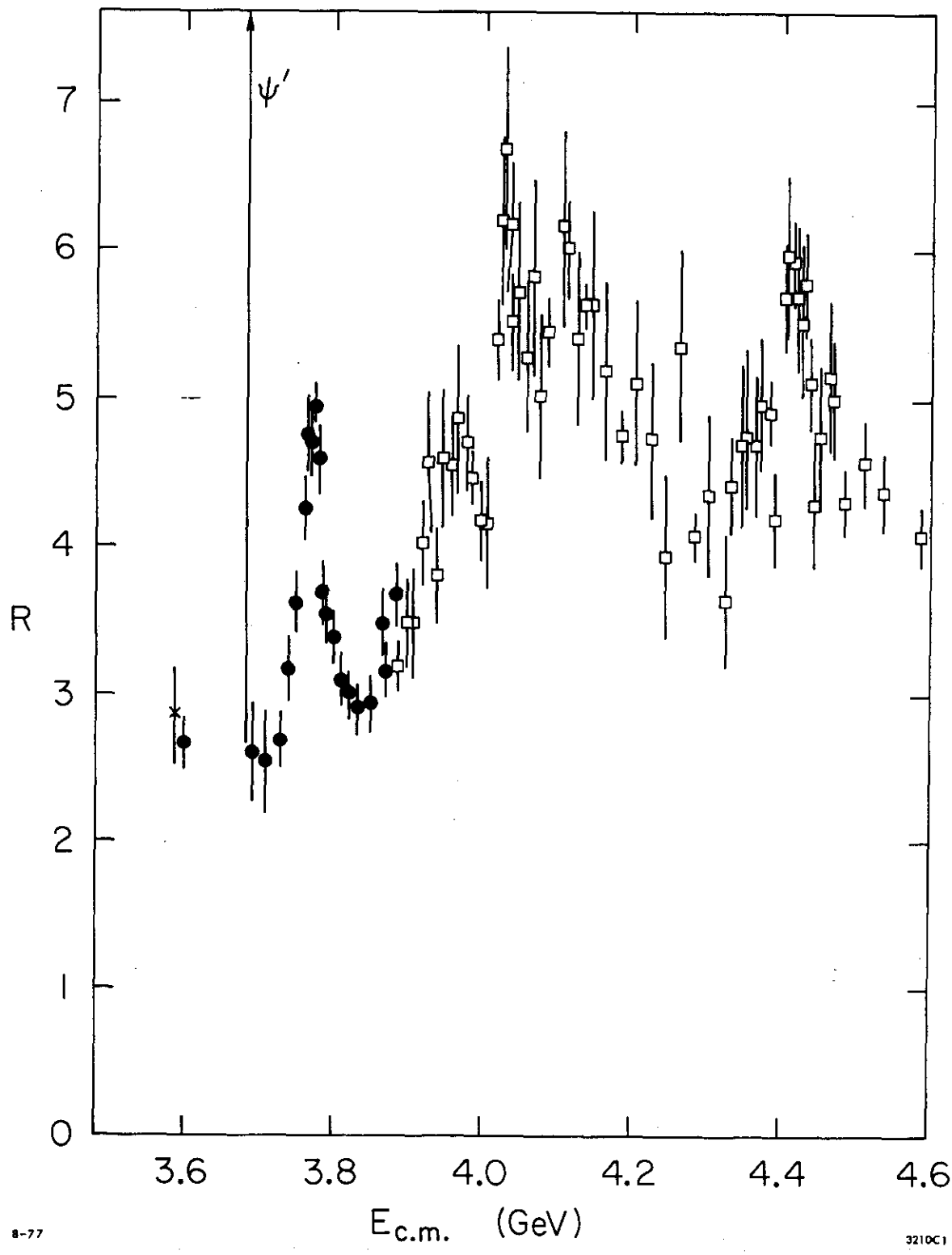

Figure 24 . Radiatively corrected values of R vs $E_{c.m.}$. The solid circles are from this work, open squares are from Ref. 59, and the crossed point is from Ref. 60. The '3.8 GeV' point from Ref. 60 with $R=3.28 \pm 0.28$ has been omitted because the exact energy at which it was taken is not known with sufficient accuracy to locate it properly on the high energy side of the $\psi''(3772)$.

is given by $$\Gamma(E) \propto \frac{p_o^3}{1 + (rp_o)^2} + \frac{p_+^3}{1 + (rp_+)^2}$$

Here p_o and p_+ represent the momenta of a D^o and a D^+, respectively, from D pair production; and r represents an interaction radius.[61] Although the data are fitted better with energy-independent widths, we can obtain acceptable fits for all values of r greater than 1 fm. A fit for r = 3 fm is shown in Fig. 23(b). The form of the background was found not to be critical, and for this fit it was arbitrarily taken to be a constant plus a constant times $(p_o^3 + p_+^3)$. The fit has a χ^2 of 14.3 for fifteen degrees of freedom. The parameters of the fit are given in Table III along with the previously determined[58,59,62] parameters of the other isolated ψ resonances.

Figure 25 shows the same data, in terms of cross-section, with the previously mentioned fit superposed (solid line) as well as a fit with an energy-independent width with the same background form (dotted line). This second fit had a χ^2 of 9.11 for 15 degrees of freedom and it gave a mass of 3771 MeV/c^2, a total width of 31 MeV/c^2, and a leptonic width 389 eV/c^2. The errors given in the Table III take into account the uncertainty in the form of the fitting function.

The parameters of the ψ'' are in striking agreement with those predicted by Eichten *et al.*[13] for the $^3D_1$ state of charmonium. In a calculation which was updated to include the measured D^o mass, Lane and Eichten[15] correctly predicted the mass and total width but underestimated the leptonic width by about a factor of 2.* In a non-

*We should note that the only other measurement of the leptonic width of the $\psi''(3772)$ differs significantly from our measurement. The DELCO experiment (Bacino *et al.*[53]) which ran simultaneously with our experiment at the east experimental pit of SPEAR found that: $m_{\psi''} = 3.770 \pm .006$ GeV/c^2, $\Gamma_{total} = 24 \pm 5$ MeV/c^2 and $\Gamma_{ee} = 180 \pm 60$ eV/c^2. A detailed comparison of the two results indicated that only 20% of the difference in Γ_{ee} between the two experiments can be attributed to relative normalization uncertainties. The remaining 80% arise from the fact that in our experiment ψ'' appears both as a wider and a larger bump. We can offer no explanation for this discrepancy.

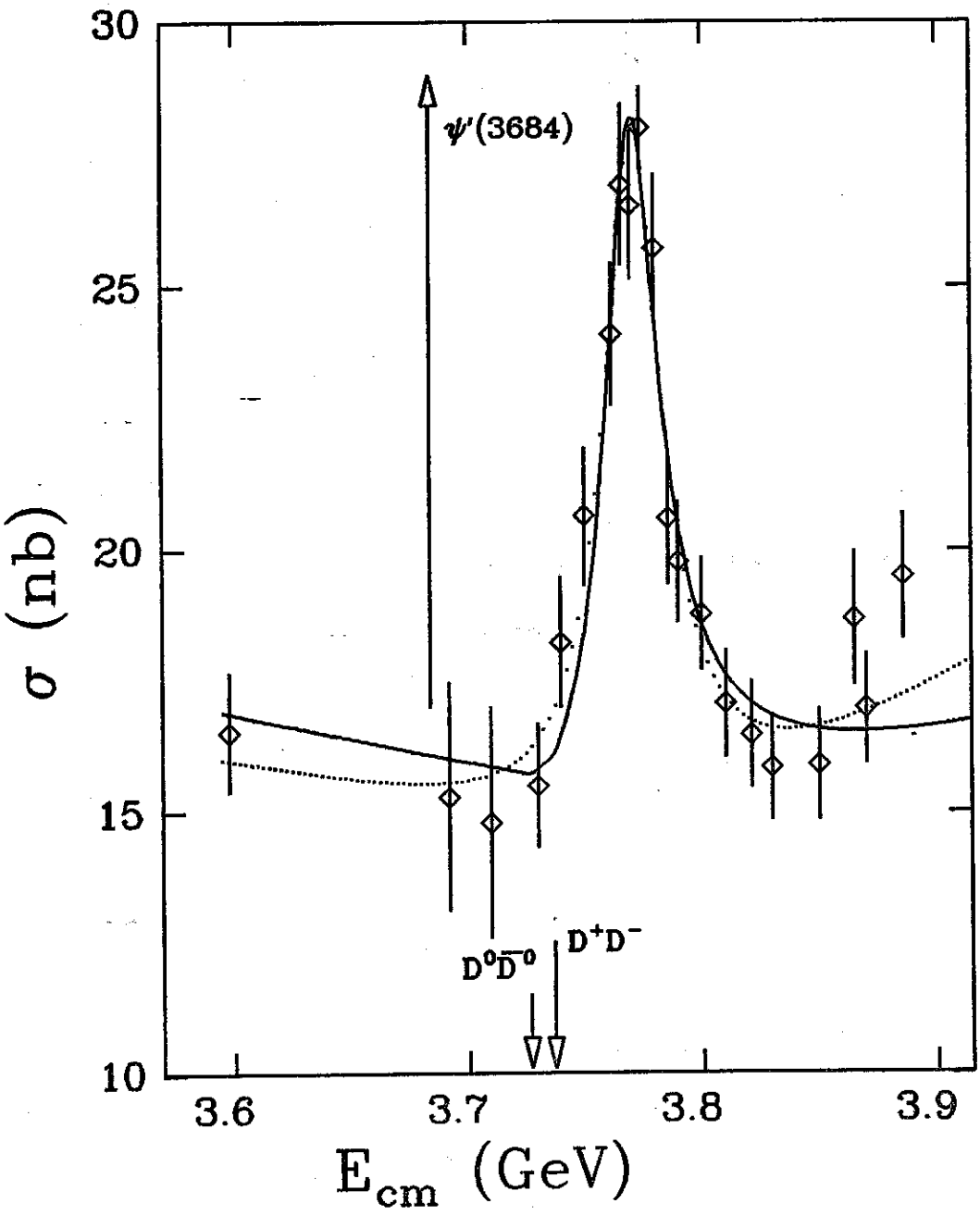

Figure 25 . Radiatively corrected values of σ_h vs $E_{c.m.}$. The solid curve is the p-wave Breit-Wigner shape, and the dotted curve is the Breit-Wigner shape with an energy independent width. Both shapes are described in the text. The mass of the ψ' and the thresholds for $D\bar{D}$ production are indicated.

TABLE III: Resonance parameters for the isolated ψ resonances. Γ is the full width, Γ_{ee} is the partial width to electron pairs, and B_{ee} is the branching fraction to electron pairs.

State	Mass* (GeV/c^2)	Γ (MeV/c^2)	Γ_{ee} (keV/c^2)	B_{ee}
$\psi(3095)$[a]	3.095 ± 0.004	0.069 ± 0.015	4.8 ± 0.6	0.069 ± 0.009
$\psi(3684)$[b]	3.684 ± 0.005	0.228 ± 0.056	2.1 ± 0.3	$(9.3 \pm 1.6) \times 10^{-3}$
$\psi''(3772)$	3.772 ± 0.006	28 ± 5**	0.34 ± 0.09	$(1.2 \pm 0.2) \times 10^{-5}$
$\psi(4414)$[c]	4.414 ± 0.007	33 ± 10	0.41 ± 0.14‡	$(1.2 \pm 0.3) \times 10^{-5}$

*Error includes a 0.13% uncertainty in the absolute energy calibration of SPEAR. The mass difference between the $\psi'(3684)$ and $\psi''(3772)$ is 88 ± 3 MeV/c^2.

[a]Ref. 58.

[b]Ref. 62

[c]Ref. 58, corrected for the 8% luminosity error mentioned in the text.

**Energy dependent width evaluated at the mass of the resonance.

‡Corrected for luminosity measurement error explained in the text.

relativistic approximation,[6] a D state does not couple to e^+e^-. It can obtain a leptonic width, however, by mixing with an S state. It is normally assumed that the $^3D_1$ mixes primarily with the 2^3S_1, which is identified with the ψ'.

In the simple two-state approximation[†] the mass matrix has the form

$$\begin{pmatrix} M_1 & \Delta \\ \Delta & M_2 \end{pmatrix}$$

M_1 is the "bare" mass of the $|2^3S_1\rangle$ state before mixing,

M_2 is the "bare" mass of $|1^3D_1\rangle$ state,

Δ is the mixing inducing term.

The physical states $|\psi'_S\rangle$ and $|\psi''_D\rangle$ with masses M_S and M_D are the eigenvalues of the mass matrix.

Introducing the mixing angle θ we have:

$$|\psi'_S\rangle = |\psi'(3684)\rangle = \cos\theta|2^3S_1\rangle - \sin\theta|1^3D_1\rangle \quad (6)$$

$$|\psi''_D\rangle = |\psi''(3772)\rangle = \sin\theta|2^3S_1\rangle + \cos\theta|1^3D_1\rangle .$$

We then have

$$\tan 2\theta = \frac{2\Delta}{M_2 - M_1}$$

[†]This approximation is an oversimplification. The partial width to electron-positron pairs of a mixed S-D state of charmonium is given by

$$\Gamma_e = \frac{16\pi e_c^2 \alpha_s^2}{M_n^2} \times \left| a\phi_s(0) + \frac{b}{M_n^2}\left[\frac{d^2\phi_D}{dr^2}\right]_{r=0} \right|^2$$

rather than our formula (7). Furthermore, relativistic corrections of the order $1/M_n^2$ have not been included. A discussion of these points can be found in Ref. 81.

$$M_D = 3772 \text{ MeV}/c^2 = (M_2 \cos^2\theta - M_1 \sin^2\theta)/\cos 2\theta$$

$$M_S = 3684 \text{ MeV}/c^2 = (M_1 \cos^2\theta - M_2 \sin^2\theta)/\cos 2\theta$$

or

$$M_2 = M_D \cos^2\theta + M_S \sin^2\theta$$

$$M_1 = M_D \sin^2\theta + M_S \cos^2\theta$$

Using the spatial wave function $\phi(\vec{r})$ of the $c\bar{c}$ system, we have for $\vec{r}_{c\bar{c}} = 0$, i.e. for zero quark separation:

$$\phi(0) = \langle \vec{r}_{c\bar{c}} = 0 | 1^3D_1 \rangle = 0$$

and from Eq. (6)

$$\phi_S(0) = \langle \vec{r} = 0 | \psi_S' \rangle = \cos\theta \langle \vec{r} = 0 | 2^3S_1 \rangle$$

$$\phi_D(0) = \langle \vec{r} = 0 | \psi_D'' \rangle = \sin\theta \langle \vec{r} = 0 | 2^3S_1 \rangle$$

Thus

$$\tan^2\theta = \frac{|\phi_D(0)|^2}{|\phi_S(0)|^2} \quad .$$

In the charmonium model, the partial width of a state ψ_n into electron-positron pairs is given by:[7,63]

$$\Gamma_e(\psi_n) = \frac{16\pi\, e_c^2\, \alpha_S^2}{M_n^2} |\phi_n(0)|^2 \qquad (7)$$

where $e_c = 2/3$ is the charge of the charmed quark

α_S is the coupling constant analogous to the QED α

M_n is the mass of the state.

Thus

$$\tan^2\theta = \frac{|\phi_D(0)|^2}{|\phi_S(0)|^2} = \frac{\Gamma_e(\psi_D'')}{\Gamma_e(\psi_S')} \left(\frac{M_D}{M_S}\right)^2 \quad .$$

Using the values in Table III we have:

$$\theta = 23.4 \pm 3^{o}$$

and

$$M_1 = 3698 \text{ MeV/c}^2 \quad , \quad M_2 = 3758 \text{ MeV/c}^2 \quad , \quad \Delta = 32.1 \text{ MeV/c}^2 \quad .$$

B. STUDY OF D MESONS PRODUCED IN THE DECAY OF THE $\psi''(3772)$

The ψ'' provides a rich source of kinematically well-defined and background free D-mesons. The D mass and some of the absolute branching ratios for D decays, can be derived with minimal assumptions from the study of this sample.[64]

The D mesons were detected as peaks in the invariant mass distributions of $K^{\mp}\pi^{\pm}$, $K^{\mp}\pi^{\mp}\pi^{+}\pi^{-}$, $K^{o}_{S}\pi^{+}\pi^{-}$ (for the D^{o}) and $K^{\mp}\pi^{\mp}\pi^{\pm}$, $K^{o}_{S}\pi^{\pm}$ (for the D^{+}). The technique used was the TOF weight technique described earlier, with unit weight assigned to a particular combination if the TOF weight exceeded a certain threshold: .01 for $K^{\mp}\pi^{\pm}$ combinations with the additional constraint that for a given doublet of particles only the combination with the higher weight was used, .3 for all other combinations.

The rationale behind this approach is that in the absence of significant background any weighted combinations in the D peak are most probably true D particles and misidentifications, given the small momentum of the D's and of their decay products, should give rise to low weight combinations. The higher weight threshold for multi-prong combinations was imposed in order to eliminate ambiguities between modes such as $K^{\mp}\pi^{\mp}\pi^{+}\pi^{-}$ and $K^{o}_{S}\pi^{+}\pi^{-}$.

Figure 26 shows the product of the cross-section $e^{+}e^{-} \to D^{o}$ or $\overline{D^{o}}$ + anything times the branching ratio for $D^{o} \to K^{-}\pi^{+}$ and $\overline{D^{o}} \to K^{+}\pi^{-}$ as a function of the center-of-mass energy. This value was determined by the number of $K^{\mp}\pi^{\pm}$ combinations under the D^{o} peak in the invariant mass distribution corrected for apparatus acceptance losses determined from the Monte Carlo simulation. The superposed line is the parametrization of the ψ'' line shape. Clearly the decay $\psi'' \to D^{o}\overline{D^{o}}$ is one of the decay modes of the ψ''.

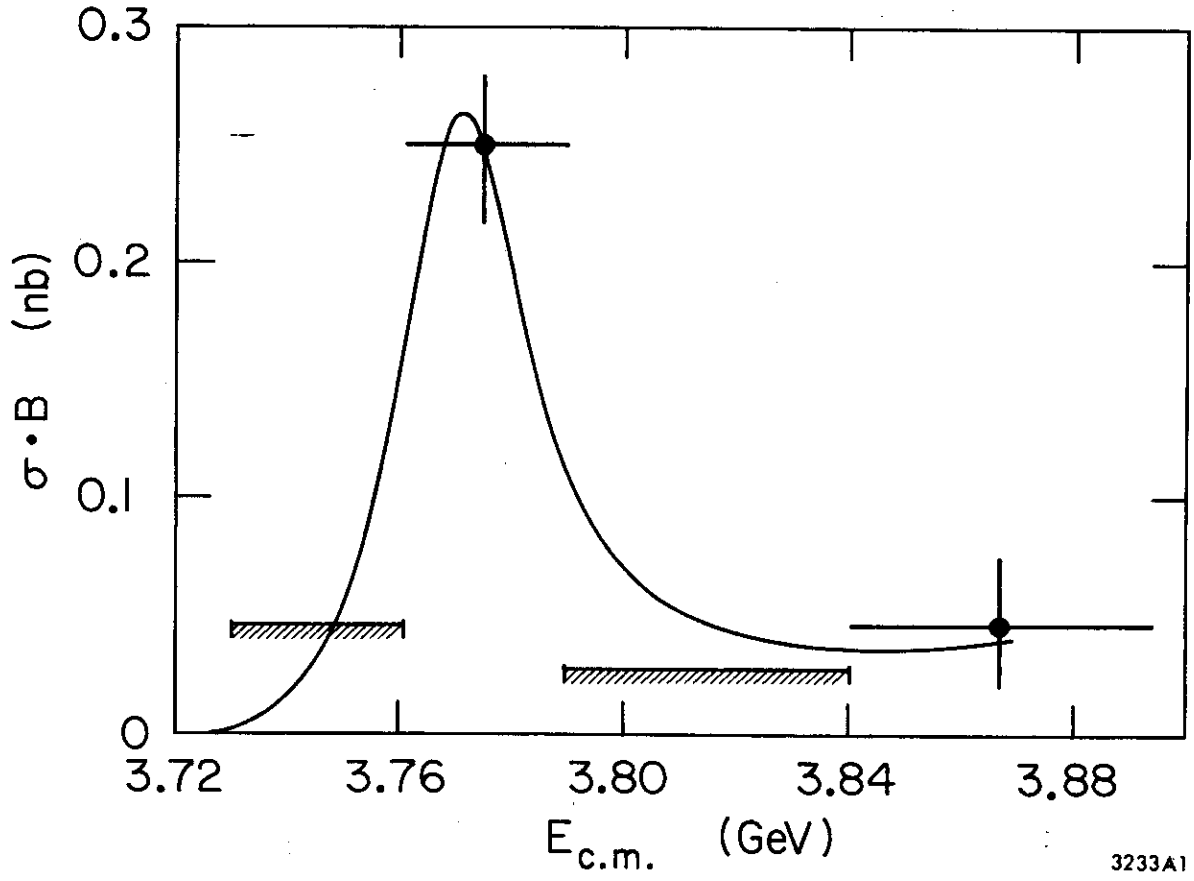

Figure 26 . $\sigma \cdot B$ for $D^0(\bar{D}^0) \rightarrow K^{\pm}\pi^{\mp}$ as a function of $E_{c.m.}$. The cross-hatched bars represent 90%-confidence-level upper limits. The curve represents the fit to the ψ'' line shape and charmed-particle background normalized to the $E_{c.m.} = 3.774$ GeV point.

For the remainder of this analysis we used the 24700 hadronic events with a center-of-mass energy near the peak of the ψ'' (73% at 3.774 GeV, 13% at 3.780 GeV, 8% at 3.766 GeV and 6% at 3.770 GeV), which correspond to an integrated luminosity of 1.21 pb^{-1}.

Rather than plotting the D meson candidates' invariant mass as determined by the measurement of the momenta of its decay products, we plot the mass obtained from

$$m_c = \sqrt{E_b^2 - P_D^2}$$

where $E_b = \frac{1}{2} E_{c.m.}$ and P_D is the vector sum of the momenta of the decay products of the D. Since E_b has a much smaller spread than the measured energy of a particle combination, and since the momentum of the D is small ($P_D \sim 300$ MeV/c), m_c is determined more accurately (by a factor of 5 to 10) in this manner than from the direct measurement. In order to make sure that a particle combination had an energy (determined from the momenta and masses of the decay products) consistent with E_b, we required that the combination's energy should be within 50 MeV of E_b, and then determined m_c.

The results shown in Fig. 27 show signals for the decays:

$$D^{\pm} \to K^{\mp}\pi^{\pm}\pi^{\pm} \quad , \quad K_S\pi^{\pm}$$

and

$$D^o \to K^-\pi^+ \quad , \quad K_S\pi^+\pi^- \quad , \quad K^-\pi^+\pi^+\pi^-$$

$$D^o \to K^+\pi^- \quad , \quad K_S\pi^+\pi^- \quad , \quad K^+\pi^-\pi^+\pi^- \quad .$$

The observed rms widths of the about 3 MeV/c^2 are consistent with our apparatus resolution alone.

The D masses were determined from fits to these distributions. The results were

$$m_{D^o} = 1.8633 \pm .0009 \text{ GeV/c}^2$$

$$m_{D^+} = 1.8683 \pm .0009 \text{ GeV/c}^2 \quad .$$

The reported uncertainties include contributions from the statistical

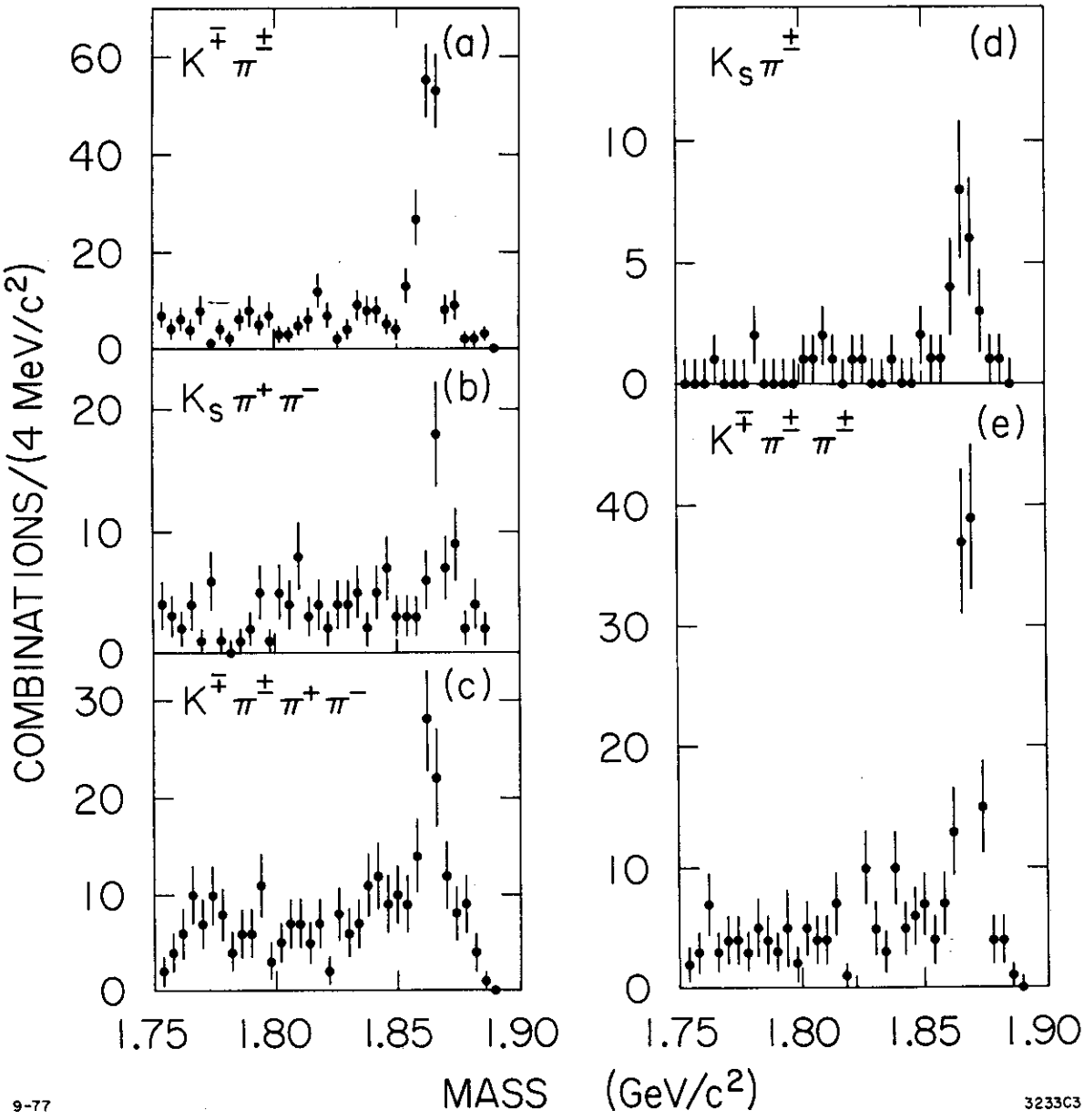

Figure 27 . Invariant-mass spectra for various D decay modes.

See the text for a discussion of cuts and techniques.

uncertainty ($\lesssim$ .4 MeV/c^2) and from systematic uncertainty ($\lesssim$ .8 MeV/c^2) which includes contributions from the uncertainty in the absolute momentum calibration ($\lesssim$ .5 MeV/c^2) and the uncertainty in the long-term stability of measuring E_b ($\lesssim$ .5 MeV/c^2).*

Table IV gives the D masses, together with the D^{*o} mass determined from previous measurements[42,65] and the D^{*+} mass determined[48] from the Q value of the decay $D^{*+} \to D^o$ mass. The deduced Q values and mass differences are also shown in Fig. 28.

Table V gives the values of $\sigma \cdot B$ for the five detected decay modes. The efficiencies quoted were determined from a Monte Carlo simulation with the same cuts imposed as the ones used in the real data analysis.

To obtain absolute branching fractions we need two quite reasonable assumptions: (1) that the ψ'' is a state of definite isospin, either 0 or 1, and (2) that its only substantial decay mode is $D\bar{D}$. The rationale for the latter assumption is that the ψ' and ψ'' differ in mass by only 88 MeV/c^2 and thus should have similar decay modes to channels which are open to both states. However, the total ψ'' width is two orders of magnitude larger than the ψ' width. The simplest explanation for the difference in widths is to attribute most of the ψ'' width to the $D\bar{D}$ channel, which is accessible to it, but not to the ψ'. The first assumption gives equal ψ'' partial widths to $D^o\bar{D}^o$ and D^+D^- except for factors which depend on the D momentum. The partial widths were assumed to be proportional to $p^3/(1 + (rp)^2)$ where p is the D momentum and r is an interaction radius. As r is varied from 0 to infinity, the fraction of $D^o\bar{D}^o$ changes from 0.59 to 0.53. We thus take this fraction to be 0.56 ± 0.03. The error due to the uncertainty in r is small compared to other systematic errors. Given these assumptions and the data on the total cross-section, the $D^o(\bar{D}^o)$ and D^- inclusive cross-sections for this data sample are 11.5 ± 2.5 nb and 9.1 ± 2.0 nb, respectively. The absolute branching fractions derived under these assumptions are also given in Table V.

In Table V we have accounted for $(9.4 \pm 2.3)\%$ of D^o decays and $(5.4 \pm 1.3)\%$ of D^+ decays. The unidentified decays are not detected by

*A .13% uncertainty in the absolute energy calibration of SPEAR has not been included. What we are really measuring is the ratio m_D/m_ψ, with m_ψ taken as 3095 MeV/c^2.

TABLE IV

Masses, mass differences, and Q values for the D meson system. The quantities in parentheses are taken from Refs. 48 and 64 and are used in the calculation of quantities involving D^*'s. All units are MeV/c^2. The errors quoted include explicitly the calculation of correlated errors, e.g. the mass difference D^+-D^o is more precisely known because most of the systematic errors cancel in the mass difference.

MASS (MeV/c^2)		MASS DIFFERENCE (MeV/c^2)		Q VALUES (MeV/c^2)	
D^o	1863.3±0.9	D^+-D^o	5.0±0.8	$D^{*o}\to D^o\pi^0$	7.7±1.7
D^+	1868.3±0.9	$D^{*+}-D^{o*}$	2.6±1.8	$D^{*o}\to D^+\pi^-$	-1.9±1.7
D^{*o}	(2006.0±1.5)	$(D^+-D^o)-(D^{*+}-D^{*o})$	2.4±2.4	$D^{*+}\to D^o\pi^+$	(5.7±0.5)
D^{*+}	2008.6±1.0			$D^{*+}\to D^+\pi^0$	5.3±0.9

TABLE V

Number of combinations, efficiency, cross section times branching fractions ($\sigma\cdot B$) and branching fractions for various D decay modes. The absolute branching fraction determination depends on assumptions discussed in the text.

MODE	# COMB.	EFFICIENCY	$\sigma\cdot B$(nb)	B(%)
$K^+\pi^-$ + c.c.	130±13	.42	0.25±0.05	2.2±0.6
$K^o\pi^+\pi^-$ + c.c.	28± 7	.05	0.46±0.12	4.0±1.3
$K^-\pi^+\pi^+\pi^-$ + c.c.	44±10	.10	0.36±0.10	3.2±1.1
$\bar{K}^o\pi^+$ + c.c.	17± 5	.10	0.14±0.05	1.5±0.6
$K^-\pi^+\pi^+$ + c.c.	85±11	.19	0.36±0.06	3.9±1.0

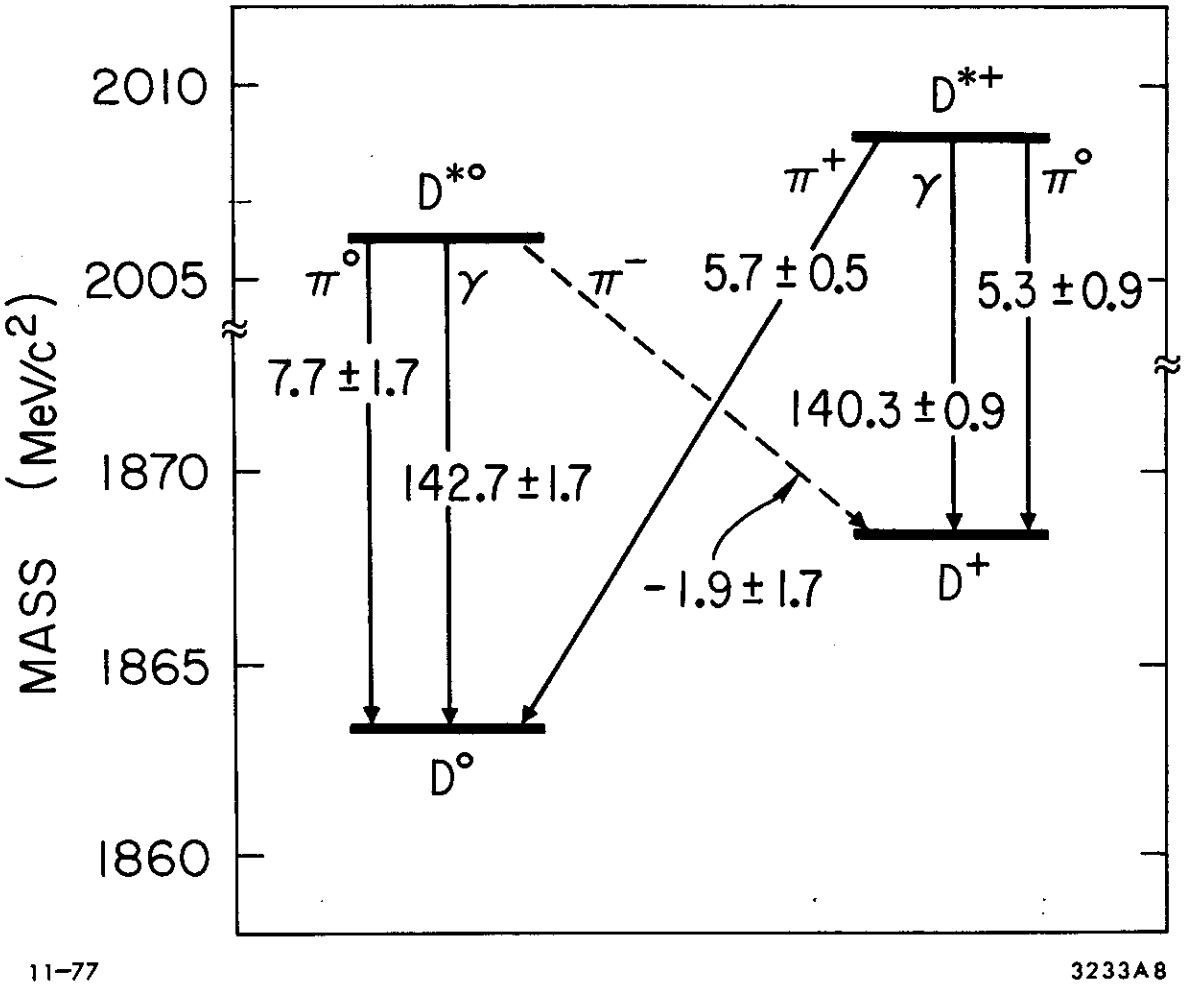

Figure 28 . Mass level diagram for D^* and D^0 states from the measurements shown in Table IV. The arrows represent different decay modes of the D^*; the numbers across the lines represent the Q for each decay expressed in MeV. The decay $D^{*0} \rightarrow D^+\pi^-$ cannot take place.

the techniques discussed up to now either because they contain neutral particles, have too small a branching fraction, have too small a detection efficiency, or are obscured by backgrounds.

The angular distribution of D's relative to the incident beams must be of the form

$$P(\theta) \propto 1 + \alpha \cos^2\theta, \qquad |\alpha| \leq 1 \quad ,$$

for any D spin and α must be -1 for spin 0. Figure 29 shows the angular distribution for D's for the $D^+ \to K^-\pi^+\pi^+$ and $D^o \to K^-\pi^+$ decays. The values of α are found to be -1.04 ± 0.10 and -1.00 ± 0.09, respectively, consistent with the assignment[42,66] of spin 0 for the D mesons.

In the events with a $D^o(D^+)$ observed in an e^+e^- annihilation at the $\psi''(3772)$, since the ψ'' decays into $D\bar{D}$ exclusively, the remaining particles must be the decay products of a $D^o(D^o)$. These "tagged" events permit inclusive studies of the decays of D mesons. A summary of the result of such studies follows.

The charged multiplicity in the decay of the recoiling D in these tagged events can be obtained by counting the number of additional tracks in each event. The true charged multiplicity in D decays can be obtained from the observed multiplicity distributions through an unfolding procedure patterned after a Monte Carlo simulation of DD^o and D^+D^- production at the ψ''.

The results are[67]

$$\langle n_c \rangle_{D^o} = \langle n_c \rangle_{D^+} = 2.3 \pm 0.3 \quad .$$

The D^o's decay mostly into two charged particles while the D^+'s decay roughly equally into states with one or three charged particles. It should be noted that in this multiplicity analysis K_S^o's were not identified and the charged pions from K_S^o decay are included in the quoted values.

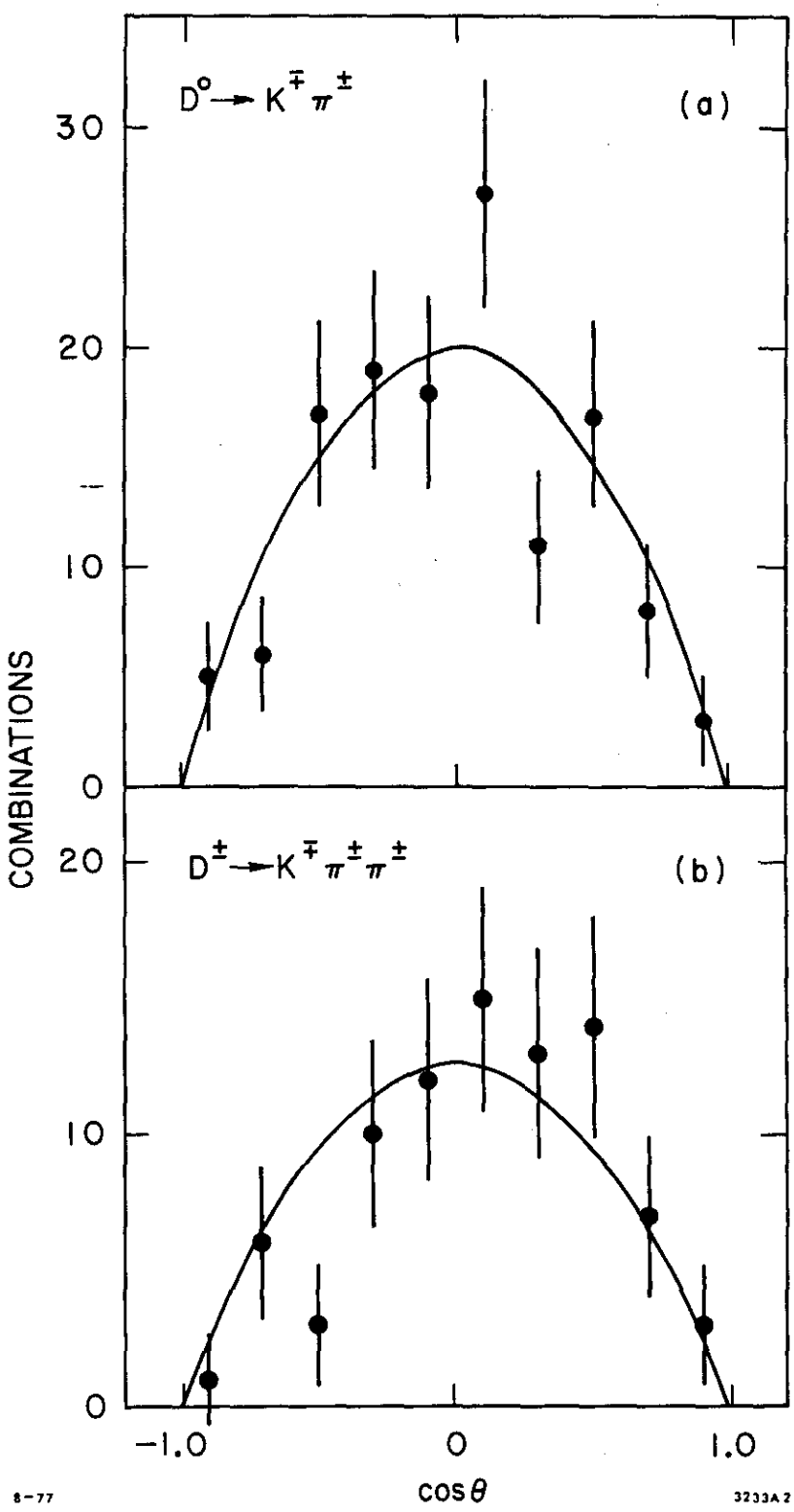

Figure 29 . Cosine of the angle between the incident e^+ beam and the D momentum for (a) $D^0(\overline{D^0}) \to K^{\mp}\pi^{\pm}$ and (b) $D^{\pm} \to K^{\mp}\pi^{\pm}\pi^{\pm}$, after background subtraction. The curves represent $\sin^2\theta$, the required distribution for the production of spinless D mesons.

From the study of the tagged events inclusive decay branching ratios can also be obtained. The results are:[67]

DECAY	BRANCHING RATIO
$D^o \to K^{\pm} X$	$35 \pm 10\%$
$\to K^o X$	$57 \pm 26\%$
$D^+ \to K^- X$	$10 \pm 7\%$
$\to K^+ X$	$6 \pm 6\%$
$\to K^o X$	$39 \pm 29\%$

where X stands for any other allowed particles in the decay.

Interesting results on D decays at the ψ'' using the γ-ray detection and electron identification capabilities of the Lead-Glass Wall system have also been obtained. We simple list them here:

a) The branching ratio for the decay of D mesons into an electron plus additional particles, averaged over the neutral and charged D, has been measured [68] to be $7.2 \pm 2.8\%$.

b) The decay $D^o \to K^- \pi^+ \pi^o$, with π^o identified from two γ-rays detected in the Lead-Glass Wall, has been observed.[69] The branching ratio for $D^o \to K^- \pi^+ \pi^o$ is $12 \pm 6\%$.

In summary, the study of D mesons produced at the $\psi''(3772)$ allowed for an accurate determination of their mass, their decay multiplicity, the measurement of absolute branching ratios into some exclusive states, as well as into inclusive states with kaons and electrons, and a confirmation that the spin of the D mesons is 0.

CHAPTER 4

INCLUSIVE PRODUCTION OF D AND K MESONS IN THE C.M. ENERGY RANGE 3.6 TO 5.8 GeV

We started the previous chapter with the observation that the most remarkable feature of R, with the exception of the ψ and ψ', was the ψ'' at 3.772 GeV. This chapter continues from that point on with the examination of the next most striking feature of R: the rich structure[59] of R at 4.0 - 4.4 GeV and its overall step-like increase[1,52] from 2.6 at 3.6 GeV to 5.2 at 7.0 GeV.

Even though there is considerable disagreement and confusion as to the exact number of resonances in region 4.0 to 4.4 GeV, the results of all the relevant experiments, shown in Fig. 3, show the existence of two clear resonances at 4.03 and 4.4 GeV and possibly of a third one at 4.16 GeV. Above this resonance region, R reaches again a smooth plateau 2.6 units higher than its original value at 3.6 GeV. The reason for this truly remarkable behavior is two-fold: one unit of the increase in R is due to the onset of pair production of the heavy lepton τ and the remaining 1.6 units of R are presumably due to the production of charmed particles. D mesons, the lowest lying charmed states, are expected to constitute the largest fraction of these charmed particles. It is an interesting question to ask whether the D production indeed follows the shape of R and what part of the observed structure can be explained by it.

In order to ellucidate this point we have studied[70] the inclusive production of D mesons as a function of energy for the c.m. energy range 3.6 to 5.8 GeV. A closely related quantity to the inclusive D meson production is the rate for inclusive kaon production. Since D mesons decay predominantly into final states that include kaons, an enhanced production of D's should give rise to an increased production of strange mesons. For this reason the scope of our analysis was enlarged to include the production of K's.

The data used for this study are hadronic events with three or more charged tracks detected in the final state. This sample was collected during the second part of the experiment and the energy range covered extends from 3.6 to 5.8 GeV. The total luminosity is approximately 8 pb^{-1}.

The D mesons were identified as peaks in the invariant mass distribution of $K^-\pi^+$ and $K^+\pi^-\pi^+$ combinations. We chose these two decay modes of the D^o and D^+ because they have the highest acceptance in our apparatus and the highest signal-to-background ratio. Particle identification was achieved through the TOF weight technique, which has been described in nauseating detail in Chapter 2. Instead of using fractional "weighted" combinations, we assigned a weight of 1 to the particular particle hypotheses that gave the highest TOF-derived weight for every two or three particle combination. We also required that the recoiling mass against the D be greater than 1.8 GeV/c^2. This selection criterion was introduced in order to reduce the background due to to uncorrelated combinations and proved to be effective at the lower c.m. energies under study. As the c.m. energy increases the uncorrelated combination background (i.e. the $K\pi$ or $K\pi\pi$ phase space) extends towards higher invariant masses and the D peak is no longer on the tail of this distribution. For this reason the 1.8 GeV/c^2 cut does not reduce significantly the background at high energies.

The number of D's was obtained from fits to the $K\pi$ and $K\pi\pi$ invariant mass distributions. These distributions, together with the fits, are shown in Fig. 30. The theoretical shape used in the fit was the sum of a smooth background and a gaussian of fixed mass and width. The width we used was the estimated width from the Monte Carlo simulation (see Fig. 13). The masses we used were not the true masses of the D's but approximately 7 MeV/c^2 higher. This shift of the centroid of the D peaks, which we attribute to an unexplained systematic shift of our invariant mass calculation, appears consistently in all of the observations of D's in our apparatus.

The detection efficiency for D's was estimated from Monte Carlo studies as an overall correction factor. At each energy we used a production mechanism which best reproduced the observed D meson momentum distribution. At 4.16 and 4.3 GeV we used a production model of $D^*\bar{D}^*$; for higher energies we used a mixture of $D\bar{D}\pi\pi$ and $D^*\bar{D}^*\pi$.

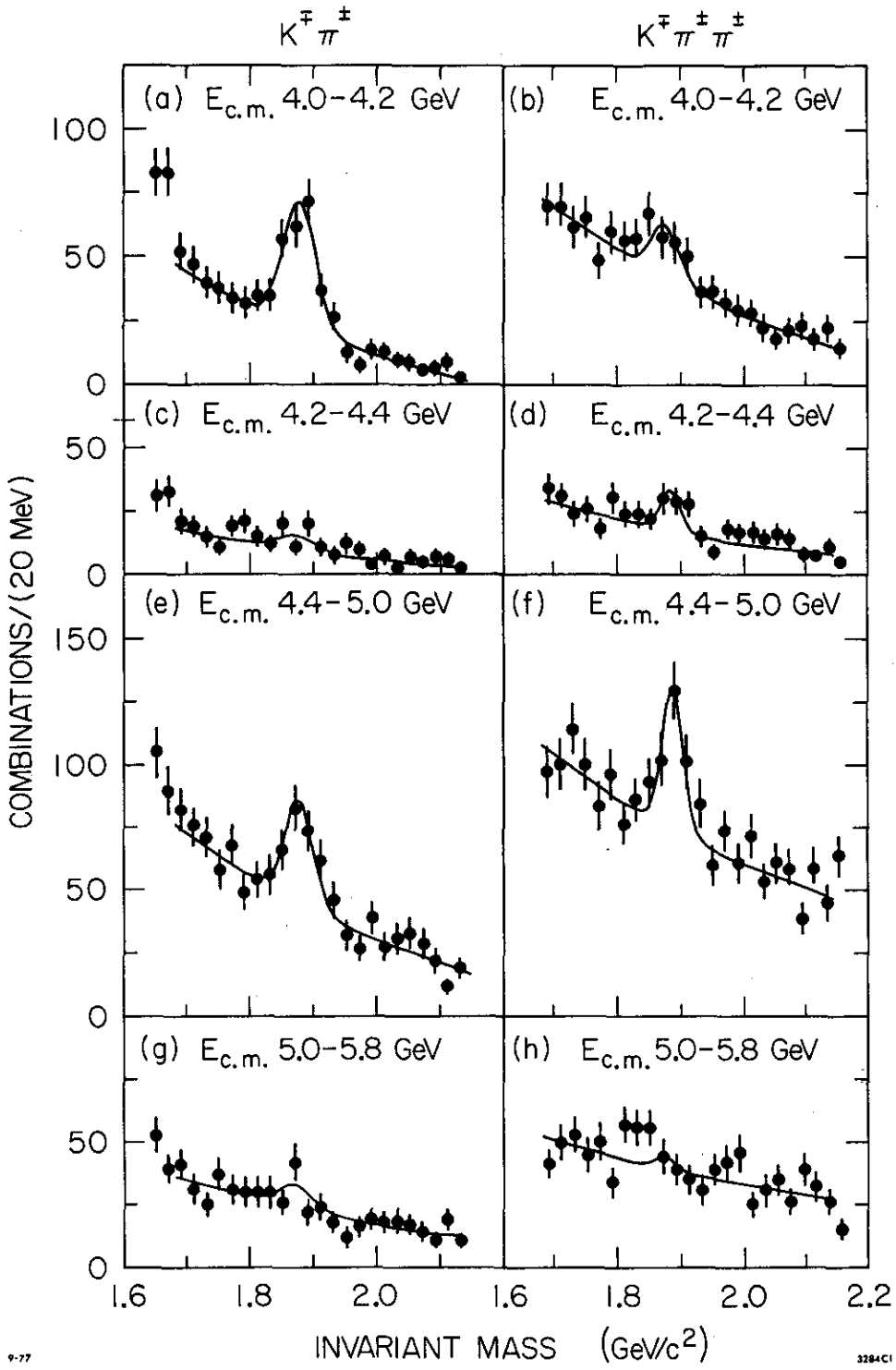

Figure 30 . Invariant mass spectra of weighted $K^{\pm}\pi^{\mp}$ and $K^{\mp}\pi^{\pm}\pi^{\pm}$ for several $E_{c.m.}$ ranges. The fits are explained in the text.

For the charged kaons we used the technique described on page 44. As we noted earlier, the sensitivity of this method deteriorates rapidly for kaon momenta greater than 1 GeV/c, forcing us to use an extrapolation in order to infer the fraction of $K^{\pm}$ at high momenta. This correction, which is of the order of 10% at the c.m. energy of 4 GeV, increases as the c.m. energy and the average kaon momenta increase and becomes a major part of our results for c.m. energies above 4.4 GeV. For this reason we do not report a measurement for inclusive charged K production at that energy or at higher energies. Neutral kaons were detected by their decay $K^o_s \to \pi^+\pi^+$, using the techniques described in Chapter 2.

The detection efficiency for kaons was estimated as the product of two terms, a term giving the probability of detecting a single kaon of a certain momentum and a term giving the probability for an event with a detected kaon to trigger our apparatus. In the determination of the trigger efficiency we investigated the effect of introducing angular distributions due to jet formation versus isotropic particle production. The differences between the two approaches were negligible, a reflection of the fact that the c.m. energy is relatively low and jet formation is not very pronounced.

The results of these studies are shown in Tables VI and VII. Table VI shows the number of observed D's and the luminosity for every energy interval. Our efficiency estimate, together with the branching ratios for $D^o \to K^-\pi^+$ and $D^- \to K^+\pi^-\pi^-$ decays allow us to determine the cross-section for inclusive D meson production. These cross-sections, as well as the ratio $R_D = (\sigma_{D^o} + \overline{D^o} + \sigma_{D^+} + D^-)/2\sigma_{\mu\mu}$ are shown in Table VI. For completeness, the ψ'' results from the previous chapter as well as the inclusive production of D's at 7 GeV, which will be discussed in chapter 5, and at 4.028 and 4.414 GeV, from earlier work[71], are included.

We observe a clear D signal in the intervals 4.0 - 4.2 GeV, and 4.4 - 5.0 GeV; no significant signal is observed in the region 4.2 - 4.4 GeV, a region where R also shows a dip.[13] In the region 5.0 - 5.8 GeV, even though no significant D signal is observed, our efficiency is quite small and our results not inconsistent with a sizable D meson production. The quantity R_D, shown in Fig.31a, follows the overall shape of R. Within our errors, R_D together with the contribution due

TABLE VI : Energy, mean energy, integrated luminosity, observed number of D's, cross section for D^o and D^+ inclusive production, and R_D for several center-of-mass energy intervals.

c.m. energy (GeV)	Mean c.m. energy (GeV)	Integrated luminosity (nb^{-1})	Observed Number of D^o and $\bar{D}^o$	Observed Number of D^+ and D^-	$\sigma_{D^o+\bar{D}^o}$ (nb)	$\sigma_{D^++D^-}$ (nb)	R_D ‡
3.73 - 3.76	3.74	180	<2.8 †	<2.7 †	<1.7 †	<1.9 †	<0.29 †
3.76 - 3.79	3.775	1220	130 ± 13	85 ± 11	11.5 ± 2.5	9.1 ± 2.0	1.69 ± .27
3.79 - 3.84	3.81	238	<1.4 †	<1.4 †	<0.7 †	<0.8 †	<0.13 †
3.84 - 3.89	3.87	236	5 ± 3	2 ± 2	2.1 ± 1.4	1.1 ± 1.1	.28 ± .16
4.0 - 4.2 §	4.15	1680	153 ± 20	65 ± 21	16.5 ± 5.0	6.2 ± 2.5	2.33 ± .57
4.2 - 4.4	4.28	854	15 ± 9	30 ± 12	3.5 ± 2.1	6.0 ± 2.9	1.03 ± .40
4.4 - 5.0 ¶	4.68	2376	108 ± 28	117 ± 30	10.9 ± 3.8	10.1 ± 3.5	2.64 ± .65
5.0 - 5.8	5.36	1115	26 ± 19	11 ± 11	5.6 ± 4.4	2.0 ± 2.0	1.26 ± .83
4.028*	4.028	1365	182 ± 18	82 ± 14	24.2 ± 7.0	9.6 ± 2.9	3.16 ± .73
4.414*	4.414	1752	92 ± 18	67 ± 19	12.6 ± 4.2	7.8 ± 3.0	2.29 ± .60
6.0 - 7.8 ††	6.96	22.5×10^3	173 ± 31	90 ± 31	3.2 ± 0.9	1.7 ± 0.7	1.34 ± .33

‡ $R_D = \dfrac{\sigma_{D^o + \bar{D}^o} + \sigma_{D^+ + D^-}}{2\sigma_{\mu^+\mu^-}}$

† 90% confidence level

§ 50% of this data was taken at 4.16 GeV

¶ Less than 10% of this data was taken in the vicinity of the $\psi(4.4)$ resonance

* From Ref. 71.

†† From Ref. 75 and chapter 5 .

TABLE VII : Energy, mean energy, integrated luminosity, observed number of kaons, and cross section for inclusive kaon production for several center-of-mass energy intervals.

c.m. energy (GeV)	Mean c.m. energy (GeV)	Integrated luminosity (nb^{-1})	Number of observed K^o_s	Number of observed † K^+ and K^-	$\sigma_{K^o_s}$ (nb)	$\sigma_{K^+} + \sigma_{K^-}$ (nb)
3.6	3.600	48	17 ± 8	130 ± 32	3.3 ± 1.5	6.3 ± 1.5
3.73 - 3.76	3.743	215	118 ± 19	916 ± 136	4.7 ± 0.8	10.6 ± 1.6
3.76 - 3.79	3.775	1263	1138 ± 58	8082 ± 526	7.7 ± 0.4	15.6 ± 1.0
3.79 - 3.84	3.811	341	123 ± 20	1522 ± 265	3.1 ± 0.5	10.4 ± 1.8
3.84 - 3.90	3.869	258	128 ± 19	976 ± 156	4.2 ± 0.6	8.6 ± 1.3
3.90 - 4.00	3.956	188	126 ± 18	896 ± 160	5.6 ± 0.8	10.8 ± 1.9
4.00 - 4.10	4.040	383	360 ± 29	3102 ± 292	7.8 ± 0.6	18.0 ± 1.7
4.10 - 4.20	4.152	1297	1234 ± 58	9006 ± 566	7.8 ± 0.4	15.1 ± 1.0
4.20 - 4.40	4.286	854	606 ± 40	3561 ± 242	5.5 ± 0.3	9.2 ± 0.6
4.40 - 4.80	4.619	1830	1181 ± 59	-*	5.0 ± 0.2	-*
4.80 - 5.20	4.948	856	487 ± 38	-*	4.3 ± 0.3	-*
5.20 - 5.60	5.394	667	321 ± 33	-*	3.6 ± 0.4	-*

† Number of events corrected for TOF losses.

* Above 4.4 GeV the high momentum of the $K^{\pm}$ makes identification unreliable.

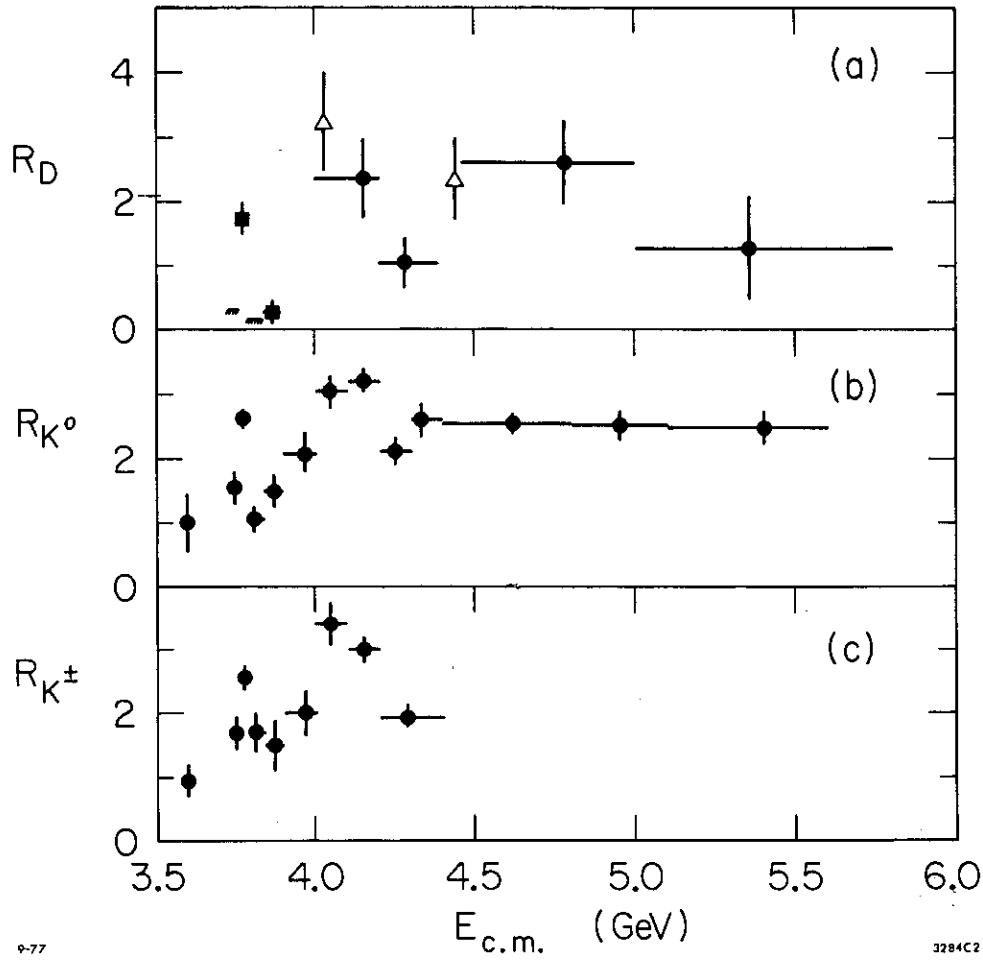

Figure 31 . Plots of :

(a) the ratio $R_D = (\sigma_{D^o\bar{D}^o} + \sigma_{D^+D^-})/2\sigma_{\mu^+\mu^-}$

(b) the ratio $R_{K^o} = 2\sigma_{K^o_s} / \sigma_{\mu^+\mu^-}$

(c) the ratio $R_{K^\pm} = (\sigma_{K^+} + \sigma_{K^-})/ \sigma_{\mu^+\mu^-}$

as functions of $E_{c.m.}$. The triangles are from Ref. 70 and the squares from Ref. 63.

to pair production of the heavy lepton τ can account for all of the increase in R observed[1] for c.m. energies greater than 4.0 GeV.

Figure 32 illustrates this point further. The upper curve is an eyeball fit to the R values as measured in our detector (see Fig. 2). The various contributions to R are progressively added starting from R = 0.

1) R_{OLD}, a constant value inferred from the measurement below the charm threshold. This constant value of 2.5 units of R represents the contribution of the old non-charmed quarks u, d, and s.
2) The contribution due to $\tau^+\tau^-$ production. We have used the QED calculated value $R_{\tau^+\tau^-} = \beta(3 - \beta^2)/2$, where β is the velocity of the τ.
3) $R_{B\bar{B}}$, the charmed baryon contribution as inferred from earlier measurements of inclusive antiproton production (see Fig. 7). The single antiproton inclusive cross-section rises from $R_{p+\bar{p}} = .3$ to $R_{p+\bar{p}} = .6$ as the c.m. energy varies from 4.4 to 5 GeV. Above 5 GeV $R_{p+\bar{p}}$ is approximately constant. We have taken the value of $R_{B\bar{B}}$ to be .3 at high energies to account for $n\bar{n}$ production, which we assume to be equal to $p\bar{p}$ production.
4) We finally include the $R_{D\bar{D}}$ values of Table VI to the above as points with error bars.

As we see the sum of these four contributions seems to account for the totality of R. It must be noted that the uncertainty in $R_{D\bar{D}}$ and and $R_{B\bar{B}}$ are large enough so that $\sim$½ unit of R for production of the putative[16] F or for some other process can be

Figures 31(b) and 31(c) are plots of the quantities $R_{K^\pm} = (\sigma_{K^+} + \sigma_{K^-})/\sigma_{\mu^+\mu^-}$ and $R_{K^o} = 2\sigma_{K^o}/\sigma_{\mu^+\mu^-}$, where the factor of 2 in R_{K^o} accounts for the undetected K^o_L's. These quantities, $R_{K^\pm}$ and R_{K^o}, represent the contribution to R for events containing a kaon pair and should be equal if charged and neutral kaons are produced at the same rate. Within our experimental errors this behavior is verified; furthermore, $R_{K^\pm}$ and R_{K^o} show an energy dependence similar to the energy dependence of R_D, as expected from the production and subsequent decay of charmed mesons.[72]

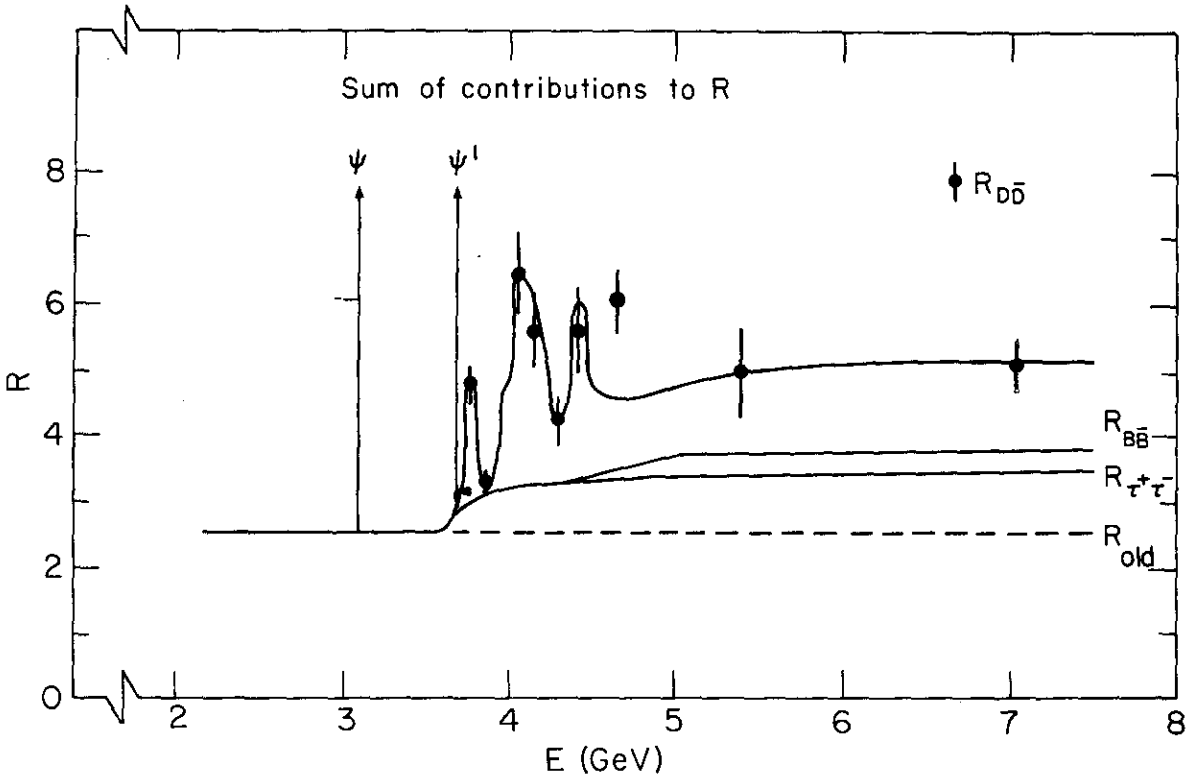

Figure 32. A composite graph illustrating the various contributions to R, the total hadronic cross section over $\sigma_{\mu\mu}$. The top curve is a sketch of R, hand drawn over the data of Fig. 2. The following contributions are progressively added starting from R=0: R_{old} is a constant as inferred by the data points below charm threshold; $R_{\tau^+\tau^-}$ is the heavy lepton contribution as calculated from QED; $R_{B\bar{B}}$ is the charmed baryon contribution as inferred by the data of Fig. 7. Finally we add the contribution of $R_{D\bar{D}}$ as data points, taken from Fig. 31 and Table VI.

A direct and significant by-product of this analysis is that the combination of the inclusive kaon and D meson production allows us to determine the number of kaons per D decay, if we make the (reasonable) assumption that the ψ'' decays entirely into $D\bar{D}$ pairs. From the total hadronic cross-section measurements of the previous chapter we see that for the c.m. energy region 3.75 to 3.79 GeV one third of the total cross-section is due to the ψ'' and two thirds due to the non-resonant background, while for the regions 3.73-3.76 GeV and 3.79-3.84 GeV the contribution of the ψ'' to the total cross-section is only 10%. Using this information we find that there are 1.03 ± 0.27 neutral kaons and 0.83 ± 0.24 charged kaons per ψ'' event. These imply that we have 0.52 ± 0.14 neutral kaons and 0.42 ± 0.12 charged kaons per D decay. For the non-resonant part of the cross-section, we find that there are 0.26 ± 0.08 neutral kaons and 0.32 ± 0.10 charged kaons per event.

The last result should be compared with the results obtained from the study of the D decays using the "tagged events."[67] On the assumption that the $D^o:D^+$ production ratio at the ψ'' is 56:44, the values of the branching ratios for D decays into final states containing kaons determined from the tagged events imply 0.49 ± 0.19 neutral kaons and 0.27 ± 0.07 charged kaons per D decay. We can find no reason why the number of charged kaons per D decay differ by this amount. A reasonable explanation is that the value obtained from the "tagged" event study is a statistical fluctuation (the total sample consisted of 248 events only), but recent unpublished data[73] on "tagged" D events in the MARK II detector at SPEAR give results consistent with our "tagged" event analysis.

CHAPTER 5

INCLUSIVE PRODUCTION OF D MESONS AT 7 GeV

As mentioned in the last part of Chapter 1, the dynamical mechanism for fragmentation of heavy quarks into hadrons is a subject of considerable interest, not only in its own right, but also because of its use in predicting the energy spectrum of leptons from the decay of charmed particles produced in hadronic or neutrino experiments. Many authors[22,24-27,29-30,33-36] have proposed a variety of forms for the quark fragmentation function for the charmed $\bar{q}$uark and have analyzed the recently available data on di-lepton[32,33] and D meson[74] production by neutrinos trying to obtain some information on its shape. The production of D mesons in e^+e^- annihilation provides a particularly clean way for studying the charmed quark fragmentation function. Specifically, the shape of the differential cross-section $\frac{d\sigma}{dz}$ for inclusive D meson production (where $z = 2E_D/\sqrt{s}$) can be directly related to the fragmentation function. The only drawback of the study of $\frac{d\sigma}{dz}$ in e^+e^- annihilation is that the maximum available energy, i.e. E_{beam}, is comparable to the mass of the charmed quark ($\simeq \frac{1}{2}m_\psi = 1.5$ GeV/c^2) and z may not be the appropriate scaling variable. For this reason we studied[75] the energy/momentum spectrum of D's only at the highest energies available to us, in order to obtain a glimpse of the charm fragmentation function in a region that probably approaches the asymptotic regime and is not dominated by threshold effects.

The data used in this analysis are the totality of the events collected with our detector for which $\sqrt{s}$ is greater than 6.0 GeV. This sample corresponds to an integrated luminosity of 22.5 pb^{-1} at an average center-of-mass energy of 7.0 GeV. We used events with 3-or-more charged tracks. We searched for D mesons in this sample of 222,000 hadronic events by looking at the invariant mass distribution of $K^-\pi^+$ combinations for the D^0 and $K^-\pi^+\pi^+$ combinations for the D^+. The analysis technique used was the weight technique described earlier.

In order to determine the inclusive momentum spectrum the data were binned into different z or x bins, where $z = eE_D/\sqrt{s} = 2\sqrt{p^2_{total} + m^2_D}/\sqrt{s}$ and $x = 2p_{total}/\sqrt{s}$. Since we are quite close to the charm threshold it is not clear which one of the two scaling variables is more appropriate

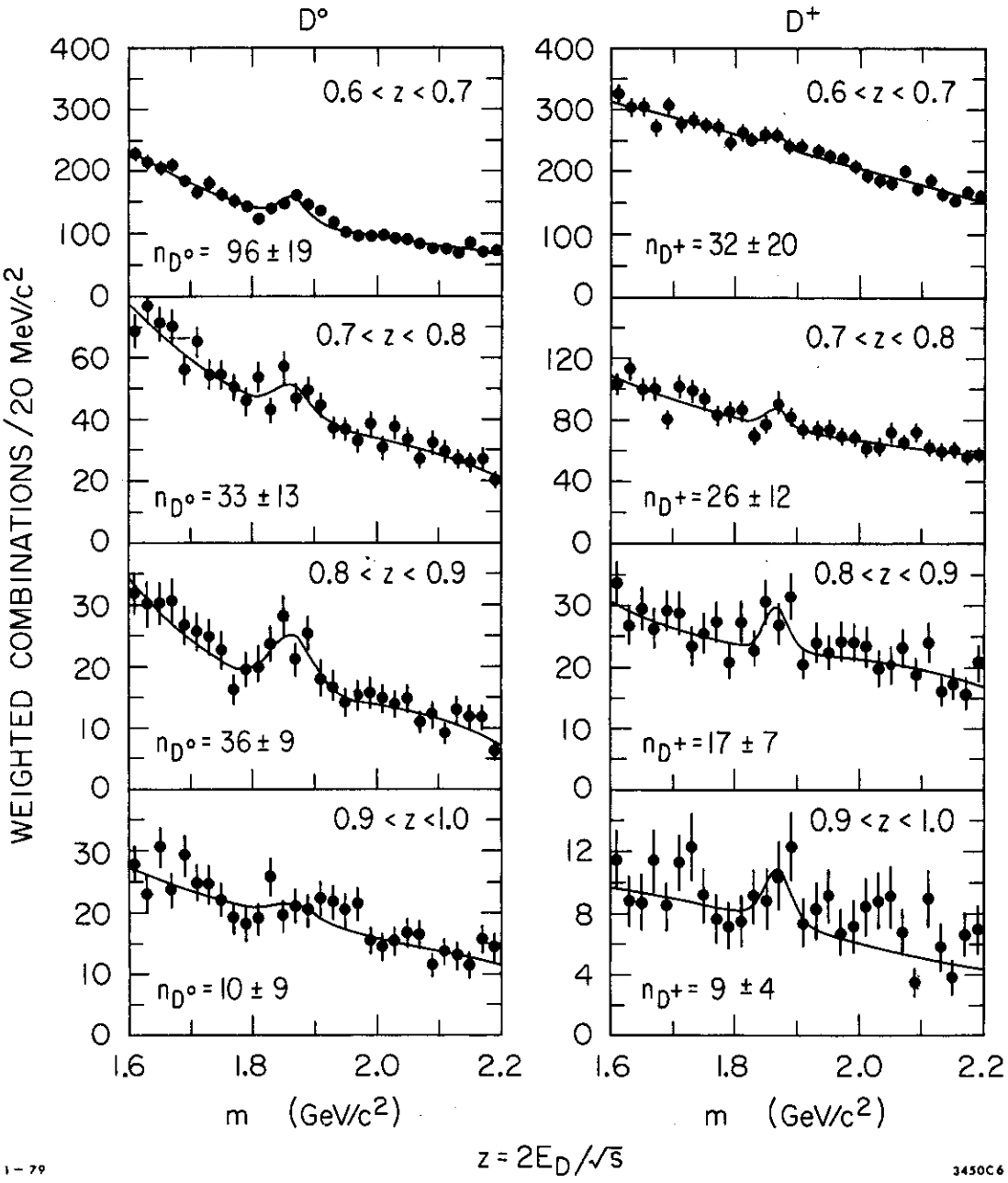

Figure 33 . Weighted invariant mass spectra for $K^{\pm}\pi^{\mp}$ and $K^{\mp}\pi^{\pm}\pi^{\pm}$ combinations for four regions of $z = 2E_D/\sqrt{s}$. The fitted curves are described in the text. The weighted number of observed D's is shown in the lower left side of each graph.

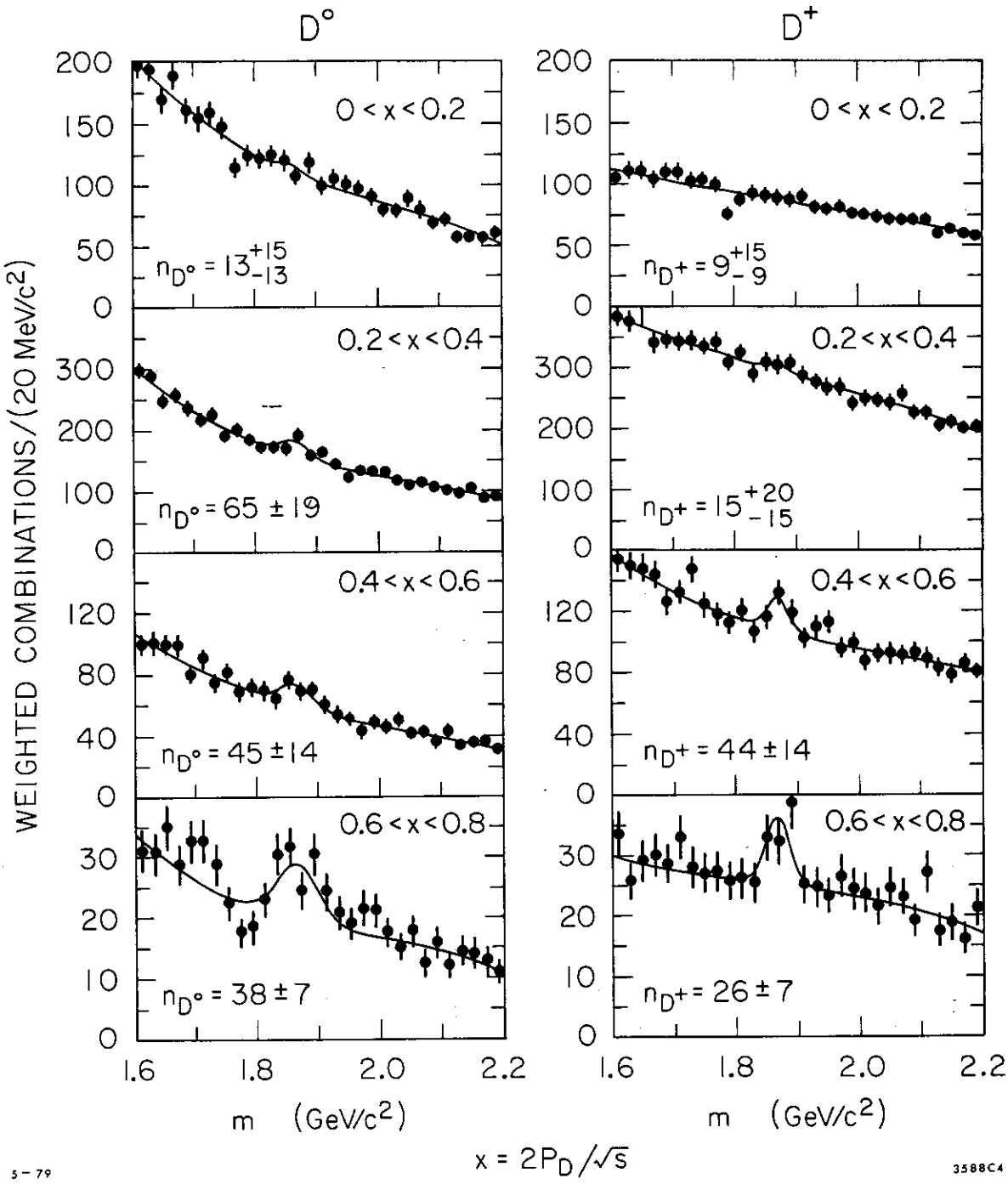

Figure 34. Weighted invariant mass spectra for $K^{\pm}\pi^{\mp}$ and $K^{\mp}\pi^{\pm}\pi^{\pm}$ combinations for four regions of $x = 2p_D/\sqrt{s}$. The fitted curves are described in the text. The weighted number of observed D's is shown in the lower left side of each graph.

to use.* For the same reason these varialbes do not cover the complete range of 0 to 1. The kinematically allowed regions are $z > 0.54$ and $x < 0.84$. The invariant mass distribution for the four z bins are shown in Fig. 33 and for the x bins in Fig. 34. The number of weighted D's in these plots was determined from a fit of a sum of a Gaussian of fixed mass and width and a simple polynomial background. The widths of the D's was the expected width estimated from the Monte-Carlo and shown in Fig. 13, the masses of the D's were taken to be 7 MeV/c^2 higher than their true mass, in order to account for the observed systematic shift of the D mass. We include in the quoted errors a contribution due to the slightly uncertain mass of the D's.

Our detection efficiency was determined in the two step procedure outlined in Chapter 2 as the product of two terms ε_D and ε_T, where ε_D is the efficiency of detecting D mesons of a fixed momentum decaying in $K^-\pi^+$ (for the D^o) and $K^-\pi^+\pi^+$ (for the D^+) and ε_T is the probability for an event with a detected D to trigger our apparatus and have at least three detected tracks in the final state.

In order to investigate the effect of a non-isotropic angular distribution of the D's, ε_D was determined for the two extreme cases of isotropic distribution ($\frac{d\sigma}{d\Omega} = \frac{1}{4\pi}$) and for $1 + \cos^2\theta$ distribution ($\frac{d\sigma}{d\Omega} = \frac{3}{16\pi}(1 + \cos^2\theta)$). The values of ε_D for these two distributions is shown in Fig. 13. The efficiency which was finally used was given

---

*Field and Feynman[22] suggest the use of the rapidity-like variable $y = \frac{E_D + p_{||}}{E_{beam} + p_q}$ where $p_{||}$ is the component of the D momentum parallel to p_q, the original quark's momentum, to avoid threshold related problems. Unfortunately, the direction of p_q is not directly measurable. What we can determine, and not always reliably, is a jet axis for an event. There are valid indications that D's are produced in association with jets in e^+e^- annihilation. We refer the reader for more information to the excellent review by G. Hanson[76] on jet production in e^+e^- collisions.

by : $$\varepsilon_D = \varepsilon_{1 + \cos^2\theta} \cdot \alpha + \varepsilon_{ISOTROPIC} \cdot (1 - \alpha)$$

where α is a momentum dependent parameter determined from inclusive hadron production in e^+e^- annihilation.[77] A graph of α is shown in Fig. 35, it ranges from $\alpha = 0$ at $x = 0$ to $\alpha = 1$ at $x = 0.84$. From this figure and Fig. 13, we see that the effect of an angular distribution is negligible at low x values, and at high x it reduces our efficiency by approximately 15%. Here we have assumed that the angular distribution of inclusively produced D's as a function of x is similar to the angular distribution for single charged particles (i.e. pions) as a function of x. The effects of charged kaon decay in flight were also included in this part of the efficiency,* Fig. 13 illustrates this effect too, which is of the order of 15% for all x values. Systematic effects to this part of the efficiency due to long-time changes of the TOF resolution** were investigated by analyzing the data 3 times with a σ_{TOF} of .35, .4 and .45; the effects of such a change are small (approximately .1 to .3 of the statistical error). A more severe source of error is the variation of ε_D within a z or x bin. We overestimated such uncertainties by assigning an error to ε_D equal to approximately 70% of its variation in the corresponding z or x bin. In summary, we estimate that the systematic uncertainty to ε_D may be as high as 15%, but the point-to-point uncertainty is less than half as much.

The triggering efficiency, ε_T, was determined from a Monte-Carlo simulation by generating a state of two D's or D^*'s with a few pions. One of the D's was constrained to decay to $K^-\pi^+$ or $K^-\pi^+\pi^+$ (the tagging mode), while the other D decayed in a variety of modes in such a way that its charged particle decay multiplicity was the same as the measured[67] decay multiplicity for D's. This part of the efficiency

*We simulated losses due to K decay in flight in a rather simplistic manner. The $K^\pm$ was allowed to decay randomly according to an exponential decay with a time constant equal to the charged kaon lifetime. If it decayed before reaching the last layer of the spark chambers we assumed it was never reconstructed by our tracking algorithms.

**The data was collected over a period that spans more than three years. For this reason $\sigma_{TOF} = .4$ ns is a more appropriate choice.

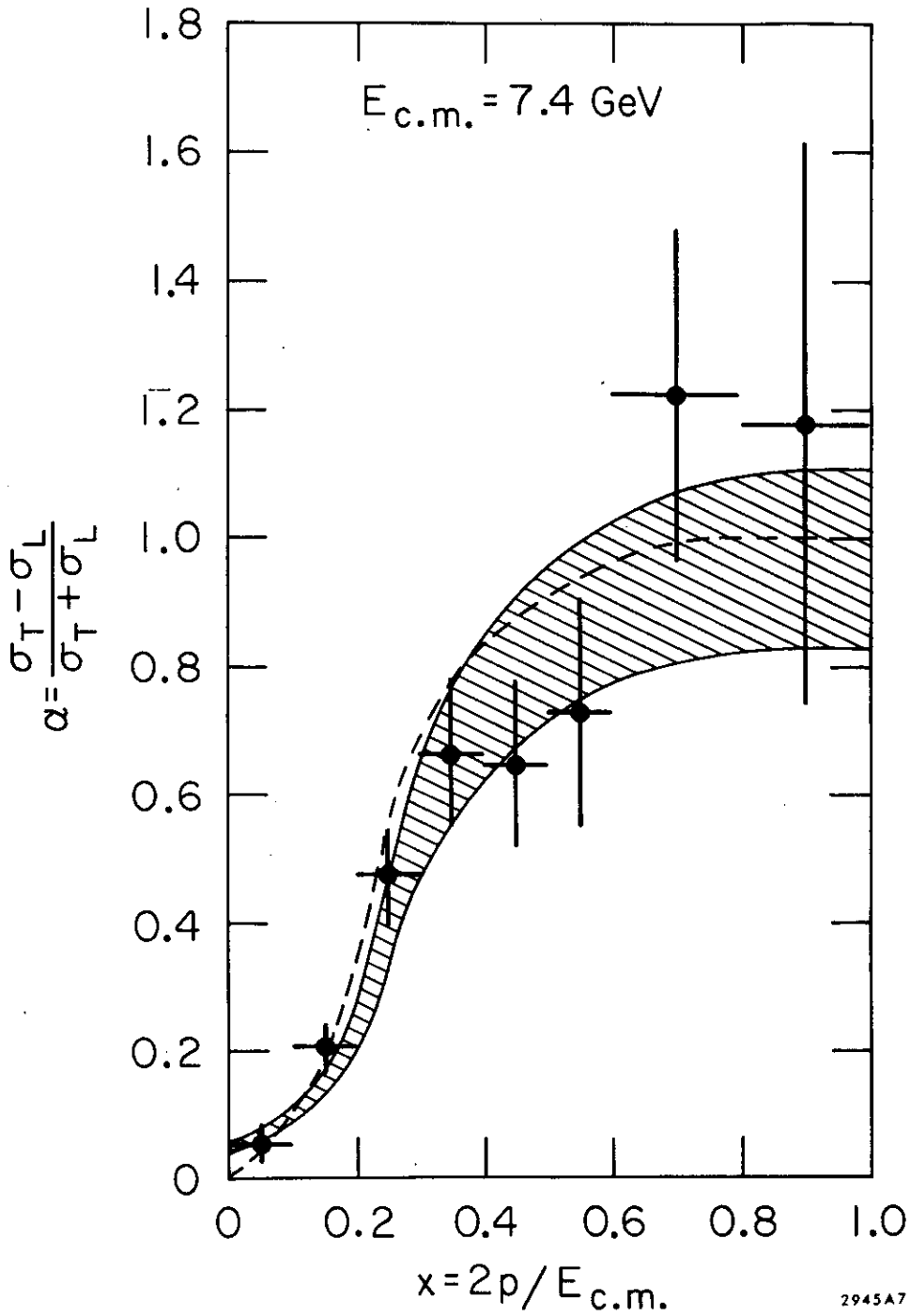

Figure 35. Observed inclusive α vs. x for particles with $|\cos\theta|<0.6$ in hadronic events at $E_{c.m.}=7.4$ GeV (Ref. 77). The prediction of the jet model Monte Carlo simulation for a jet axis angular distribution of the form $1+(0.97\pm0.14)\cos^2\theta$ is represented by the shaded band. The dashed line is the $\alpha(x)$ used in our analysis.

is both model dependent and dependent on the D momentum. The results for a variety of models are shown in Table VIII. The fact that ϵ_T is always larger than 90% allows us to assume that ϵ_T is independent of the momentum of the D. The values we used are $.95 \pm .05$ for the D^o and $.99 \pm .02$ for the D^+.

After these efficiency corrections, and taking into account the known branching ratios for the decays $D^o \to K^-\pi^+$ ($2.2 \pm 0.6\%$) and $D^+ \to K^-\pi^+\pi^+$ ($3.9 \pm 1.0\%$) the inclusive momentum spectra shown in Fig. 36 were obtained. These results are summarized in Table IX.

For comparison the same spectra are shown again in Fig. 37 together with the charged π and K_s inclusive spectra observed in e^+e^- annihilation over a comparable range of energies.[50,77] We observe that the D meson production is similar to the π production and significantly higher than the K_s production over the range of z = .6 to 1.0. All three of the displayed spectra are decreasing functions of z and have approximately the same slope. It should also be noted that the recently reported[78] γ and π^o inclusive spectra in e^+e^- annihilation show a similar behavior.

We fit the averaged D meson production spectrum with three of the forms proposed for the quark fragmentation function. For the form $D(z) = \frac{a}{z}(1-z)^\alpha$ we obtain $\alpha = .42 \pm {}^{.28}_{.23}$, for $D(z) = b(1-z)^\beta$ we obtain $\beta = .63 \pm {}^{.30}_{.24}$, and for $D(z) = c\, e^{\gamma z}$ we obtain $\gamma = -3.6 \pm {}^{1.3}_{1.4}$. All of these forms give a reasonable representation of the data. Table X summarizes these results, together with fits to the individual D^o and D^+ z spectra. Even though our statistical error is quite large and even though charm threshold effects could be significant at this energy range, our results, Fig. 36 and Fig. 37, are in disagreement with the idea that the fragmentation function for heavy quarks should be an increasing function of z. A similar conclusion can be drawn from the D meson spectrum observed in neutrino reactions.[74]

Finally, the total number of D^o's and D^+'s observed allows us to determine the cross-section for inclusive D meson production in e^+e^- annihilation for the energy range $\sqrt{s}$ = 6 to 7.8 GeV. We find $(e^+e^- \to D^o$ or $\bar{D}^o$ + anything) = 3.2 ± 0.9 nb and $\sigma(e^+e^- \to D^+$ or D^- + anything) = 1.7 ± 0.7 nb. Their sum corresponds to $R_D = 2.7 \pm 0.7$, where R_D is the ratio of the single charged and neutral D and $\bar{D}$ meson inclusive production to the rate of $\mu^+\mu^-$ pair production.

TABLE VIII

Model Dependence of the Triggering Efficiency ϵ_T
For Inclusive D Meson Production

Model	Tagging Mode	
	$D^o \to K^-\pi^+$	$D^+ \to K^-\pi^+\pi^+$
D^+D^- --		.997
$D^+D^-\pi^o$		.992
$D^+\bar{D}^o\pi^-$	.980	.995
$D^{*-}D^+$		.998
$\bar{D}^oD^+\pi^-\pi^o\pi^o$	.997	.9996
$D^o\bar{D}^o$	.939	
$D^o\bar{D}^o\pi^o$	.910	
$D^o\bar{D}^o\pi^o\pi^o$	.900	
$D^o\bar{D}^o\pi^+\pi^-$	.992	
$\bar{D}^oD^{o*}$	.936	
Value used	$.95 \pm .05$	$.99 \pm .02$

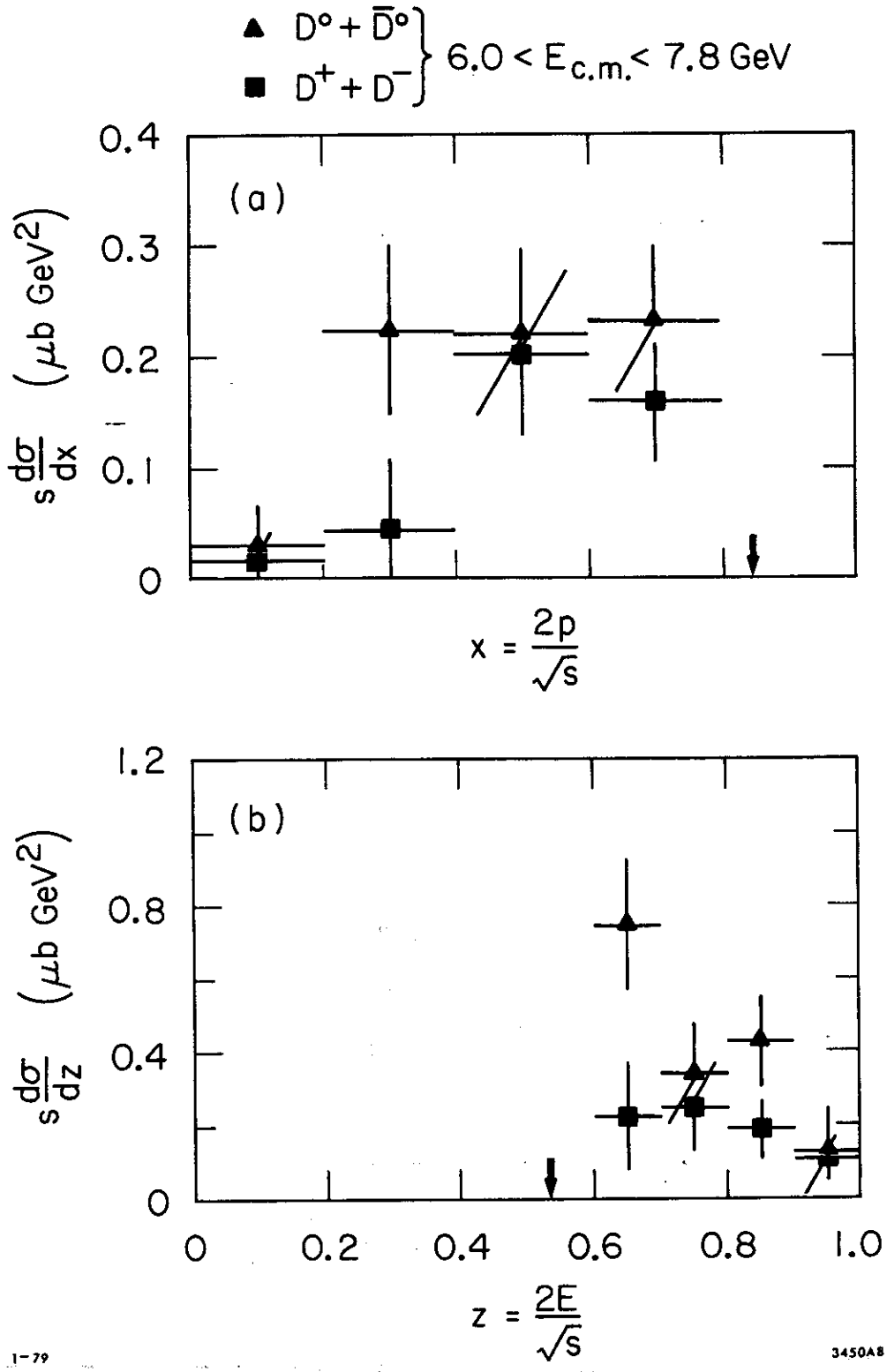

Figure 36. Inclusive production spectra for charged and neutral D's as functions of z and x. The error bars include statistical errors and the expected systematic variation from point to point. An overall normalization uncertainty of approximately 10% as well as the uncertainty in the D decay branching fractions have not been included. Arrows indicate kinematic limits.

TABLE IX

Cross Section for Inclusive D Meson Production at 7 GeV.

Z bin	Number of Weighted D^o's Observed	Number of Weighted D^+'s Observed	$\left[s\frac{d\sigma}{dz}\right]_{D^o}$ (μb-GeV^2)	$\left[s\frac{d\sigma}{dz}\right]_{D^+}$ (μb-GeV^2)
.6 - .7	96.0 ± 19.0	32.0 ± 20.2	.75 ± .18	.22 ± .15
.7 - .8	32.9 ± 12.5	26.3 ± 11.8	.34 ± .14	.25 ± .12
.8 - .9	35.8 ± 8.8	16.5 ± 6.5	.43 ± .12	.19 ± .08
.9 - .1	9.8 ± 9.4	8.5 ± 4.4	.13 ± .12	.11 ± .06

X bin	Number of Weighted D^o's Observed	Number of Weighted D^+'s Observed	$\left[s\frac{d\sigma}{dx}\right]_{D^o}$ (μb-GeV^2)	$\left[s\frac{d\sigma}{dx}\right]_{D^+}$ (μb-GeV^2)
0 - .2	13.1 ± 14.8	8.6 ± 16.3	.03 ± .04	.02 ± .03
.2 - .4	65.0 ± 20.6	14.7 ± 20.9	.22 ± .08	.04 ± .06
.4 - .6	44.4 ± 13.9	44.0 ± 14.0	.22 ± .08	.20 ± .07
.6 - .8	38.1 ± 9.5	26.1 ± 7.4	.23 ± .07	.16 ± .05

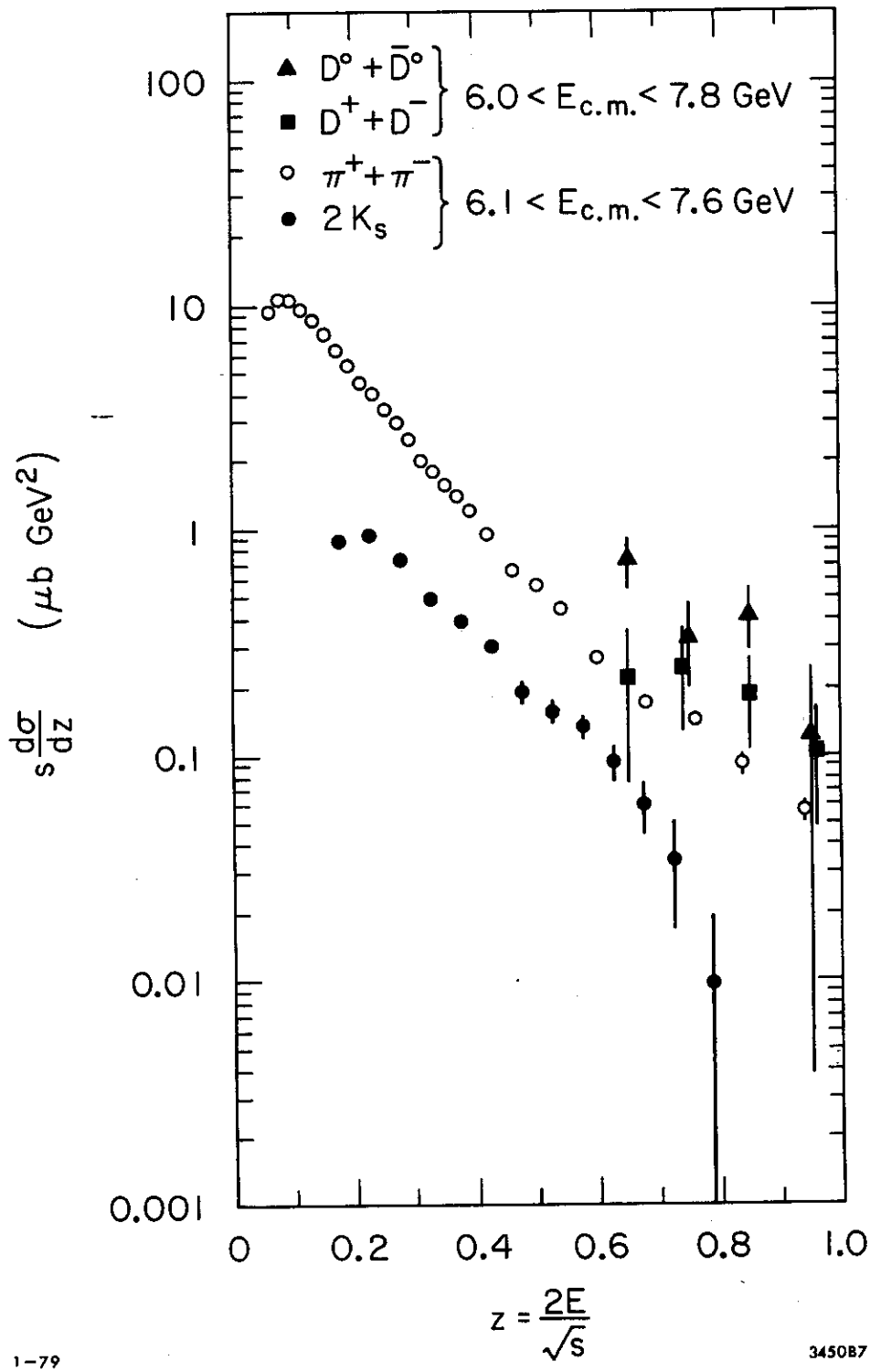

Figure 37. Inclusive spectra for charged and neutral D mesons and for charged pions and K_s^o. The K_s^o spectrum is taken from Ref. 50, the charged pion spectrum is obtained from the single charged-particle spectrum of Ref. 77 after subtracting the charged kaon contribution. The charged kaon spectrum was assumed to be equal to twice the K_s^o spectrum of Ref. 50.

TABLE X

Shape Fits to $s\frac{d\sigma}{dz}$ spectra of
Inclusive D Meson Production

Fitted Function	Parameter	Averaged Spectrum	D^o Spectrum	D^+ Spectrum
$\frac{a}{z}(1-z)^{\alpha}$	α	$.42^{+.28}_{-.23}$	$.54^{+.42}_{-.31}$	$.24^{+.37}_{-.33}$
$b(1-z)^{\beta}$	β	$.63^{+.30}_{-.24}$	$.76^{+.45}_{-.33}$	$.43^{+.39}_{-.34}$
$c\ e^{\gamma z}$	γ	$-3.6^{+1.3^{\dagger}}_{-1.4}$	$-4.3^{+1.7^{\dagger}}_{-2.0}$	$-2.6^{+2.3^{\dagger}}_{-2.2}$

†For comparison, a fit of the form $c\ e^{\gamma z}$ to the last five points of the pion $s\frac{d\sigma}{dx}$ spectrum of Fig. 35 gives $\gamma = -5.5 \pm 0.6$

REFERENCES

1. G.J. Feldman in Proceedings of the 19th International Conference on High Energy Physics, Tokyo, Japan, 1978, p. 777.
2. G. Weber, invited talk at the IX International Symposium on High Energy Multiparticle Dynamics, Tabor, Czechoslovakia, July, 1978, DESY report 78/35.
3. G. Feldman and M.L. Perl, Phys. Rep. 33C, no 5, 285(1977).
4. G. Feldman and M.L. Perl, Phys. Rep. 19C, no 5, 233(1975).
5. J.P. Perez-y-Jorba, and F.M. Renard, Phys. Rep. 31C, no. 1 (1977).
6. A. W. Hendry and D.B. Lichtenberg, Rept. Prog. Phys. 41, 1707(1978).
7. T. Appelquist, R.M. Barnett, and K. Lane, Ann. Rev. Nuc. Part. Sci., 28, 387(1975).
8. M.K. Gaillard, B.W. Lee, and J.L. Rosner, Rev. Mod. Phys. 47, 277(1975).
9. S.J. Brodsky, T. Kinoshita, and H. Terazawa, Phys. Rev. D4, 1532 (1971).
10. H.D. Politzer, Phys. Rev. Lett. 26, 1346(1973); D. Gross and F. Wilczek, Phys. Rev. Lett. 26, 1343(1973).
11. J. Sapirstein, private communication.
12. S. Okubo, Phys. Lett. 5, 105(1963);
    G. Zweig, CERN report TH-401, 412(1964);
    J. Iizuka, K. Okada, and O. Shito, Prog. Theor. Phys. 35, 1061(1966).
13. W. Tanenbaum et al., Phys. Rev. D17 1731(1978).
14. E. Eichten et al., Phys. Rev. D17, 3090(1978);
    E. Eichten et al., Phys. Rev. Lett. 34, 369(1975); 36, 500(1976).
15. K. Lane and E. Eichten, Phys. Rev. Lett. 37, 477, 1105 (E)(1976).
16. R. Brandelik et al., Phys. Lett. 70B, 132(1977);
    S. Yamada in Proceedings of the 1977 International Symposium on Lepton and Photon Interactions at High Energies, Hamburg, August 1977, p. 47.
17. D. Lüke, Proceedings of the 1977 Meeting of the APS Division of Particles and Fields, Argonne, Ill. 1977, p. 441(1977).
18. A. Barbaro-Galtieri in Proceedings of the XVI International School of Subnuclear Physics, Erice, Italy, July 1978, LBL report 8537, to be published.

19. M. Piccolo et al., Phys. Rev. Lett. 39, 1503(1977).
20. For an overall review see: R.P. Feynman, Photon-Hadron Interactions (Benjamin Reading, Mass. 1972).
21. R.D. Field, and R.P. Feynman, Phys. Rev. D15, 2590(1977); R.P. Feynman, R.D. Field, and G.C. Fox, Nucl. Phys. B128, 1(1977).
22. R.D. Field and R.P. Feynman, Nucl. Phys. B136, 1(1978).
23. R.P. Feynman, R.D. Field, and G.C. Fox, Phys. Rev. D18, 3320(1978); R.D. Field, Physica Scripta 19, 131(1979).
24. L.M. Sehgal and P.M. Zerwas, Nucl. Phys. B108, 483(1976).
25. A Seiden, Phys. Lett. 68B, 157(1977).
26. M. Gronau et al., Nucl. Phys. B123, 47(1977).
27. S.D. Ellis, M. Jacob, and P.V. Landshoff, Nucl. Phys. B108, 93(1976).
28. S.J. Brodsky and G.R. Farrar, Phys. Rev. Lett. 31, 1153(1973); Phys. Rev. D11, 1309(1975); V.A. Matveev, R.A. Muradyan, and A.V. Tavkheldize, Lett. Nuovo Cimento 7, 719(1973); R. Blankenbecler and S.J. Brodsky, Phys. Rev. D10, 2973(1974). S.J. Brodsky and G.P. Lepage in Workshop on Current Topics in High Energy Physics, CIT, Pasadena, Calif., February 1979, to be published, SLAC publication 2294 (1979).
29. M. Suzuki, Phys. Lett. 68B, 164(1977); 71B, 139(1977).
30. V.G. Kartvelishvili, A.K. Likhoded, and V.A. Petrov, Phys. Lett. 78B, 615(1978); V.G. Karvelishvili and A.K. Likhoded, IHEP report 78-33, Serpukhov 1978, unpublished.
31. V. Barger, T. Gottschalk and R.J.N. Phillips, Phys. Lett. 70B, 51(1977).
32. For a review see F. Dydak in Facts and Prospects of Gauge Theories: Proceedings of the XVII Internationale Universitätswochen für Kernphysik der Karl-Franzens-Universität Graz, Schladming, Austria, 1978, edited by P. Urban, Acta Physica Austriaca, Supplementum XIX, p. 463.
33. For a review and references to this data see: C.H. Lai, Phys. Rev. D18, 1422(1978).
34. R. Odorico, Phys. Lett. 71B, 121(1977); R. Odorico and V. Roberto, Nucl. Phys. B136, 333(1978).

35. J. Dias De Deus, Nucl. Phys. B138, 465(1978).
36. J.B. Bjorken, Phys. Rev. D17, 171(1978).
37. M. Sands in Physics with Intersecting Storage Rings; Proceedings of Course XLVI of the International School of Physics "Enrico Fermi", Varenna, June 1969, edited by B. Touschek, Academic Press, N.Y. 1971.
38. F. Vannucci et al., Phys. Rev. D15, 1814(1977).
39. R. Hollebeek, Thesis, 1975, LBL report 1874, unpublished.
40. J.E. Zipse, Thesis, 1975, LBL report 4281, unpublished.
41. J.S. Whitaker, Thesis, 1976 LBL report 5518, unpublished.
42. J.E. Wiss, Thesis, 1977, LBL report 6725, unpublished.
43. B.P. Kwan, Thesis, 1978, SLAC report 207, unpublished.
44. J.M. Feller, 1979, LBL report 9017, unpublished.
45. D.E. Fries, SLAC report 99, unpublished.
46. G. Goldhaber et al., Phys. Rev. Lett. 37, 255(1976).
47. I. Peruzzi et al., Phys. Rev. Lett. 37, 569(1976).
48. G. Hanson et al., Phys. Rev. Lett. 35, 1609(1975).
49. G.J. Feldman et al., Phys. Rev. Lett. 38, 1313(1977).
50. V. Lüth et al., Phys. Lett. 70B, 120(1977).
51. R.F. Schwitters, Proceedings of 1975 International Symposium on Lepton Photon Interactions at High Energies, Stanford, Calif., p. 355 (1975).
52. P.A. Rapidis et al., Phys. Rev. Lett. 39, 526(1977).
53. W. Bacino et al., Phys. Rev. Lett. 40, 671(1978).
54. R.R. Larsen, Proceedings of the 1974 Meeting of the APS Division of Particles and Fields, Williamsburg, Virginia, Sept. 1974.
55. G. Bonneau and F. Martin, Nucl. Phys. B27, 381(1971).
56. J.D. Jackson and D.L. Scharre, Nucl. Instrum. Methods 128, 13(1975).
57. D.R. Yennie, Phys. Rev. Lett. 34, 239(1975).
58. A.M. Boyarski et al., Phys. Rev. Lett. 34, 1357(1975).
59. J. Siegrist et al., Phys. Rev. Lett. 36, 700(1976).
60. J.-E. Augustin et al., Phys. Rev. Lett. 34, 764(1975).
61. J.D. Jackson, Nuovo Cimento 34, 1645(1964)
A. Barbaro-Galtieri, in Advances in Particle Physics, edited by R.L. Cool and R.L. Marshak (Wiley, New York, 1968), Vol. II.
62. V. Lüth et al., Phys. Rev. Lett. 35, 1124(1975).

63. R. Van Royen and V.F. Weisskopf Nuovo Cimento 50A, 617(1967); 51A, 583(1967).
64. I. Peruzzi et al., Phys. Rev. Lett. 39, 1301(1977).
65. G. Goldhaber et al., Phys. Lett. 69B, 503(1977).
66. H.K. Nguyen et al., Phys. Rev. Lett. 39, 262(1977).
67. V. Vuillemin et al., Phys. Rev. Lett. 41, 1149(1978).
68. J.M. Feller et al., Phys. Rev. Lett. 40, 1677(1978); 41, 518 (E) (1978).
69. D.L. Scharre et al., Phys. Rev. Lett. 40, 74(1978).
70. M. Piccolo et al., submitted to Phys. Lett., SLAC-PUB 2323.
71. M. Piccolo et al., Phys. Lett. 70B, 260(1977).
72. S.L. Glashow, I. Iliopoulos, and L. Maiani, Phys. Rev. D2, 1285 (1970).
73. R.H. Schindler, private communication.
74. C. Baltay et al., Phys. Rev. Lett. 41, 73(1978).
75. P.A. Rapidis et al., Phys. Lett. (in press), SLAC publication 2184.
76. G. Hanson in Proceedings of the 13th Recontre de Moriond on High Energy Leptonic Interactions and High Energy Hadronic Interactions, edited by Tran Thanh Van, Les Arcs, Savoie, France, 1978, Vol. II, p. 15.
77. G. Hanson et al., Phys. Rev. Lett. 35, 1609(1975); G. Hanson in Proceedings of the XVIII International Conference on High Energy Physics, Tbilisi, U.S.S.R., 1976, p. B1.
78. D.L. Scharre et al., Phys. Rev. Lett. 41, 1149(1978).
79. T. Himel et al., Bull. Amer. Phys. Soc. 24, No. 4, 600(1979); E.D. Bloom in Proceedings of the 14th Recontre de Moriond , edited by Tran Thanh Van, Les Arcs, Savoie,France, to be published.
80. R.H. Schindler et al., Bull. Amer. Phys. Soc. 24, No. 4, 600(1979).
81. J.D. Jackson in Proceedings of the European Conference on Particle Physics, Budapest, Hungary, 1977, edited by L. Jenik and I. Montvay, p. 603.